Dissertation
submitted to the
Combined Faculties for the Natural Sciences and for Mathematics
of the Ruperto-Carola University of Heidelberg, Germany
for the degree of
Doctor of Natural Sciences

Put forward by

Diplom-Physicist: Gernot Guigas
Born in: Karlsruhe, Germany

Oral examination: 16 July 2008

On the Mobility of Macromolecules in Cells

Referees:	**Prof. Dr. Michael Hausmann**
	Dr. Matthias Weiss

Zusammenfassung:
Im ersten Teil der vorliegenden Arbeit werden Diffusionsuntersuchungen mit Fluoreszenzkorrelationsspektroskopie an fluoreszenzmarkierten Nanogold-Partikeln in Zytoplasma und Nukleus lebender Zellen vorgestellt. Die Messungen zeigten, dass sich die Nanopartikel per Subdiffusion bewegten, d.h. ihre mittlere quadratische Verschiebung ein Zeitskalierungsverhalten $\sim t^{\alpha}$, $\alpha < 1$ aufwies. Ein solches Bewegungsverhalten lässt sich auf die in großen Mengen in intrazellulären Flüssigkeiten gelösten Makromoleküle (beispielsweise Proteine) zurückführen, welche die Bewegung einzelner Nanopartikel behindern. Aus dem Diffusionsverhalten der Partikel wurde das komplexe Schermodul $G(\omega) \sim \omega^{\alpha}$ der intrazellulären Flüssigkeiten berechnet; dies zeigte, dass sich das Zellinnere auf der Nanoskala viskoelastisch verhält. Im Weiteren wurde anhand von Computersimulationen quantifiziert, mit welcher Effizienz ein subdiffundierendes Molekül ein fixiertes Ziel erreicht (beispielsweise eine Bindungsstelle). Es ergab sich, dass die Wahrscheinlichkeit, ein Ziel zu erreichen, für einen subdiffundierenden Partikel höher ist als für einen normal diffundierenden Partikel, was den Schluss zulässt, dass eine Zelle von der Subdiffusion von Makromolekulen in ihrem Inneren profitiert. Im zweiten Teil der Arbeit wird in 'grobkörnigen' Molekulardynamiksimulationen ('dissipative particle dynamics') das zweidimensionale Diffusionsverhalten von in Lipidmembranen eingebetteten zylindrischen Objekten mit unterschiedlichen Radien untersucht. Es erwies sich hierbei, dass eine zutreffende Vorhersage der Größenabhangigkeit der Diffusionskoeffizienten durch die Saffman-Delbrück-Theorie gegeben wird.

Summary:
In the first part of this thesis diffusion measurements with fluorescence correlation spectroscopy on fluorescence-labeled nanogold particles in the cytoplasm and the nucleus of living cells are presented. The nanoparticles were detected to move by subdiffusion, i.e. their mean square displacement displayed a power-law scaling $\sim t^{\alpha}$, $\alpha < 1$. This observation can be explained with the high amounts of macromolecules (such as proteins) dissolved in intracellular fluids which obstruct the motion of indiviual nanoparticles. From the diffusion behaviour of the particles the complex shear modulus $G(\omega) \sim \omega^{\alpha}$ of the intracellular fluids was calculated, which showed the cellular interior to be viscoelastic on the nanoscale. Furthermore, the efficiency of a subdiffusive molecule to approach a fixed target was quantified. Computer simulations highlighted here that the probability to reach a target is increased for a subdiffusive particle as compared to a normal diffusive particle, which suggests that a cell may benefit from the subdiffusion of macromolecules in its interior. In the second part of the thesis the two-dimensional diffusion of cylindrical objects embedded in lipid membranes is investigated. Coarse-grained molecular dynamic simulations ('dissipative particle dynamics') demonstrated that the size-dependence of the diffusion coefficients is properly described by the Saffman-Delbrück theory.

Contents

Chapter 1

Introduction

A living system can be described as a self-preserving and self-reproducing entity. To allow in this context a clear differentiation between living organisms and other organised matter systems, a number of ’criteria of life’ has been specified in biology, the most important of which are motion, reproduction, metabolism, growth and stimulus response. Living organisms obtain their specific features and abilities which classify them as ’living’ due to a variety of concerted processes which permanently run in their interior. These processes consist in activities of both chemical and mechanical nature. The length and time scales on which they occur include all orders of magnitude between the macroscopical appearance of the organism and the molecular level. Since processes on a certain length and time scale naturally depend on the events on subordinated levels, processes on the molecular level are fundamental and of particular importance.

On the micron scale and below, all living organisms are organised similarly: they consist of cells as fundamental units. Cells themselves have to be regarded as living organisms: they represent the most elementary (and smallest) entities that meet the biological criteria of life. A cell is kept alive by the variety of biochemical processes taking place in its interior, which serve for example for material uptake, energy transduction or the synthesis of functional macromolecules.

Functional biological macromolecules are the cornerstones of cells, and therefore of all biological matter. They are involved in the construction of biological matter as well as in the storage of biological information and in the implementation of biological functions. The main species of biological macromolecules are proteins, deoxyribonucleic acid (DNA) molecules, ribonucleic acid (RNA) molecules, lipids and sugars.

An elementary property of biological macromolecules is their mobility. The natural environment of biological molecules – which may be the cellular interior or the space between cells in an organism – is typically a fluid. To carry out its particular function, a biological macromolecule usually has to overcome the distance between the location where it was generated and its specific target, which could be for example a reaction partner or a binding site. While there exist energy-consuming transport systems like the blood circulation, the lymphatic system or active transport along filaments to carry large amounts of molecules over long distances in an organism, a molecule covers 'short' distances of the magnitude of a cell's diameter and below typically by thermally driven motion, i.e. diffusion. How effective a macromolecule species spreads in space obviously is of fundamental importance for all processes in which the molecule participates, e.g. chemical and enzymatic reactions or the assembly of large structures or patterns.

In the work presented here, some basic questions concerning diffusion of macromolecules in biological systems will be addressed. Diffusion generally is a random process being induced by kicks of thermally moving solvent molecules on a dissolved particle. A diffusing macromolecule therefore has no preferred direction, but explores its environment isotropically. The longer a diffusion process continues, the larger is the explored space, and the larger becomes the distance to its starting point a tracer has covered on average. The diffusive spreading depends on the size and the shape of the diffusing molecule just as on the rheological properties of the embedding fluid and can be measured by the particle's mean square displacement. For the simple case of a spherical particle in a three-dimensional viscous fluid, the mean square displacement grows linearly with time; the proportionality factor is the diffusion coefficient D that depends on the particle radius, the fluid viscosity and the system temperature, according to the well-known Einstein-Stokes relation. The spreading of a diffusive particle here is the faster the smaller the particle and the less viscous the embedding fluid is.

For biological macromolecules in their natural environment diffusion is typically more complicated. At first, a general differentiation can be made: diffusion in three dimensions, i.e. macromolecules which are dissolved the in intra- or extracellular fluids (soluble proteins and RNA molecules), and diffusion in two dimensions, i.e. macromolecules which are embedded in biological membranes (lipids and membrane proteins). Biomembranes are lipid bilayer structures that surround and protect entire cells and intracellular compartments. Since membranes maintain their structural integrity due to non-covalent forces, their constituents can diffuse freely within the membrane which means that a membrane behaves as a two-dimensional fluid. Apart from the dimensionality macromolecule diffusion in a biological environment has the pecularity that it takes place in a non-homogeneous environment. Intra-/extracellular fluids as well as membranes are structured on several length scales; in particular on a scale of some ten nanometers they are densley occupied with interacting macromolecules of different sizes and shapes ('macromolecular crowing').

Both, the diffusion of macromolecules in the cellular interior and in membranes has been investigated for the present dissertation. The thesis is structured as follows: In Part I the three-dimensional mobility of macromolecules located in the cytoplasm and the nucleus of cells is examined; in association with this the rheological state of the intracellular fluids is studied. Chapters 2 – 4 give an overview on the current knowledge on these topics: Chapter 2 provides a general introduction to the mathematical description of diffusion and introduces anomalous subdiffusion, a specific mode of motion which was determined to play a particular role for macromolecules in cells. In Chapter 3 previous studies on intracellular diffusion and on cell rheology are discussed. In Chapter 4 the measurement methods used for this thesis are described.

Chapter 5 is the first results part. Here, diffusion measurements on fluorescently labeled nanogold particles (which were introduced as probe particle into living cells) are presented. The diffusion was measured using fluorescence correlation spectroscopy (FCS), a method that relies on the detection and analysis of the diffusion-driven concentration fluctuations in a small observation volume of the sample. As a result, the nanogold particles were determined to move by subdiffusion, i.e. their mean square displacement was growing nonlinear with a power-law scaling $\sim t^{\alpha}$, $\alpha < 1$. This is in strong contrast to the diffusion of these particles in water where $\alpha = 1$. In further measurements, subdiffusion was also detected for BSA proteins in cells. These findings suggest that subdiffusion is the mode of motion for many macromolecule species with diameters about 5 - 10 nm in cells.

From the diffusive behaviour of the nanogold particles the mechanical properties of the intracellular fluids were calculated in terms of the complex shear modulus $G(\omega)$. To do so, an approach given by Mason & Weitz was used, which relates $G(\omega)$ of a medium to the mean square displacement of embedded spherical probe particles [1]. As a result, cytoplasm and nucleoplasm of living cells were determined to be viscoelastic on the nanoscale with the complex shear modulus following a power-law scaling $G(\omega) \sim \omega^{\alpha}$. Comparative test measurements in unstressed and osmotically stressed cells suggested that, from a rheological point of view, intracellular fluids can be described phenomenologically as diluted polymer solutions obeying the Zimm theory. From the described measurements the conclusion can be drawn that the fluids in the interior of the cell are uniformly crowded with macromolecules having a high degree of entanglement, which explains tracer subdiffusion as well as the property of intracellular fluids to be viscoelastic. In accompanying measurements, subdiffusion of nanogold and viscoelastic rheological properties were detected to be conserved in various cell lines of different origins and health states.

Chapter 6 is the second results part, highlighting implications of subdiffusion. In computer simulations the ability to approach a fixed binding target was determined for particles moving by normal diffusion or subdiffusion. As a result, the simulations showed that the target finding probability P is increased for subdiffusive particles as compared to normally diffusing particles. Transferring these simulation results to concrete examples from biology indicated that cells indeed may benefit from their crowded internal state and the associated subdiffusion.

Part II of the thesis deals with the two-dimensional diffusion of macromolecules embedded in membranes. Chapter 7 gives a general introduction to the structure and functionality of membranes; furthermore, dissipative particle dynamics is introduced as a class of particle-based computer simulations suitable to examine membranes. Chapter 8 is the results part; here, a study on the two-dimensional mobility of membrane inclusions is presented. A theoretical expression which relates the diffusion coefficient D of a cylindrical membrane inclusion (e.g. a membrane protein) to its radius R was already derived in 1975 by Saffman & Delbrück, predicting $D \sim \log(1/R)$ [2]. However, a robust test of the Saffman-Delbrück theory has never been performed due to various experimental challenges. Here, dissipative particle dynamics simulations were used to determine the diffusion coefficients of differently sized membrane inclusions. The simulation data confirmed the Saffman-Delbrück theory to properly describe the above mentioned size-dependence.

Part I

On the diffusion of macromolecules in cytoplasm and nucleus

Chapter 2

Fundamentals of diffusion

In this chapter an introduction to the mathematical description of diffusion is given (Section 2.1). Anomalous subdiffusion is introduced and the general reasons for its occurrence are highlighted (Section 2.2). Furthermore, it is described how the searching efficiency of a diffusing particle for a specific target can be quantified and how it changes when different modes of diffusion are used (Section 2.3).

2.1 Brownian motion

Particles suspended in a fluid show directionless and irregular movements which appear due to thermal random kicks by solvent molecules. This phenomenon is denoted as Brownian motion or (self-)diffusion; the particle's movement is denominated a *random walk*.

The self-diffusion of a tracer is characterised by the probability distribution function $P(x,t)$ of the distances x from its starting point $x_0 = 0$ after a time period t.

$P(x,t)$ can be derived from stochastic theory. When we regard the simplest case of one-dimensional diffusion, a tracer jumps on a straight line small distances of random length δ either in positive or negative direction in short time intervals dt, with positive and negative jumps having the same probability p=1/2. The probability for exactly k jumps along the positive direction in n trials is then given by a Binomial distribution. For a large number n and a finite probability p of the process (i.e. $n \cdot p \rightarrow \infty$ as $n \rightarrow \infty$), the Binomial distribution approximates a Gaussian or normal distribution due to the central limit theorem [3]. Therefore, $P(x,t)$ for a d-dimensional problem and continuous space and time assumes the familiar form:

$$P(x,t) = \frac{1}{(4\pi Dt)^{(d/2)}} \cdot e^{-\frac{|x|^2}{4Dt}}. \tag{2.1}$$

Here, d is the embedding spatial dimension and D denotes the diffusion coefficient, while $P(x,t)$ gives the probability of a diffusing particle to be at a distance x from its starting point 0 at a time t. A plot showing the evolution of $P(x,t)$ in time is displayed in Figure 2.1.

By definition, the first moment of $P(x,t)$, i.e. the mean value of x, is:

$$\langle x \rangle = 0. \tag{2.2}$$

The second moment of $P(x,t)$ is the variance of $P(x,t)$ or the particle's mean square displacement:

$$\langle x^2 \rangle = 2dDt. \tag{2.3}$$

Higher moments of the Gaussian distribution are functions of the first and the second moment and thus contain no independent information.
The diffusion coefficient D depends specifically on the properties of a diffusing particle and of its embedding medium. For the case of a spherical particle in a three-dimensional homogeneous viscous medium, D is related to the absolute temperature T of the system, the medium viscosity η and the particle radius R by the Einstein-Stokes-relation [4]:

$$D = \frac{k_B T}{6\pi\eta R}. \tag{2.4}$$

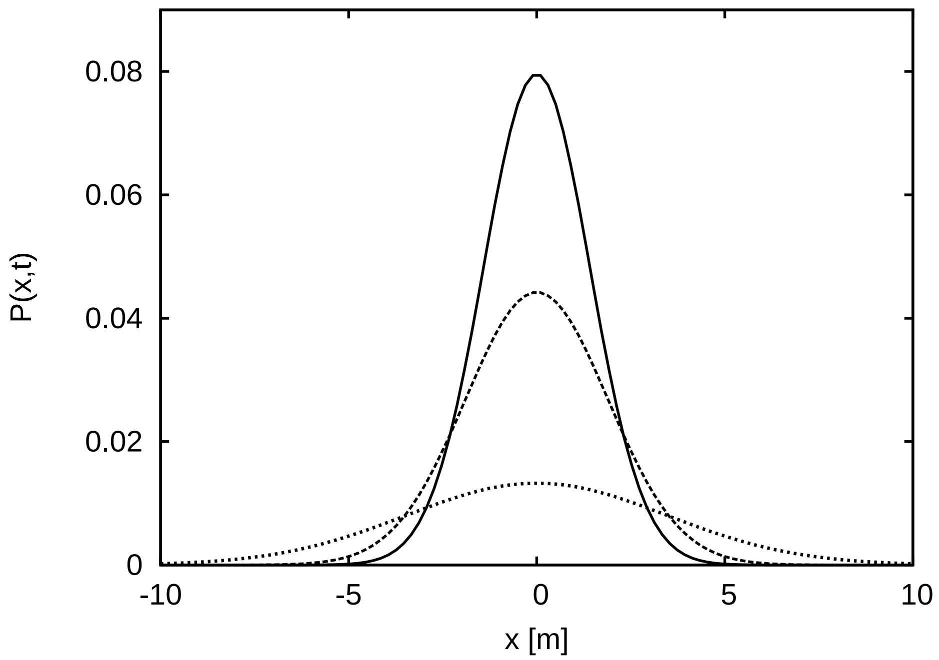

Figure 2.1: Evolution of the distribution $P(x,t)$ as described by Eq. 2.1, assuming a diffusion coefficient $D = 4$ m^2/s. Initial condition was $P(0,0) = \delta(x,t)$. Full line: $t = 1$ s, dashed line: $t = 2$ s, dotted line: $t = 6$ s.

Concentration diffusion

From the macroscopic view, self-diffusion of particles leads to the balancing of particle concentration gradients. The particle flow $\vec{\jmath}$ that arises due to a concentration gradient ∇C is given by Fick's first law [5]:

$$\vec{\jmath} = -D\nabla C. \tag{2.5}$$

Equation 2.5 together with the continuity equation (mass conservation) yields the diffusion equation (Fick's second law):

$$\frac{\partial C}{\partial t} = D\triangle C. \tag{2.6}$$

Equation 2.6 reflects the spatial and temporal change of concentration in a system after a perturbation from the steady state where all particles are uniformly distributed in the system. The general solution of equation 2.6 for a symmetric system is, with the initial condition $C(0,0) = \delta(x,t)$, a Gaussian (c.f. Figure 2.1):

$$C(x,t) = \frac{1}{(4\pi Dt)^{(d/2)}} \cdot e^{-\frac{x^2}{4Dt}} \tag{2.7}$$

This solution is the Green's function (or the propagator) of the diffusion equation which determines the time evolution of the δ-function. It is identical to Equation 2.1, i.e. the spreading of particle concentration and the probability distribution of a single diffusing particle follow the same function.

2.2 Anomalous diffusion

The spreading of particles in a diffusion process is characterised by the second moment (or the mean square displacement *MSD*) of its probability distribution function $P(x,t)$. In normal (classical, regular) Fickian diffusion, $P(x,t)$ is a Gaussian and the *MSD* grows linearly with time as described by Equation 2.3. The diffusion coefficient D has units m^2/s.

Diffusion processes which deviate from normal Gaussian behaviour are generally denoted as *anomalous diffusion* [6]. These processes typically show a non-linear scaling of the *MSD*:

$$MSD(t) = 2dD_A t^{\alpha}, \text{ with } \alpha \neq 1. \tag{2.8}$$

Here, D_A is the generalized diffusion constant in units m^2/s^{α} while α denotes the degree of anomaly. In case of $\alpha < 1$, one speaks about *subdiffusion*, the case $\alpha > 1$ denotes *superdiffusion*. In classical normal diffusion α is unity, while ballistic transport is described by $\alpha = 2$. Figure 2.2 illustrates the different time scaling behaviour of normal diffusion, subdiffusion and superdiffusion.

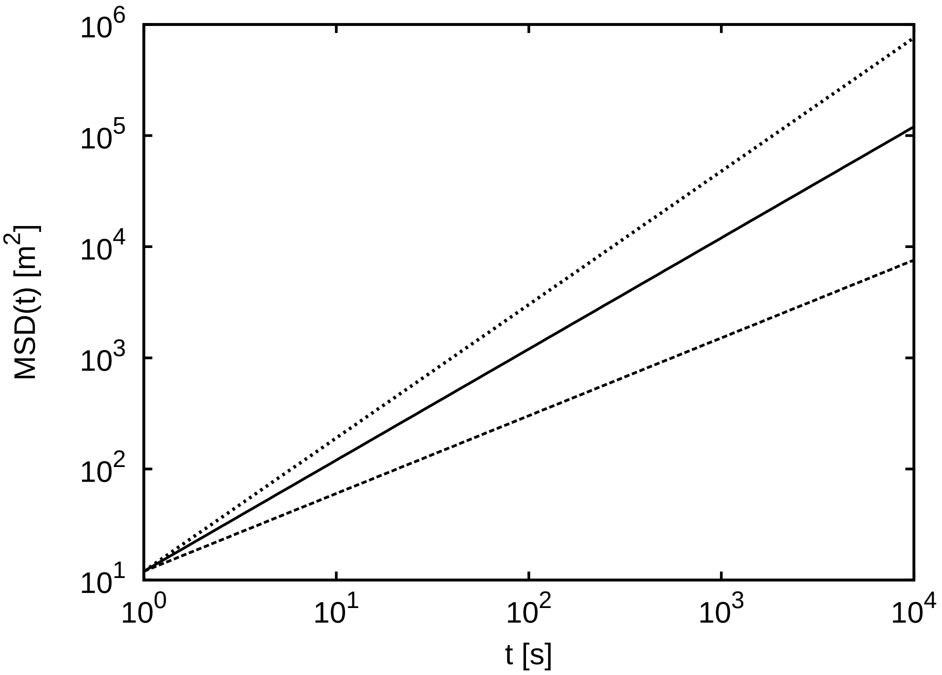

Figure 2.2: Mean square displacement $MSD(t) \sim t^{\alpha}$ of particles which move by normal diffusion (full line), subdiffusion with $\alpha = 0.7$ (dashed line), superdiffusion with $\alpha = 1.2$ (dotted line)

Anomalous diffusion has been experimentally observed for various transport processes. Superdiffusion, for instance, was shown to describe the relative diffusion of two objects in a turbulent flow [7] or the travelling behaviour of humans [8]. Examples for subdiffusion include charge transport in amorphous semiconductors [9], the dynamics of polymers [10] or the diffusion of objects in a viscoelastic environment [11].

2.2.1 Reasons for anomalous diffusion

The Gaussian nature of normal diffusion results from the central limit theorem (CLT) of probability theory. The CLT states the following: Given an arbitrary distribution $G(x)$ of independently and identically distributed random variables x with finite mean $\langle x \rangle$ and finite variance $\langle x^2 \rangle$, the mean values of random samples of size N taken from $G(x)$ will follow a normal distribution with mean $\langle x \rangle$ and variance $\langle x^2 \rangle / N$.

A diffusive process described by the probability distribution $P(x,t)$ will appear anomalous when the validity of the CLT breaks down for $P(x,t)$ and hence $P(x,t)$ does not approach a Gaussian. This is the case when either

a) the variance of $P(x,t)$ diverges due to large/critical fluctuations or

b) long-range correlations arise in the system [12].

Large fluctuations in a diffusion system typically occur when the jump lengths and/or the waiting times of the random walk follow broad distributions, e.g. a power-law scaling [6]. Broad distributions of the jump length can be caused, for example, by an intermittent energy-driven directed transport of the diffusing entity; broad distributions of waiting times may arise due to an intermittent immobilisation of the diffusing entity.
Long-range correlations appear, for instance, if the path of a diffusing particle is obstructed [13], if a particle moves in a static stochastic potential or if a memory-controlled feedback coupling of the particle with its local environment exists [14].

2.2.2 Subdiffusion

For the experiments performed in the framework of the present thesis, only subdiffusion is of importance; we therefore will now concentrate on this case in the remainder. Three fundamental reasons for the appearance of subdiffusion are:
1) A random walk deviates from normal behaviour because it takes place in an environment with specific geometrical character.
2) A random walk deviates from normal behaviour in time because the time increments between two jumps are drawn from a power-law distribution and can therefore be extraordinarily long.
3) A random walk is not completely random, but is influenced by a memory, e.g. by the local viscoelastic relaxation behaviour of the embedding fluid.
In the following, these three cases will be discussed in more detail.

1) Subdiffusion due to spatial disorder – Random walks on fractals

In a 'free', unobstructed system, diffusion is normal. In a system where random obstacles are present (e.g. in disordered media), subdiffusion may appear. Simple model systems which possess all characteristics that are necessary to understand the pecularity of obstructed diffusion are so-called percolation clusters which exist as lattice and continuum models [15, 16] and have been studied extensively in computer simulations [17, 18, 13]. A convenient realisation of a percolation cluster can be obtained, for example, by simulating diffusion on a square lattice where random sites are inaccessible to diffusers and represent thus obstacles. With increasing obstacle concentration C, a cluster adopts more and more a maze-like geometry in which tracers become subdiffusive because they have to explore complex/fractal hindrances like holes, bottlenecks and dangling ends.
Due to their statistical geometric organisation, percolation cluster geometries can be described as fractals [16]. A fractal generally is a geometric object which is

self-similar on all length scales; an illustrative example would be the path of a Brownian particle: its increment lengths are statistically similar in the sense that they are described by a Gaussian distribution in all parts and on all length scales [19]. In fractal theory, very complex geometries are characterised by the single number d_F, the fractal dimension, which for a percolation cluster defines the dependency of the cluster mass $M(r)$ in a sphere on the sphere radius r via the relation $M(r) \sim r^{d_F}$ [16].

A percolation cluster typically is self-similar and fractal on length scales below a characteristic correlation length ξ that depends on the obstacle concentration C. On length scales larger ξ, the cluster becomes homogeneous (non-fractal), because here large holes exist in the obstacle distribution and finite clusters (accumulations of obstacles) can be distinguished. ξ represents the mean size of both the holes and the finite clusters. When C reaches a critical value C_P (the so-called percolation threshold), the characteristic length ξ diverges and the cluster becomes self-similar and fractal on all length scales.

Tracer diffusion characteristics in a percolation cluster are related to the fractality of the cluster. In case of $C < C_P$, tracer motion is subdiffusive at short times since the cluster is fractal over the associated short distances. A tracer here encounters the mentioned hindrances like dead ends, bottlenecks and obstructed areas. For long times, tracer motion changes to normal diffusion, since the cluster is homogeneous on large length scales. Over long distances, a continous path for lateral diffusion exists, with a long-range diffusion coefficient D for tracers that decreases with increasing C.

For $C = C_P$, the percolation cluster is fractal and self-similar on all length scales. Thus, the typical hindrances are present on all length scales, and the tracer is impeded on all length scales. Consequently, tracer motion is subdiffusive at all time scales, except for the first few steps where the tracer meets no obstacles [13]. For $C > C_P$, the tracer is trapped in a local environment and the long-range diffusion coefficient D becomes 0, i.e. the case of normal diffusion never sets in.

The strength of subdiffusion is quantified by the diffusion anomaly α and the crossover time t_{Cr} from subdiffusion to normal diffusion. Generally, α and t_{Cr} depend on the obstacle concentration as well as on shape and size of diffusers and obstacles (a small tracer for example may escape easily from an environment which confines a larger tracer). Typically, with an increasing obstacle concentration C, the anomaly α decreases and t_{Cr} increases smoothly [13]. For $C = C_P$, α becomes constant at a finite minimum value α_P while t_{Cr} becomes infinite. The conditions in nature may be best approximated by a 'Swiss-cheese' continuum percolation model, which yields $\alpha_P = 0.697$ for a two-dimensional system and $\alpha_P = 0.526$ for a three-dimensional system [20, 12].

Interrelating the quantities of a percolation cluster

The fractal and subdiffusive properties of a percolation cluster can be quantified as follows: The fractal dimension d_F of a percolation cluster measures the average mass $M(r)$ of the cluster within a sphere of radius r:

$$M(r) = \begin{cases} r^2 & \text{for } r > \xi \\ r^{d_F} & \text{for } r < \xi \end{cases} \tag{2.9}$$

where ξ is the characteristic length or correlation length above which the percolation cluster becomes non-fractal.

The *MSD* of a tracer scales as:

$$\mathit{MSD}(t) \sim \begin{cases} t & \text{for } r > R_{Cr} \\ t^{\alpha} & \text{for } r < R_{Cr} \end{cases} \tag{2.10}$$

where R_{Cr} is the crossover length to normal diffusion; α is the degree of anomaly. The parameters ξ and R_{Cr} depend on the obstacle concentration C and follow for C $\rightarrow C_P$ scaling laws:

$$\xi \sim |C - C_P|^{-\mu} \tag{2.11}$$

$$R_{Cr} \sim |C - C_P|^{-\mu+\beta/2} \tag{2.12}$$

Here, the exponent μ is defined by Equation 2.11. The parameter β gives the probability P_∞ that a lattice site is part of the infinite cluster:

$$P_\infty \sim |C - C_P|^{\beta}. \tag{2.13}$$

R_{Cr} is related to the crossover time t_{Cr} as $R_{Cr}{=}\sqrt{D(\infty) \cdot t_{Cr}}$, with D($\infty$) being the limiting diffusion coefficient for t $\rightarrow \infty$.

2) Subdiffusion due to temporal disorder

Tracers can show the characteristics of subdiffusion if they move in a system where traps or binding sites are present which immobilise them transiently [21]. The presence of just a single trap species with a specific binding energy E_B will lead to subdiffusion only for a short time period; after a crossover time t_{Cr}, normal diffusion is recovered. To cause subdiffusion for longer times, a hierarchy of multiple trap species with increasing binding energies E_B is necessary. The crossover time t_{Cr} then grows with increasing hierarchy; the crossover to normal diffusion will take place after all traps in the system were explored and occupied with tracers (the tracers are then said to have equilibrated with the traps). A suitable infinite hierarchy of traps would lead to subdiffusion at all times.
Generally, the immobilisation time t_i of a trap depends on its binding energy E_B; the two parameters are related by a Boltzmann factor: $t_i \sim \exp(-E_B/k_BT)$. An appropriate trap hierarchy to cause subdiffusion would be given for instance by a system where the binding energy of the trap species increases by dE at each level of the hierarchy; the immobilisation time accordingly would increase by a factor $\exp(-dE/k_BT)$ [22].

The diffusion coefficient D of tracers for long times, at which normal diffusion was recovered, depends on the concentration of traps in the system and is typically strongly reduced compared to systems without traps. As a consequence, an increase of the trap concentration leads to an increase of the crossover time t_{Cr}.

A mathematical description of subdiffusion due to transient immobilisation of tracers is given by the *continuous time random walk* (CTRW) [18]. A CTRW can be regarded as a random walk with a modified time scale, which means that the time increment dt between two steps is a random waiting time drawn from a suitable probability density function $w(t)$. While the resulting random walk is normal if the first moment $\langle T \rangle$ (the characteristic waiting time) of $w(t)$ is finite, the system becomes subdiffusive as $\langle T \rangle$ diverges [6, 23]. A suitable probability density yielding subdiffusion in terms of a CTRW is

$$w(t) = (1-\beta)t^{(\beta-2)}, 0 < \beta < 1. \tag{2.14}$$

Here, the degree of anomaly of the resulting subdiffusion is α=1-β [22].
A CTRW can be regarded as the mean-field description of a system where an infinite hierarchy of binding sites is present [24, 22]. The long waiting times then appear due to the existence of very deep traps in the system. A transition to normal diffusion never happens because the trap hierarchy is infinite and tracer particles never have explored a deepest trap.

3) Subdiffusion in viscoelastic systems

Subdiffusion has also been observed in viscoelastic media such as entangled polymers [1, 25, 26, 11, 27]. These media are characterised by their response to shear stress in that they dissipate part of the deformation energy like a viscous fluid, but also store part of the deformation energy like an elastic solid [1]. This behaviour appears due to extended multi-atomar structures in the viscoelastic medium [25]: The molecules in the medium are partially irreversibly shifted upon deformation (like the molecules in a fluid); partially, they are interconnected by bonds similar to the molecules in a elastic solid and can thus relax towards their original state when the deforming forces are removed. The fluid therefore has a memory that is reflected in a non-trivial creep function [28].
The thermal motion of tracer particles embedded in a viscoelastic fluid can become subdiffusive since the energy stored in the medium affects the temporal correlations of the stochastic forces acting on the particles (see Chapter 4.4 for more details). Generally, subdiffusion with $MSD \sim t^{\alpha}$, $0 < \alpha < 1$ can be expected to occur when the rates of diffusion and viscoelastic relaxation are comparable [26]. If the viscoelastic relaxation happens much slower than diffusion, a diffuser will rather behave like in an viscous fluid and show normal diffusion with $MSD \sim t$; if the relaxation happens faster than diffusion, an embedded particle will be immobilised like in an elastic environment, i.e. $MSD = 0$.

2.3 Searching a specific target via diffusion

2.3.1 The probability to approach a target via normal diffusion

A parameter of central importance for all processes in which at least one participant can freely move in solution is the ability of this participant to approach its specific target. For a normally diffusing particle, the probability to reach a defined target can be calculated analytically by considering a so-called diffuse-to-capture scenario [3]. Assuming isotropy, this scenario has spherical symmetry and can therefore be treated in spherical coordinates. In the scenario, a single target exists, being represented by a spherical absorber of radius a at position $r = 0$. Diffusing particles start from a shell source surrounding the target in a distance $r = R$. The particles are absorbed when they approach the target or when they reach a position $r > c$, with $c > R$.

Generally, in a diffusion system where sources and absorbers are present, the final distribution $C(r)$ of particles approaches a non-uniform steady-state, i.e. $\frac{\partial C}{\partial t} = 0$. The diffusion equation Eq. 2.6 therefore becomes:

$$\triangle C = 0 \tag{2.15}$$

In spherical coordinates, this equation reads:

$$\frac{1}{r^2}\frac{d}{dr}(r^2\frac{dC}{dr}) = 0. \tag{2.16}$$

In the described scenario, the particle concentration $C(r)$ has a maximum C_0 at $r = R$ and is 0 at $r = 0$ and $r = c$. With these boundary conditions, the solution of equation 2.16 becomes [3]:

$$C(r) = \begin{cases} \frac{C_0}{1-a/R}(1-\frac{a}{r}) & \mathrm{a \leq r \leq R} \\ \frac{C_0}{c/R-1}(\frac{c}{r}-1) & \mathrm{R \leq r \leq c} \end{cases} \tag{2.17}$$

With the radial flux $\jmath = -D\frac{\partial C}{\partial r}$, the diffusion current $I = -4\pi \jmath r^2$ in the system can be calculated to be $I_{in} = 4\pi D C_0 \frac{C_0}{1-a/R}$ (from the source to the target) and $I_{out} = 4\pi D C_0 \frac{C_0}{c/R-1}$ (from the source to the outer absorber). The probability P(R) of a particle starting at $r = R$ to be absorbed at $r = a$ then can be calculated to be:

$$P(R) = \frac{I_{in}}{I_{in} + I_{out}} = \frac{a(c-R)}{R(c-a)}. \tag{2.18}$$

This becomes in the limit $c \rightarrow \infty$, i.e. for particles moving in a infinite medium:

$$P(R) = \frac{a}{R}. \tag{2.19}$$

Equation 2.19 gives the probability that a diffusing particle reaches a target of radius a when it starts at a initial distance R from the target.

2.3.2 Searching via specific modes of diffusion

The efficiency with that a tracer approaches a target can increase when it moves by specific modes of diffusion, in particular when its motion is restricted to one or two dimensions or when tracers use superdiffusion instead of normal diffusion.

Reduction of dimensionality and coupled diffusion

The mean time τ for a diffuser to reach a small target of radius a in the middle of a sphere of radius L depends on the dimensionality of the diffusive search [29]:

$$\tau_1 = \frac{L^2}{3D_1} \tag{2.20}$$

$$\tau_2 = \frac{L^2}{2D_2} \cdot \ln(\frac{L}{a}) \tag{2.21}$$

$$\tau_3 = \frac{L^2}{3D_3} \cdot \frac{L}{a} \tag{2.22}$$

Here, the index i = 1,2,3 of parameters τ_i and D_i denotes the dimensionality. The parameter D_i is the diffusion coefficient in i dimensions. As the equations show, the search time τ_i is shorter for diffusers moving in one and two dimensions as compared to three dimensions, when the diffusion coefficients D_1, D_2, D_3 are of comparable magnitude. Reference [29] proposed that biological processes could benefit from this reduction of search times due to dimensionality when both targets and searchers are attached either to one-dimensional structures (e.g. a DNA strand or a microfilament) or two-dimensional structures (e.g. a membrane). The total search time then would be the sum of the mean time τ_3 (which the diffuser needs to approach the structure via three-dimensional diffusion) and the mean time τ_1/τ_2 (to approach the target via one/two-dimensional diffusion on the structure). This principle is denominated 'coupled diffusion'. Given that the diffuser binds only transiently to the structure that guarantees one/two-dimensional diffusion, the total search time also depends on the affinity of the diffuser to the structure. The total search time further is affected by the individual diffusion coefficients of the tracer in one/two/three dimensions, by the target size and also by the geometry of the low dimensional structure, since the way that the diffuser has to cover on folded or interlaced structures may be very long.

A well studied example for a biological process making use of the principle of coupled diffusion is the binding of the Lac repressor protein to DNA. Experiments show that the Lac repressor finds its specific DNA binding site faster by several orders of magnitudes than explicable with pure three-dimensional diffusion, but also faster than allegeable by pure one-dimensional diffusion along the long DNA strang. Instead, it is here a combination of transient one-dimensional diffusion due to temporary non-specific binding to the DNA (so-called sliding) and transient three-dimensional diffusion (between a release of the non-specific DNA binding and a new non-specific binding) that allows the Lac repressor to efficiently search its specific DNA binding site [30].

Searching via Lévy Flights (superdiffusion)

In several studies, searching via superdiffusive Lévy flights has been shown to be more effective than searching via normal diffusion under suitable conditions.
Lévy flights are random walks with jump lengths l drawn from a Lévy distribution $p(l)$. A Lévy distribution is a broad distribution with a diverging variance and has the shape [6]:

$$p(l) \sim l^{-1-\mu}. \tag{2.23}$$

Here, the scaling exponent must be $1 < \mu < 2$. The resulting random walk is denoted a Lévy flight and has the characteristics of superdiffusion with a mean square displacement *MSD* described by:

$$MSD(t) \sim t^{2/\mu}. \tag{2.24}$$

In the studies [31, 32, 33], normal Brownian motion and Lévy Flights were compared in their effectivity as searching strategies. It was shown that in a searching process where targets are few and fixed, the mean encounter rate is higher for diffusers searching via Lévy fligts than for tracers using normal diffusion [31]. This observation was seen to be, in principle, independent from the dimensionality of the problem [32]. For moving targets in the one-dimensional case, it was shown that the target's mechanisam of motion (Lévy/ Brown), the target density, and the relationships of both size and velocity between targets and tracers play a role. Lévy flight searching was shown to be more effective in particular for targets which are smaller and slower than the searchers and for low target densities. For the two-dimensional and three-dimensional case, one may expect a quantitative, but not a qualitative change of these observations [33].

Chapter 3

An introduction to intracellular diffusion and cell mechanics

In this chapter the current knowledge on the state of intracellular fluids and on the diffusion of macromolecules in cells is presented (Section 3.1); furthermore, available studies on cell mechanics are discussed (Section 3.2).

3.1 The mobility of macromolecules in cells

3.1.1 Functional biological macromolecules

The dominant fraction of water-soluble macromolecules with biological functions are proteins and RNA molecules. Proteins are polypeptides, i.e. polymers of amino acids joint together by peptide bonds. After its synthesis, a polypeptide chain undergoes a folding process to assume a well-defined three-dimensional structure. Once achieved, the protein structure is stable due to hydrogen bonds, hydrophobic interactions and electrostatic forces between the protein's residues. Only in the folded state a protein possesses its specific chemically active sites and therefore can perform its function [34].

Most of the soluble proteins belong to the class of globular proteins, which possess an approximately spherical shape with typical diameters in the range of 1 to 10 nm. Soluble proteins have a plethora of functions, e.g. they catalyse biochemical reactions as enzymes or act as messengers in signal transduction [34].

RNA molecules are polymers of nucleic acids. In the form of mRNA they serve as templates for proteins that are to be synthesized, but they also can have catalytic functions. In the first case, the mRNA molecules are more or less unfolded chains, in the latter case, the RNA molecules are folded to well-defined three-dimensional structures comparable to globular proteins.

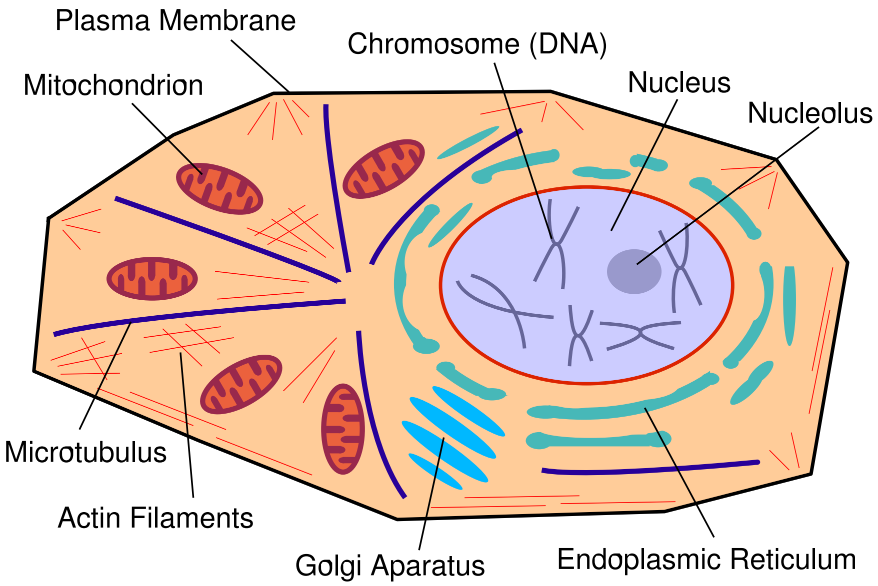

Figure 3.1: Schematic picture of an eucaryotic cell.

3.1.2 The cellular interior on the nanoscale - Macromolecular crowding

The characteristics of macromolecule diffusion in cells are determined by the constitution of the cellular interior which is a non-homogeneous, highly complex environment. Within cells, compartments and organelles, membranes, filaments, macromolecular complexes and single macromolecules occur as structuring elements on lengthscales between 1 nm and 1 μm.

A schematic drawing of an eucaryotic cell is displayed in Figure 3.1. On the micron scale, organelles like nucleus, mitochondria, chloroplasts (in plants) and the Golgi apparatus define the gross structure of the eucaryotic cell. On the 100 nm scale, the endoplasmic reticulum forms a random network across the cellular interior [35], and the constituents of the cytoskeleton (microtubuli, intermediate filaments, actin filaments) build up a dense inter-linked scaffold. All these elements influence not only the stability of cells but also the mobility of embedded objects on the respective lengthscales.

Below the 100 nm scale, i.e. in the cytoplasmic space between compartments and in the pores of the cytoskeleton, structures are defined less clearly. The intracellular space is filled up with an aqueous fluid of compartment-specific composition. The rheological properties of these intracellular fluids are determined by their large contents of dissolved biological macromolecules, i.e. of proteins, RNA molecules and sugars.

Macromolecules contribute between 5 and 40% to the total mass of the cytoplasm [36, 37, 38]. While the concentration of an individual macromolecular species can be very low, the total concentration of macromolecules ranges at very high values between 50 to 400 mg/ml. This phenomenon has been termed (macro)molecular crowding. Strong molecular crowding has several important effects both on the hydrodynamics and the thermodynamics of a system as will be described below.

Crowding occurs in all living cells, in eucaryotes as well as in procaryotes, the latter lacking most of the organelles of eucaryotic cells [39, 40]. In the nucleus, the crowding conditions may differ from the crowding conditions in the cytoplasm due to the presence of DNA molecules in different folding states and due to the existence of large macromolecular complexes like nucleoli, PML bodies and Cajal bodies. In multicellular organisms, crowding appears not only in the interior of cells, but also in the extracellular matrix of tissues. Moreover, blood plasma has a total concentration of macromolecules reaching up to 80 g/l, this concentration being an adequate cause of significant crowding effects [41].

If crowding occurs in high degrees, we can expect significant interactions of the crowder macromolecules, for example sterical repulsion. The most fundamental effect of crowding is the reduction of accessible space in a medium; this is denoted as the *excluded-volume effect.* Since dissolved molecules are impenetrable, the free space in an enclosed compartment decreases with an increasing number of dissolved molecules. For the degree of volume occupation in a solution, however, next to the number of dissolved molecules also their size distribution and shapes are important. This can be illustrated with the picture of a beaker filled with small balls of the same size: The balls will close-packed fill up only $\approx 70\%$ of the beaker's volume; but although $\approx 30\%$ of the total volume are empty it will be impossible to add an additional ball due to geometrical contraints. If now the blank space between the balls is filled with sand grains, still 10% of the beaker volume will rest empty. The blank space between the sand grains, however, again will be accessible to smaller molecules like water [42].

A rough estimate of the volume occupancy in intracellular fluids can be obtained by referring to the theoretical 'overlap' concentration of a protein solution, which is for a protein with a molecular weight of 50 kDa about 130 mg/ml [43]. This concentration is comparable to the macromolecule concentration in cells. The critical overlap concentrations for proteins and other macromolecules in the intracellular environment, however, may deviate from this value, since the different macomolecule species in cells vary in their diameters. The distribution of masses in the cytoplasm is roughly exponential [44], with proteins having weights between $\approx$ 10 - 200 kDa; and the respective diameters of proteins and RNA molecules in the folded state lie in the range of 1 to 10 nm. For an estimate of the volume occupancy in cells it has also to be taken into account that macromolecules often exist as multimers and larger complexes, e.g. as ribosomes or transcriptional complexes. Macromolecular complexes in cells were shown to have dimensions of 20 to 50 nm [45] and have to be considered as individual contributors to the intracellular crowding.

3.1.3 The diffusive mobility of macromolecules in cells

3.1.3.1 Measuring diffusion in cells

Today, mostly fluorescence methods are used to determine the intracellular mobility of macromolecules. In order to do so, the particles of interest have to be labeled individually with fluorophores to visualize their positions. Fluorophores are molecules that emit light upon excitation with light of a specific wavelength. The term 'excitation' means that the fluorophore absorbs the energy of an incoming photon by transferring an electron from the ground state S_0 to the singlet state S_1. After a lifetime of few nanoseconds, the electron relaxes from the S_1 state to the S_0 state, which is accompanied by emission of energy in form of a fluorescence photon. The wavelengths of the excitatory photon and the emitted photon typically are different due to the subdivision of both the S_0 state and the S_1 state into various niveaus of vibration. An electron typically is excited from a low S_0 niveau to a high S_1 niveau. Here, it falls under generation of phonons to the energetically lowest S_1 niveau within a time of about 1 ps. The relaxation of the electron to the S_0 state then happens from the lowest S_1 niveau to a high S_0 niveau, with the consequence that the wavelength of the emitted photon is red-shifted to a lower energy (Stokes-shift). The Jablonski diagramm in Figure 3.2 illustrates of the described electron transitions.

The S_1 state is a singlet state, which means that the net spin of the involved electrons is zero. Due to excitation by other means than photon absorption, electrons in the excited S_1 state can, with a certain probability, convert to a excited triplet state T_1 where the net spin is 1 (intersystem crossing). An excited electron that has undergone a transfer to T_1 then relaxes from T_1 to S_0 which typically happens on a time scale of 0.1 - 10 μs. The emission of strongly red-shifted fluorescence photons may be observed here but can be neglected because the photon yield of the transition from T_1 to S_0 is very small. For imaging, the existence of triplet states means that fluorophores may become transiently invisible since they can not be excited while they are in the T_1 state.

Fluorphores only have a limited physical life. After repeated excitation (or excitation with light of a high intensity), so-called photobleaching takes place, which denotes the irreversible photochemical destruction of the fluorophore. In other words, the dye changes its molecular structure to a non-fluorescent state. A fluorophore typically can emit a maximum number of 10^6 - 10^9 photons on average upon light excitation before it is destructed [46].

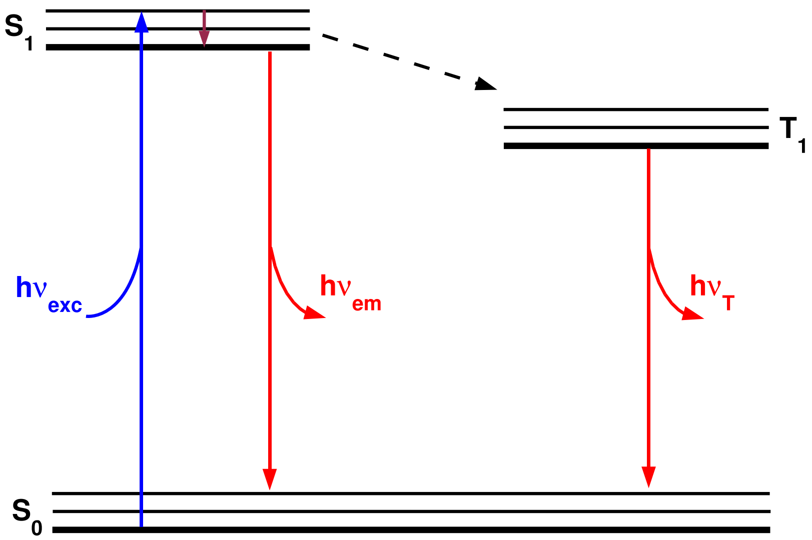

Figure 3.2: Jablonski diagramm, illustrating the electron transitions in a fluorophore. Upon excitation with a photon of energy $h\nu_{exc}$, an electron is transferred from the ground state S_0 to the excited state S_1. From here, the electron either directly relaxes to S_0 under emission of a photon of energy $h\nu_{em}$, or transiently is converted to the triplet state T_1. The yield of photons with an energy $h\nu_T$ emitted due to the transition $T_1 \rightarrow S_0$ is typically very small.

The labeling of biological macromolecules with fluorophores in order to visualize their positions can be done by several methods:
a) Chemical binding of fluorophores. To do this, the macromolecule of interest must be available in a purified form; the labeling is done in vitro and the labeled macromolecules has to be introduced into cells (e.g. injected) before the measurements.
b) Using antibodies which carry a fluorophore and bind specificly to the macromolecule of interest. This can be done, at least in principle, in vivo.
c) Genetic modification. The genetic sequence of a biological fluorophore such as the green fluorescence protein (GFP) is added to the beginning or end of the sequence of the macromolecule which is to be examined. When the modified gene is expressed, the newly synthetised macromolecule will carry an attached GFP. This is also an in vivo labeling method.

Methods of diffusion measurement

To determine the mobility of fluorescent particles, several standard techniques are available. Each method is appropriate for a certain concentration range of fluorescent particles, and each method determines the mobility on a specific length scale and time scale.

- *Single Particle tracking microscopy* SPTM
In SPTM, the positions of individual fluorescent particles, e.g. single fluorophores, are recorded with a laser scanning microscope or camera [47, 48]. This means that SPTM directly monitors the time-dependent path of a moving particle in three dimensions, from which the particle's characteristics of motion clearly can be recognised, including normal diffusion and anomalous diffusion, directed transport or transient particle immobilisation. SPTM therefore is largely independent of fit models, in contrast to other methods of diffusion measurement like FRAP or FCS. A disadvantage of SPTM is that visible particle traces often are short due to photobleaching. Therefore, averages over multiple traces have to be taken to yield evaluable data [49], which may be related to a loss in local information. SPTM works best at very low concentrations where the recognition of single particles is possible. The technique can be used to determine molecular motion on lengthscales down to tens of nanometers and on timescales down to tens of microseconds.

- *Fluorescence recovery after photobleaching* FRAP
In FRAP the fluorescence in a selected region of the sample is deleted by bleaching the fluorophores irreversibly with laser light of high intensity. Diffusion then leads to a replacement of the bleached particles in the region of interest with unbleached particles and thus to a recovery of the fluorescence intensity in the bleached region. By recording the fluorescence recovery curve and fitting it with an analytical function, diffusion coefficients and binding kinetics can be quantified [50].
FRAP works best with millimolar concentrations of fluorescent particles and measures diffusion on a lengthscale of micrometers and on timescales larger than 100 microseconds. The method has some limitations: First, it typically determines only the two-dimensional diffusion coeffient in the plane of the sample perpendicular to the optical axis. The laser beam bleaches the sample over its entire thickness, and thus the recovery curve of the bleached area contains no information in three dimensions. Next, FRAP suffers from the intrinsic technical limitation that bleaching and scanning take a finite time [51]. Furthermore, the interpretation of FRAP curves depends critically on the model that is used for data evaluation [51]. Although FRAP is in principle able to detect anomalous diffusion it is not very sensitive to do so because the deviations in the shape of the recovery curve induced by anomalous diffusion are often not easy to identify [52].

- *Fluorescence correlation spectroscopy* FCS

In FCS, the fluorescence intensity from a very small observation volume in the sample is recorded. Due to the motion of fluorescent particles into and out of the observation volume the fluorescence shows fluctuations in time. An autocorrelation analysis of the fluorescence curve reveals the characteristics of the fluctuations and thus the characteristics of the particles' motion. FCS allows to quantify directed motion as well as diffusion, including the recognition of anomalous diffusion; also binding kinetics can be determined. For a detailed introduction into FCS, see Chapter 4.

FCS works best at nanomolar fluorophore concentrations and measures diffusion on a lengthscale below micrometers and on timescales between one microsecond and one second. The need of low fluorophore concentrations can be problematic – especially for measurements in cells where concentrations often are rather high when fluoroscent proteins are expressed from modified genes. Another disadvantage of FCS is the possible distortion of the measurement curves due to processes that give rise to additional fluorescence fluctuations; here in particular the transitions of fluorophore electrons into the triplet states contribute. Also the dependence of FCS on fit models can be problematic since fitting sometimes does not allow a clear assignment of FCS data to a specific mode of motion. Compared to other measurements methods of diffusion, FCS allows local measurements in specific regions of a specimen, whereas FRAP rather detects long-range diffusion coefficients; with SPTM in an optimal case the detection of both short- and long-range coefficients is possible.

- An alternative approach for measuring diffusion of a fluorescent species is to monitor by video recording the spreading of an ensemble of fluorescent molecules into a compartment that initially was free from fluorescence [53]. This method is limited to very specific applications because typically the fluorescent species is already present in the compartment of interest and does not enter it in a spreading process.

- Non-fluorescent techniques to quantify diffusion are magnetic resonance methods, e.g. nuclear magnetic resonance (NMR) [54] and electon spin resonance (ESR) [55, 56]. With these techniques, translational and rotational diffusion of spin-labeled probes such as small molecules can be measured. However, NMR and ESR are much less sensitive than fluorescence methods and do not permit cell-level spatial resolution.

3.1.3.2 Experimental studies on the mobility of macromolecules in cells

Intracellular Viscosities
For the interpretation of particle diffusion measurements, it is important to know the viscosity of the embedding fluid. Measuring the viscosity of the intracellular fluid by monitoring the viscosity-dependent fluorescence intensity ratio of the fluorophores Cy3/Cy5 [57] showed the viscosity of the solute in cells not to differ significantly from free water. Time-resolved anisotropy measurements detected the picosecond rotational correlation times of the fluorophore BCECF and other nano-sized solutes to be not much smaller in the cytoplasm than in diluted solutions. This indicates that the fluid-phase viscosity of the cellular interior is not much larger than that of water [58]. However, one should bear in mind that in the mentioned studies the viscosity of a thin solvent shell around the fluorophores is probed; on larger length scales, the viscosity might change.

FRAP studies on diffusion
The diffusion of fluorescent labeled particles in cells was examined in FRAP studies since the 1980s. Various investigations on proteins with radii between 1.6 and 6.1 nm showed generally a reduction of the diffusion coefficients by factors 2 to 10 compared to a dilute solution [59, 60]. A correlation of the mobility with the protein radius could not be detected in these experiments [61].
FRAP studies on differently sized dextran and ficoll molecules (inert tracer particles) with effective hydrodynamic radii between 1 and 45 nm highlighted a reduction of the diffusion coefficients in cells compared to water by factors from 1.1 to 70, dependend on the tracer species and the cell type [62, 63, 53, 64, 65]. Several studies determined a clear size-dependence of the diffusion coefficients (i.e. the diffusion coefficients decreased with increasing particle radii) [63, 53, 64] whereas the study [65] reported no size dependence for particles with radii $<$ 20 - 30 nm and a strong impairance for the diffusion of larger particles.
Since previous measurements indicate that the intracellular viscosity is similar to that of water, the reviews of Luby-Phelps [61] and Verkman [58] suggest the possible reasons for the reduction of nanoparticle diffusion in cells to be either collisions with intracellular macromolecules (crowding), sieving by intracellular networks (in which for example the cytoskeletal actin could be involved) or transient binding to intracellular structures.

FCS studies on diffusion
Since the 1990s, FCS became available for diffusion measurements in living cells. Compared to FRAP, FCS has an improved temporal and spatial resolution and allows explicitly the detection of anomalous diffusion dynamics.
An early FCS study [66] measured the diffusion of latex test beads (diameter 7

and 15 nm) in cells to be slowed down about 2-fold compared to water, which is similar to the results of FRAP experiments. More recent FCS studies measured not only a reduction of diffusing coefficients for nano-sized tracers, but detected also the appearance of subdiffusion in weak degrees for GFP [67] and in strong degrees for dextran tracers with effective hydrodynamic radii between 1.8 to 14.4 nm [44]. The authors of these studies suggested subdiffusion to be caused by tracer obstruction due to macromolecular crowding. This is in agreement with the percolation theory, which shows tracers to be subdiffusive in environments containing random obstacles in large concentrations (c.f. Section 2.2.2). In this interpretation, the cellular interior on the nanoscale would have to be regarded as a disordered medium of fractal geometry, due to macromolecular crowding. FRAP measurements in comparison may detect rather the long-time and long-range influence of crowding on diffusion, which consists – again in agreement with percolation theory – in a reduction of the diffusion coefficient D.
The authors of [44] further proposed the anomaly degree α of subdiffusion to be a measure for the 'crowdedness' of a fluid. In agreement with Reference [44], an in vitro study showed by means of FCS that the diffusion of streptavidin proteins was subdiffusive in artificially crowded solutions that resemble the intracellular environments [68].

SPTM studies on diffusion
In a SPTM study, RNA-protein complexes (diameter about 100nm) were determined to show subdiffusion in the cytoplasm of E.coli bacteria [69]. In mutants lacking some cytoskeletal proteins, no significant change of the subdiffusive behaviour was observed, indicating that it was independent from the cytoskeleton. Thus, the authors suggest in agreement with Reference [44] macromolecular crowding as reason for the observed subdiffusion.

3.1.3.3 Implications of subdiffusion

It was described above that several studies detected macromolecules to show subdiffusion in cells and consistently explained this observation in terms of a fractal nanoscale geometry of the cytoplasm due to macromolecular crowding [67, 44, 68, 69]. Both, subdiffusion of molecules and the appearance of a fluid as a fractal disordered medium would have consequences on several processes relevant for biology, in partiular on binary and enzymatic reactions, and on pattern formation.

Chemical reactions in disordered media
The kinetic rate coefficients k_i of a chemical reaction are generally described in terms of classical mass-action laws. In this context it is typically assumed that a reaction takes place in a well-stirred solution; the rate coefficients therefore depend

only on the effective concentrations of the reactants. If a reaction takes place in a badly stirred solution, however, where mixing of the reactants is limited by diffusion, the kinetic rate coefficients k_i depend also on the diffusion coefficient D_i of the reactants. For elementary chemical reactions of the type $A + B \rightarrow C$ in a three-dimensional system, the kinetic rate coefficient k (which relates the reaction rate r to the educt concentrations c_i by the expression $r = kc_A c_B$), is $\sim D$ for $t \rightarrow \infty$, i.e. k does not depend on t [70].

In disordered media the rate coefficients k_i of diffusion-limited reactions are altered and the description via mass-action laws fails. For reactions of the types $A + A \rightarrow C$ and $A + B \rightarrow C$, k decays with time: $k \sim t^{-h}$, $0 \leq h \leq 1$. In contrast, for a homogenous environment, i.e. a well-stirred, diffusion-independent three-dimensional systems, $h = 0$ [71]. Kinetics of this type are referred to as fractal-like kinetics [72]. They appear due to the subdiffusive spreading of particles in disordered media: Reactants stay on average for a prolonged time period close to their initial positions, hence being able to react quickly with near reaction partners. The period needed to encounter reaction partners in distant regions, however, increases with enhancing distances; therefore, k becomes time-dependent. Under appropriate conditions, even a segregation of reactants in only-A and only-B regions can take place for a reaction of the type $A + B \rightarrow C$ [72].

Fractal kinetics in disordered media are also reflected in an increase of the reaction order x compared to homogeneous media. The reaction order x specifies the dependence of the rate r on concentrations. E.g. for $A + A \rightarrow C$: $r \sim c_A^x$ with $x = 2$ for a homogeneous environment, $x = 2.5$ for a percolation cluster [72].

The influence of subdiffusion on chemical reactions dependent on the activation energy

Subdiffusion does not necessarily lead to a slowdown of chemical reaction rates. The studies [73] and [74] examined by computer simulations the rates of diffusion-limited chemical reactions (A+B $\rightarrow$ C) with different activation energies on percolation clusters. 'Fast' reactions with low activation energies (i.e. reactions in which typically a high percentage of reactant collisions yields products) were detected to be decelerated due to reactant subdiffusion. This deceleration of reactions was observed to be weaker in reactions with higher activation energies, that is, a lower reaction probability at the first encounter of reactants.

In contrast, reactions with very high activations energies were seen to be accelerated slightly as a consequence of reactant subdiffusion, with the rate of product formation being almost independent of the obstacle concentration in the percolation cluster. The explanation for these observations can be found in the fact that reactant subdiffusion manifests in two basic effects:

a) An increase of the time needed for the first collision of two reactants; this causes the deceleration of 'fast' reactions.

b) An increase of the time for reactant separation after a unsuccessful collision;

this yields a higher rate of recollision and accelerates therefore 'slow' reactions.

Enzymatic reactions on two-dimensional percolation clusters

A typical function of proteins is to act as enzymes. An enzyme E catalyzes the specific chemical reaction of one or more substrate molecule S to a product P. Generally, the kinetics of an enzymatic reaction is modeled by the Michaelis-Menten scheme $E + S \rightarrow C \rightarrow P$ [75]. This formalism is based on classical mass action laws that assume constant kinetic rate coefficients. The study [76] showed by Monte Carlo simulations that on 2-dimensional percolation clusters the Michaelis-Menton description of enzymatic activity fails. The kinetic rate coefficients become time-dependent due to subdiffusion of the reactants, in agreement with [72]. Furthermore, a segregation of substrates and products in the cluster was detected at high obstacle densities. The author suggests this segregation to be a possible mechanism for self-organisation in biological membranes.

The influence of subdiffusion on pattern formation

The development of regular patterns is an ubiquitous phenomenon in biology [77]. Patterns determine for instance the optical appearance of animal skins (e.g. for tigers, zebras, butterflies) [78] and the structure of plant or shell surfaces [79]. Furthermore, basic functions of organisms depend on the pattern-like organisation of molecules: an example is the formation of a cellular mid plane by specific proteins during the cell division of E.coli bacteria [80, 81].

Alan Turing proposed in 1952 a mechanism for the spontanous formation of stable patterns which might for example play a role in embryogenesis [82]; mechanisms related to that of Turing were suggested to play a role in several biological processes based on pattern formation. A Turing model is given, for instance, by a reaction-diffusion system consisting of two substances: an activator that generates more of itself by autocatalysis and an inhibitor which is activated by the activator and inhibits the autocatalytic generation of the activator. If in such a system the inhibitor diffuses faster than the activator structures may appear which are stationary in space and in time ('Turing patterns'); in other words, regions occur in the system where only activator or only inhibitor exists [77].

In a recent study, the dependence of Turing pattern formation on particle numbers was investigated for an activator-inhibitor system [83]. It was shown here that for normal diffusion of the reactants relatively high particle numbers might be necessary for the formation of stable patterns. However, the Turing pattern formation was seen to become more stable even for very low particle numbers when the activator particles moved by subdiffusion. From the biological aspect, this effect could be important for pattern formation in cells where particle numbers naturally are limited.

3.1.4 Thermodynamic effects of crowding on biological mechanisms in cells

In addition to the hydrodynamic effects described above, crowding also influences the thermodynamics of a system, thus affecting biological, chemical and physical processes. From the perspective of thermodynamics the restriction of a particle's free mobility due to volume exclusion has the consequence of an entropy reduction in the system. When the total concentration of macromolecules rises, the configurational entropy of each macromolecular species decreases, and its contribution to the total free energy of the system grows. Consequently, processes will be driven that lead to an increase of the available volume and hence cause an entropy increase of the system.

The effects of crowding on reaction processes can be studied experimentally by working in artificially crowded environments, e.g. in fluids where crowding agents like BSA proteins or dextrans are present or in silica matrices [84]. For a specific (bio)chemical reaction, the thermodynamic effects of crowding become clear when the equilibrium constant K is calculated under consideration of the crowded environment. Let us consider a generalised reversible reaction in solution:

$$e_1 E_1 + e_2 E_2 + ... \longrightarrow p_1 P_1 + p_2 P_2 ... \tag{3.1}$$

Here, e_i is the stoichometric coefficient of the educt species E_i and p_i is the stoichometric coefficient of the product species P_i. The equilibrium constant of the reaction is calculated as:

$$K = \frac{a_{P_1}^{p_1} \cdot a_{P_2}^{p_2} \cdot \dots}{a_{E_1}^{e_1} \cdot a_{E_2}^{e_2} \cdot \dots} \tag{3.2}$$

In this equation, the coefficients $a_{E_i/P_i} = V_{E_i/P_i} \cdot c_{E_i/P_i} / V^{tot}$ denote the effective concentrations (or thermodynamic activities) of the educts/products, depending on the available volume V_{E_i/P_i} per educt/product molecule, the actual concentrations c_{E_i/P_i} and the total volume V^{tot}. Via a_{E_i/P_i}, the equilibrium constant directly depends on the crowding conditions which define V_{E_i/P_i}. As a general effect, such calculations show that crowding supports a) the association of macromolecules and b) the conformational compaction of indiviual macromolecules, since both processes cause an increase of the available volume in the system and are thus entropically favored.

In more detail, specific effects of crowding were highlighted already for a large number of explicit examples from biology [85]. Studies on protein folding and stability, for instance, demonstrated that conformational changes that increase the volume of a molecule (such as protein unfolding) are prevented in a crowded environment, while conformational isomerisation reactions from expanded or aspherical conformations to more compact and spherical conformations are supported [42]. A protein will therefore be stabilised against denaturation by heat, cold or denaturant, if high concentrations of stable crowder macromolecules are present [86, 87, 88]. In several studies, the formation of aggregates and protein multimers was found to be supported by crowding; examples for this include the self-assocation of an n-mer from monomers [42], Haemoglobin assembly [89, 90] or the association of the 50s and 70s ribosomal subunits [91]. As another effect crowding was shown to enhance the activity of some chaporenes (specific proteins that support the folding process of other proteins). This may happen either to compensate a possible interference of crowding with folding (since crowding favours the aggregation of unfolded proteins) or be caused by a stronger cohesion of chaperones in a crowded environment [92, 93]. In the context of the organisation of the cytoskeleton, it was suggested that crowding could induce spontaneous alignment and bundling of self-assembled filaments, which may happen because orientational ordering can change the available volume for large and elongated macromolecules [94]. As a further effect of crowding, the enhancement of the rate and the extent of the formation of fibrous or rod-like protein assemblies was highlighted [86]. Crowding also has implications for genome structure and function because it influences both the structural organization of DNA and the interactions between DNA and proteins [37, 95]. Furthermore, crowding is an important factor in the compensation mechanisms which protect essential macromolecular interactions in E. coli bacteria against strong changes in the tonicity of their surrounding [40]. And as a last implication, it shall be mentioned that crowding also can cause the reversal of biochemical reactions. In this context, studies indicate that in a crowded environment enzymes preferably may synthesise polypeptides instead of catalysing peptide hydrolysis like they would do in a dilute solution [96].

3.2 Mechanical properties of cells and cell constituents

The stability and the rheological behaviour of a material is typically determined either a) by measuring its response to deformation with weak forces or b) by observing the passive thermal fluctuations of embedded probe particles which directly are influenced by the rheological properties of their environment. To measure the mechanical behaviour of cells, various techniques have been developed. Experiments that measure the response of entire cells to deformation are, for example, micropipette aspiration [97, 98, 99]; atomic force microscopy (AFM) [100, 101, 102]; microplate manipulation [103]; microneedles [104, 105]; magnetic bead microrheometry [106]; magnetic tweezers [107], and magnetic twisting cytometry [108].

Since these various methods apply different types of deformations to cells and the deformation happens at different strengths, rates and lengthscales, the various techniques elicit different responses from cells. To interprete the measurements appropriate models have to be used [109]. Leucocyte cells which are aspired by a micropipette with a large diameter, for example, can be described by a liquid drop model [110] whereas cells that are aspired by a micropipette with a small diameter could be approximated as an incompressible elastic half-space [111]. As the various measurement methods and models differ strongly, a comparison between their observations is often complicated. A fundamental finding of all techniques, however, is that cells show viscous and elastic properties, and can thus be described as viscoelastic materials.

Of particular interest are studies that determine the viscoelastic behaviour of cells in terms of a frequency-dependend complex shear modulus $G(\omega) = G'(\omega) + iG''(\omega)$ (c.f. Section 4.4 for a more detailed introduction). In several studies, entire cells were investigated over large frequency ranges by magnetic twisting cytometry [112, 108] or AFM [102]. Here, $G(\omega)$ was detected to follow a weak power-law $G(\omega) \sim \omega^x$ with x lying between 0.1 and 0.4. The elastic contribution G' of $G(\omega)$ was slightly stronger than the viscous contribution G'', but both were of a similar magnitude.

While References [108] and [102] tested the mechanical behaviour of cells by applying forces to the cellular surface, a recent study measured non-invasively the mechanical stability of the cellular interior over 5 decades in ω by observing the thermal fluctuations of Brownian particles (diameter 100 nm) in the cells [11] (c.f. Section 4.4 for a detailed description of the method). Here, a power-law scaling of $G(\omega)$ was detected with $x \approx 0.75$; elastic and viscous moduli were of similar strength. These power-laws of $G(\omega)$ as measured outside the cell [108, 102] and inside [11] are comparable. The viscoelastic behaviour of entire cells as measured in the described studies seems to be determined mainly by the cytoskeleton since a disruption of cytoskeletal elements was seen to cause a decrease only of the elasticity and an increase of the viscosity, i.e. to soften the cell [11, 108].

Most measurement methods only allow one to determine the global cell stability. Examining the stability in different intracellular regions is a challenging task but can, for example, be done by the method of detecting the local thermal fluctuations of Brownian particles which was mentioned already. Reference [11] demonstrated using this technique that subcellular regions of the cytoplasm, in particular the lamella and the perinuclear region, exhibit large differences in stiffness. In a similar study the interior of the nucleus was explored by tracking artificially introduced nanospheres (diameter 100 nm), with the result that the nucleus interior is also viscoelastic yet stiffer than the cytoplasm [113].
Another method to probe the mechanical characteristics of intracellular elements is to isolate them and probe them in vitro. Reference [114] measured the viscoelastic behaviour of solutions of purified actin, mimicking physological conditions, and detected a power-law scaling $G(\omega) \sim \omega^x$ with $x = 0.15$ and the elasticity G' dominating over the viscosity G''. These dynamics are qualitatively similar to the measurements on entire cells of Reference [108], yet the absolute values of $G(\omega)$ differ strongly (by four orders of magnitude). In another study, actin solutions were shown to exhibit a dynamical behaviour $G(\omega) \sim \omega^x$, $x \approx 0.75$ [115] which is consistent with the findings in the interior of cells of Reference [11]. In agreement with this, similar measurements reported by Reference [116] in actin solutions can be interpreted as $G(\omega) \sim \omega^x$, $x \approx 0.75$. In a distinct study, isolated nuclei of artificial chondrocyte cells were shown by micropipet aspiration to be viscoelastic, with the specific characteristics of being stiffer and more viscous than intact chondrocyte cells [117]. The peculiar stability of the entire nucleus might be assigned to its shell, the lamina-supported nuclear envelope [118] and to a putative nucleoskeleton [119].

In several studies, the viscoelasticity of various cell lines was measured and compared. These examinations highlighted that different cell types qualitatively show the same viscoelastic behaviour, but differ in their individual values for $G(\omega)$ [108]. Reference [120] measured the deformabilty of single suspended cells in an optical stretcher and detected a cell's $G(\omega)$ to be related to the cell type and the cell's state of development and disease. This finding can be explained with the close relation of structure/composition of the cytoskeleton to the cell metabolism.
Measurements which compared the viscoelasticity of healthy cells and their cancerous counterparts showed that elasticity and viscosity were reduced in malignant cells [121, 103, 122]. The greatest reduction of the rigidity was found in metastatic cancer cells [121, 123] which might facilitate their entry into the lymphatic system or the blood circulation to reach target organs [124]. Also, red blood cells that were infected with the malaria parasite were in micropipette aspiration experiments shown to be stiffer than healthy red blood cells [109].

Chapter 4

Measuring molecule diffusion with Fluorescence Correlation Spectroscopy (FCS)

In this chapter the measurement methods used for the present thesis are introduced. In the Sections 4.1, 4.2 and 4.3 Fluorescence correlation spectroscopy is presented in detail as a technique to determine the diffusion of dissolved fluorescence-labeled molecules; an introduction to the theoretical background is given as well as a description of the experimental setup. In Section 4.4 the technique of Mason & Weitz to determine the rheological properties of a fluid from diffusion measurements on embedded probe particles is presented.

4.1 A general introduction to Fluorescence Correlation Spectroscopy

Fluorescence Correlation Spectroscopy has been developed in the early 1970s [125, 126, 127, 128, 129, 130]. It is a method to analyse the properties of dissolved fluorescent molecules with high temporal and spatial resolution. The parameter of interest in FCS is not the fluorescence intensity itself (like in other fluorescence techniques like FRAP), but rather temporal fluctuations of the fluorescence. By determining the typical behaviour of the fluctuations in time (i.e. their strength and duration) via the fluorescence autocorrelation, the characteristics of the underlying processes which cause the fluctuations can be determined.

In principle, all physical parameters which give rise to fluorescence fluctuations are accessible to FCS [131]. Typically, the technique is used to investigate the mobility of fluorescent molecules. In a system of mobile fluorescent molecules, fluorescent fluctuations occur due to the continuous entry and exit of molecules into and out of the FCS detection volume. A quantitative autocorrelation analysis of the

fluctuations thus reveals a) the molecule concentration and b) the mode and the dynamics of the molecular motion.
Indeed, FCS allows one to discriminate between directed transport and diffusive motion, to characterise different types of diffusion (normal diffusion, anomalous sub-/superdiffusion, rotational diffusion) and to recognise multiple species with different mobilities. In the case of transient binding of diffusing molecules to immobile structures, the rates of the on/off kinetics can also be detected. The field of application for FCS is very broad because the technique allows one to examine a plethora of processes that are related to the mobility of molecules. For instance FCS can detect conformational changes of diffusing molecules [132] or their binding to other mobile objects [133] because both are related to a change of the molecule's hydrodynamic radius and thus to its mobility. Also a molecule's binding to a membrane is reflected in a change of its diffusional behaviour and thus detectable in FCS [134]. In the present work, conclusions on the rheological properties of its embedding medium will be made from a test particle's mobility as measured with FCS.

A central aspect of FCS is to work close to the single molecule level. This is important because the relative fluctuations of the particle number in the detection volume, which are used for the autocorrelation analysis, decrease as the particle number rises. In large ensembles, the relative fluctuations are thus masked by unavoidable background noise. An adequate reduction of the molecule number to yield large fluctuations is achieved by using small detection volumes in FCS and by peforming measurements in highly diluted solutions, i.e. nanomolar concentrations.

Perturbations of FCS mobility measurements come from all processes which change the light emission of a fluorophore during the measurement and thus destroy the assumption that fluorescence fluctuations appear only due to the change of the number of fluorescent molecules in the observation volume. Such disturbing processes can be, for example, electron transitions in the fluorophore or conformational transitions of the fluorophore due to a certain chemical environment. These interferences must be either excluded in the system under investigation, or the FCS measurements must be corrected for them, which is possible for example in the case of electron transitions into non-fluorescent triplet states.

4.2 Molecule statistics in diluted solutions

To demonstrate why FCS - as a technique to analyse molecule number fluctuations - depends on working at low molecule concentrations, the particle statistics in a diluted solution is considered.
When we regard a closed system of the volume V_0, the total number N_0 of dissolved molecules is constant. The molecule number inside a small open volume $V < V_0$ in the system - which can be for example the optically defined observation volume

used in fluorescence techniques like FCS - is constant on average but fluctuates with time, due to the self-diffusion of molecules through the observation volume. The probability $p(N)$ that at a particular time t exactly N molecules can be found inside V is given by a binomial distribution, which approximates for small V and large N_0 a Poisson distribution:

$$p(N) = e^{-\langle N\rangle} \cdot \frac{\langle N\rangle^N}{N!} \tag{4.1}$$

The Poisson distribution is characterised by the fact that its mean value and its variance are equal:

$$\langle N\rangle = \langle \triangle N^2\rangle \tag{4.2}$$

In order to maximise the detected relative fluctuations $\frac{\sqrt{\langle \triangle N^2\rangle}}{\langle N\rangle}$, it is therefore desirable to reduce the mean particle number $\langle N\rangle$ in FCS, since:

$$\frac{\sqrt{\langle \triangle N^2\rangle}}{\langle N\rangle} = \frac{1}{\sqrt{\langle N\rangle}}. \tag{4.3}$$

Relation 4.2 can also be expressed in terms of concentrations, with $\langle C\rangle = \frac{\langle N\rangle}{V}$ being the average molecule concentration in the observation volume V and $\langle \delta C^2\rangle = \frac{\langle \triangle N^2\rangle}{V^2}$ being the variance of the concentration:

$$\langle \delta C^2\rangle = \frac{\langle C\rangle}{V}. \tag{4.4}$$

For an infinitesimal volume element d^3r at position $\vec{r}$, Equation 4.4 can be expressed with the Dirac δ-function as [126]:

$$\langle \delta C(\vec{r},t)\delta C(\vec{r'},t)\rangle = \langle C\rangle\delta(\vec{r}-\vec{r'}). \tag{4.5}$$

The δ-function has the dimension of a reciprocal volume and replaces $1/V$. According to Equation 4.5, the concentration fluctuations at two different loci $\vec{r}$ and $\vec{r'}$ at a fixed time point t are statistically independent from each other. This will become particularly important for the calculation of the autocorrelation function of the concentration fluctuations in Section 4.3.2.

4.3 Measurement procedure and technical background of FCS

The fundamental approach in FCS is as follows: A small laser spot is placed on the locus of interest, e.g. in a solution or in a living cell containing fluorescent molecules. Then, the fluorescence intensity from the spot is recorded as a time series. The fluorescence will be constant on average but will show stationary fluctuations (provided that disturbances of the measurement are excluded). From the temporal fluctuations the autocorrelation function is calculated, which has typically the shape of a decay curve (see derivation in Section 4.3.2). To get the parameters of interest, e.g. the diffusion coeffiecient of the examined molecule species, the autocorrelation curve is fitted with an appropriate theoretical expression.
In the following chapters, the basic physics and the experimental realisation of each of the measurement steps will be described.

4.3.1 Recording of fluorescence

To yield a fluorescence signal from an ensemble of fluorescent molecules, the fluorophores have to be excited by illumination light of an appropriate wavelength. The emitted fluororescent light from the fluorophores then is guided to a detector which records its intensity.

Confocal alignment
For FCS measurements typically a confocal microscope is used. In contrast to conventional widefield fluorescence microscopy where the entire specimen is illuminated, confocal microscopy works with a point illumination. This can be achieved by using a laser as a light source. The laser beam is focussed to the specimen (the object) by an objective lense. Due to diffraction, the laser focus appears not as a mathematical point but represents a focus volume V_C, which has – according to Abbe's resolution limit – an estimative diameter $\omega_0 = \frac{\lambda}{2NA}$. In this formula, λ is the illumination light wavelength. The parameter $NA = n \cdot \sin\beta$ denotes the numerical aperture, with n being the refractive index of the specimen and β being half of the opening angle of the objective. The focus volume V_C decreases with an increasing NA, and since NA has a maximum value due to the diffraction limit, V_C always is finite. With water immersion (i.e. water is used as medium between objective and specimen, since water has a similar n as biological specimen), a high $NA > 1$ can be obtained.
Upon illumination, the specimen emits fluorescent light which is mapped by the objective lens onto a pinhole to reduce out-of-focus information and finally reaches the detector. Because the focal volumes of illumination and detection coincide, the system is denominated 'confocal'. The advantage of a confocal microscope is that

optical information from outside the midplane of the illumination focus is supressed by a) the confocal alignment of the foci and b) the supressing of light from outside the focal plane by the pinhole. Thus, the axial resolution of the system is improved compared to conventional microscopy and scattered light is avoided. The path of rays in a confocal microscope is illustrated in Figure 4.1.

For a FCS measurement the confocal volumes of illumination and detection are placed on the locus of interest, for example in a solution of fluorophores. Fluorophores inside the illumination volume are then excited proportional to the local light intensity and emit fluorescence light.

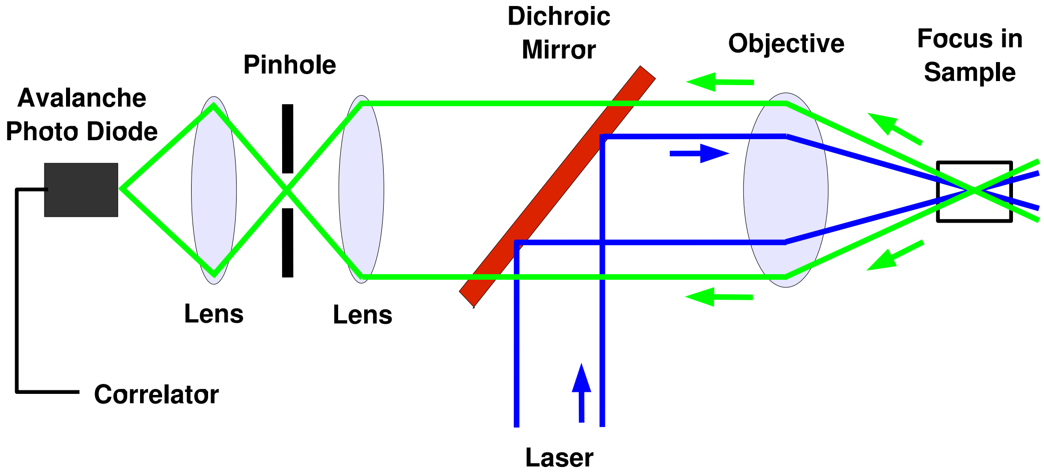

Figure 4.1: Path of rays in a confocal microscope, as used for the excitation and detection of fluorescence in a FCS measurement.

Illumination

The characteristics of the illumination volume depend on the laser beam, on the objective lens which focusses it on the specimen and on the specimen's refractive properties. The excitation laser beam works at a constant (adjustable) light intensity and has an intensity profile of Gaussian shape with a $1/e^2$ - radius ω_1. The objective lense, a complex entity containing a large number of intermediate and correction lenses, is specified by its focal distance f.

The light intensity distribution I_{exc}(x,y,z) of the illumination volume in the object space is described in radial direction (x-y-plane) by a Gaussian distribution and in axial direction (z-coordinate) by a Lorentz distribution:

$$I_{exc}(x,y,z) = \frac{\omega_0^2 \cdot I_0}{\omega(z)^2} \cdot e^{\frac{-2(x^2+y^2)}{\omega(z)^2}} \tag{4.6}$$

The width of the beam in the focal plane is $\omega_0 = \frac{\lambda_{exc} \cdot f}{n \cdot \pi \cdot \omega_1}$, where λ_{exc} is the vacuum wavelength of the illuminating laser beam and n is the diffraction index of the specimen. The beam cross subsection outside the focal plane (shifted in z-direction) is defined by $\omega(z)^2 = \omega_0^2 + z^2\omega_1^2/f^2$. I_0 is the maximum intensity of the illuminating laser beam in the beam center.

Detection

The emitted fluorescence light is collected by the objective lense and focussed on the pinhole. Only photons that come directly from the object plane can pass the pinhole. The pinhole radius L is chosen in such a manner that the image of L in the object plane and the width ω_0 of the illumination volume are equal. The combination of a high *NA* objective and the pinhole allows one, in accordance with Abbe's resolution limit, to obtain very small detection volumes of less than 1 fl.
The pinhole is mapped 1:1 on the photon detector, which is typically a single photon counting avalanche photodiode. The fluorescence intensity I_{em} is measured as the number of photons ('counts per seconds' cps) that reach the detector per time unit.

The intensity distribution $I_{em}(x, y, z)$ of the emitted fluorescence light in the detection volume as recorded by the detector depends on the illumination intensity distribution $I_{exc}(x, y, z)$, on the characteristics of the detection optics which is described by the collection efficiency function *CEF(x,y,z)*, on the photon yield of a single fluorophore per excitation intensity Q and on the total efficiency of the filters and photon counters E:

$$I_{em}(x, y, z) = E \cdot Q \cdot \mathit{CEF}(x, y, z) \cdot I_{exc}(x, y, z) \tag{4.7}$$

The product of the normalized excitation intensity $I_{exc}(x, y, z)/I_0$ and the *CEF(x,y,z)* is often denoted as molecule detection efficiency *MDE(x,y,z)*.
The photon yield Q of a fluorophore is defined as the ratio of the number of adsorbed photons to the number of emitted photons. The optical components that define the *CEF* are the objective lens and the pinhole. Thus, the *CEF* can be calculated from the objective's point spread function *PSF* and the pinhole or transmission function $T(x, y)$. The *PSF* describes the light intensity distribution in the image plane (on the detector) resulting from a point shaped light source in the object space that was mapped by the objective. $T(x, y)$ describes the restriction of light detection due to the pinhole. *PSF* and $T(x, y)$ can be expressed by disc functions in the object space [135, 136].

$$\mathit{PSF}(\vec{r}, \vec{r'}, z) = \frac{circ(\frac{\vec{r} - \vec{r'}}{R(z)})}{\pi \cdot R(z)^2} \tag{4.8}$$

$$T(\vec{r}) = circ(\vec{r}/s_0) \tag{4.9}$$

$$circ(\vec{r}/r_0) = 1 \text{ if } |\vec{r}| \leq r_0, \text{ else } 0 \tag{4.10}$$

$\vec{r}$ is the two-dimensional vector in the x-y-plane perpendicular to the optical axis. A point light source at the position $\vec{r}, z$ in the object plane is mapped into the focal plane ($z = 0$) as a disc with a radius that is determined by the resolution R_0 of the objective lense. R_0 is the radius of the first Airy disc. In planes with $z \neq 0$ parallel to the focal plane, the disc is magnified as defined by a Lorentz function:

$$R(z)^2 = R_0^2 + z^2 \cdot \tan^2 \beta. \tag{4.11}$$

$s_0 = L/M$ is the image of the pinhole radius L in the object space as generated by the objective lens with magnification M.

The *CEF* is in each plane z calculated by an integral over the area:

$$CEF(\vec{r}, z) = \frac{1}{N} \cdot \int T(\vec{r}) \cdot PSF(\vec{r}, \vec{r'}, z) d\vec{r} \tag{4.12}$$

where N is a normalization factor.

A multiplication of the *CEF* of the objective-pinhole system and the illumination intensity distribution I_{exc} shows that the pinhole modifies the resolution in direction of the optical axis. The emission characteristic $I_{em} = \kappa \cdot Q \cdot CEF(x, y, z) \cdot I_{exc}(x, y, z)$ becomes a complicated expression that can be solved only numerically. However, I_{em} can be approximated by a Gaussian in axial and radial direction, if the pinhole radius L is chosen according to the condition $\omega_0 < L < \frac{\tan\beta}{2 \cdot \tan\delta \cdot \omega_0}$ (δ is denoting the focus angle) [136]. This condition guarantees that after the passage through the optical system
a) the lateral Gaussian shape of I_{exc} is conserved and
b) the axial Lorentz shape of I_{exc} is modified in a manner that it can be approximated by a Gaussian.
I_{em} then becomes:

$$I_{em}(x, y, z) = E \cdot Q \cdot I_0 \cdot e^{\frac{-2(x^2+y^2+(z/S)^2)}{\omega_0^2}} \tag{4.13}$$

Here, $S \approx 3$ - 10 is the constant dimensionless shape factor that specifies the distortion of I_{em} in axial direction compared to the lateral directions.

4.3.2 Analysis of fluorescence intensity fluctuations

Measured fluorescence intensity signal

The fluorescence intensity signal $F(t)$ that is detected from the observation volume V depends on the intensity $I_{em}(x, y, z)$ of the light which is emitted from the position (x, y, z) and on the fluorophore concentration $C(x, y, z, t)$ in V:

$$F(t) = \int_V I_{em}(x, y, z) \cdot C(x, y, z, t) d^3 r \tag{4.14}$$

The fluorescence intensity and the concentration can be separated in the constant average values $\langle F\rangle$ and $\langle C\rangle$ and the fluctuations $\delta F(t)$ and $\delta C(x,y,z,t)$:

$$F(t) = \langle F\rangle + \delta F(t) \tag{4.15}$$

$$C(x,y,z,t) = \langle C\rangle + \delta C(x,z,y,t). \tag{4.16}$$

Autocorrelation analysis
To examine the characteristics of the fluorescence fluctuations $\delta F(t)$ an autocorrelation analysis of $F(t)$ is performed. Generally, an autocorrelation serves to clean a fluctuating variable $f(t)$ from noise and to detect a possible self-similarity in the behaviour of the variable.
The autocorrelation function of a time-dependent function $f(t)$ without constant component (i.e. $\langle f(t)\rangle = 0$) is defined as:

$$AC(\tau) = \langle f(t)\cdot f(t+\tau)\rangle = \lim_{T\to\infty}\frac{2}{T}\cdot\int_{-T}^{T} f(t)\cdot f(t+\tau)dt \tag{4.17}$$

The meaning of this mathematical operation is that each time point t_0 of $f(t)$ is compared with each later time point $t_0{+}\tau$, for $t_0{=}t_{min}\rightarrow t_{max}$, $\tau = 0 \rightarrow t_{max} - t_0$. Autocorrelation therefore highlights the self-similarity of $f(t)$ for a certain increment τ, which only exists if $f(t)$ contains a meaningful information and not just random numbers. The autocorrelation function $AC(\tau)$ then describes the temporal decay of the information transported in $f(t)$. For a periodic signal, $AC(\tau)$ is also periodic, while for an event limited in time, $AC(\tau)$ decays from a maximum to zero.

The normalised autocorrelation function of the fluorescence intensity $F(t)$ is:

$$AC(\tau) = \frac{\langle F(t)\cdot F(t+\tau)\rangle}{\sqrt{\langle F(t)^2\rangle\langle F(t+\tau)^2\rangle}} \tag{4.18}$$

With the Equations 4.14, 4.15, 4.16, the numerator of 4.18 becomes:

$$\langle F(t)F(t+\tau)\rangle = (\overline{C}\cdot\int_V I_{em}dV)^2 + \int_V\int_{V'} I_{em}(\vec{r})I_{em}(\vec{r'})\langle\delta C(\vec{r},t)\delta C(\vec{r'},t+\tau)\rangle dVdV' \tag{4.19}$$

Here, the first term is a constant and the second term is the autocorrelation function of the fluorescence fluctuations, $\langle\delta F(t)\cdot\delta F(t+\tau)\rangle$. It depends on the intensity profile of the illuminating laser I_{exc} and on the autocorrelation function of the concentration fluctuations $\langle\delta C(\vec{r},t)\cdot\delta C(\vec{r'},t+\tau)\rangle$.

Autocorrelation function for one diffusing particle species

If concentration fluctuations $\delta C(\vec{r},t)$ arise due to diffusion, the autocorrelation function of δC can be calculated with the Gaussian solution Eq. 2.7 of the diffusion equation and the condition specified in Eq. 4.5 in a three-dimensional system [126]:

$$\langle \delta C(\vec{r},t) \cdot \delta C(\vec{r'},t+\tau) \rangle = \frac{\langle C \rangle}{(4\pi D\tau)^{\frac{3}{2}}} \cdot e^{\frac{-|\vec{r}-\vec{r'}|}{4D\tau}} \tag{4.20}$$

The autocorrelation function of the fluorescence fluctuations

$$AC(\tau) = \frac{\langle \delta F(t) \cdot \delta F(t+\tau) \rangle}{\langle F^2 \rangle} = \frac{\int_V \int_{V'} I_{em}(\vec{r}) I_{em}(\vec{r'}) \langle \delta C(\vec{r},t) \delta C(\vec{r'},t+\tau) \rangle dV dV'}{(\langle C \rangle \int_V I_{exc}(\vec{r}) dV)^2} \tag{4.21}$$

then becomes with Equation 4.13 and Equation 4.20:

$$AC(\tau) = \frac{1}{\pi^{3/2} \cdot \omega_0^2 \cdot z_0 \cdot \langle C \rangle} \cdot \frac{1}{1+\frac{\tau}{\tau_d}} \cdot \frac{1}{\sqrt{1+\frac{\tau}{S^2 \tau_d}}}. \tag{4.22}$$

This autocorrelation function gives the decay curve which is expected in a FCS measurement on a single species of fluorescence-labeled molecules dissolved in water; a representative plot is displayed in Figure 4.2. In the autocorrelation function, $V = \pi^{3/2} \cdot \omega_0^2 \cdot z_0$ is the observation volume, with $z_0 = S \cdot \omega_0$ giving the volume's dimension along the octical axis. Thus, $\langle N \rangle = \pi^{3/2} \cdot \omega_0^2 \cdot z_0 \cdot \langle C \rangle$ is the average number of fluorophores in the observation volume, and the amplitude $AC(\tau = 0)$ is the inverse molecule number $\frac{1}{\langle N \rangle}$ in the observation volume. The intensity distribution I_{em} in principle is defined over the entire space and has no physical border, but it decreases exponentially in all three spatial directions due to its Gaussian shape. Therefore, AC describes the behaviour of $\langle N \rangle$ particles in an effective volume V. The size of V is typically about 1 fl, due to Abbe's resolution limit $\omega_0 \approx \frac{\lambda}{2}$. Its exact determination is typically done experimentally, either by remeasuring the already known concentrations of test solutions or by mobility measurements on a molecule species with a known diffusion coefficient.

The mean decay time of the autocorrelation function $\tau_d = \frac{\omega_0^2}{4D}$ is also denoted as the diffusion time since it depends on the diffusion coefficient D. It represents the average residence time of a molecule in the observation volume and hence tells how long a fluororescent molecule is visible on average in the detection volume. The autocorrelation function $AC(\tau)$ can also be regarded after proper normalisation as the probability that a molecule detected at the time $t = 0$ is still detectable at $t = \tau$.

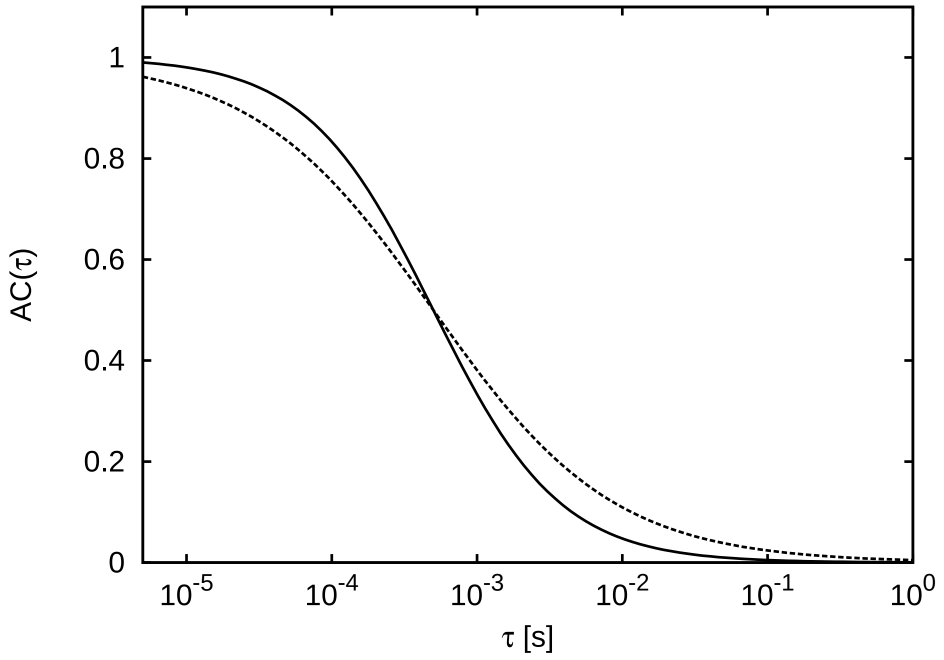

Figure 4.2: Autocorrelation functions of concentration fluctutations in a small observation volume of Gaussian shape due to normal diffusion with $\tau_d = 500\ \mu s$ (Eq. 4.22, full line) and subdiffusion with $\tau_s = 500\ \mu s$, $\alpha = 0.7$ (Eq. 4.26, dashed line).

Autocorrelation function for multiple diffusing particle species

If various fluorescent molecule species with different diffusion coefficients are present in a solution, the autocorrelation function of the system must be modified. We assume that k non-interacting species are present which have the diffusion coefficients D_i and possess all the same fluorescence characteristics $E \cdot Q$. Then, the autocorrelation function AC_{tot} of the entire system is the sum of the single ACs multiplied with a weigthing factor taking in account the relative amount f_i of each species i in the system:

$$AC_{tot} = \sum_{i=1}^{k} f_i \cdot AC_i = \sum_{i=1}^{k} \frac{f_i}{N} \cdot \frac{1}{1+\tau/\tau_{d_i}} \cdot \frac{1}{\sqrt{1+\frac{\tau}{S^2 \tau_{d_i}}}} \tag{4.23}$$

Here, the parameters $\tau_{d_i} = \frac{\omega_0^2}{4D_i}$ are the diffusion times of the k molecule species.

Autocorrelation function for anomalous diffusion

The FCS technique also allows to detect anomalous diffusion of particles. To derive an appropriate fit formula for the autocorrelation function in this context, the specific scaling behaviour of the mean square displacement MSD for anomalous diffusion $MSD \sim 2d\Gamma t^{\alpha}$ (c.f. Section 2.2) typically is modelled using the heuristic approach of a time dependend diffusion coefficient:

$$D(t) = \Gamma \cdot t^{\alpha-1} \tag{4.24}$$

which leads to $MSD \sim 2dD(t)t$. The corresponding diffusion equation is $\frac{\partial C(\vec{r})}{\partial t} = D(t) \cdot \Delta C(\vec{r})$ with the solution:

$$C(\vec{r}) = \frac{1}{(4\pi\Gamma t^{\alpha})^{d/2}} \cdot e^{\frac{-r^2}{4\Gamma t^{\alpha}}} \tag{4.25}$$

where d is the spatial dimension of the system. With the same calculation as in the normal diffusive case, the autocorrelation function for anomalous diffusion becomes:

$$AC(\tau) = \frac{1}{\pi^{3/2} \cdot \omega_0^2 \cdot z_0 \cdot \langle C \rangle} \cdot \frac{1}{1 + (\frac{\tau}{\tau_s})^{\alpha}} \cdot \frac{1}{\sqrt{1 + \frac{1}{S^2}(\frac{\tau}{\tau_s})^{\alpha}}} \tag{4.26}$$

Here, α is the degree of anomaly and τ_s is the average residence time in the confocal volume [44]. Comparative plots of the autocorrelation functions of normal diffusion Eq. 4.22 and subdiffusion Eq. 4.26 are shown in Figure 4.2.

The approach of deriving the autocorrelation function from Equation 4.24 is problematically for small times as $D(t) \to \infty$ for $t \to 0$ if $\alpha < 1$, i.e. in the subdiffusive case. For a mathematically correct treatment of the subdiffusive case, the transition probability $\langle \delta C(\vec{r}, t) \delta C(\vec{r'}, t + \tau) \rangle$ would have to be derived for example in terms of a continuous time random walk (CTRW) [6]. However, in the study [44] it was shown by numerical calculations that fitting FCS data with the handy formula Eq. 4.26 yields effectively the same results as a fit with the rather complex expression calculated in terms of the CTRW.

4.3.3 Disturbing factors and their correction

Triplet states of fluorophores
An FCS measurement is affected by the transition of electrons from the singlet state S_1 to a triplet state T_1 if the transition rates between the states S_0, S_1 and T_1 are smaller than the diffusion times of the observed process, what typically is the case. The effects of the existence of T_1 on a FCS measurement are that
a) the detected fluorophore number in the observation volume is reduced because fluorophores in the triplet state are invisible to the detector and
b) the 'vanishing' of fluorophores due to transition from S_1 to T_1 contributes to the measured fluorescence fluctuations.

Both effects distort the shape of the fluorescence autocorrelation curves measured in FCS. A correction term can be derived by consulting the population kinetics of the S_0, S_1 and T_1 states, which is described by the following system of coupled differential equations [137]:

$$\frac{d}{dt}\begin{pmatrix} S_0(t) \\ S_1(t) \\ T_1(t) \end{pmatrix} = \begin{pmatrix} -k_{12} & k_{21} & k_{31} \\ k_{12} & -k_{21}-k_{23} & 0 \\ 0 & k_{23} & -k_{31} \end{pmatrix} \begin{pmatrix} S_0(t) \\ S_1(t) \\ T_1(t) \end{pmatrix} \tag{4.27}$$

Here, k_{12} is the transition rate from S_0 to S_1, k_{21} from S_1 to S_0, k_{23} from S_1 to T_1, k_{31} from T_1 to S_0.

In the autocorrelation function only molecules contribute which were at $t = 0$ in S_0 and emitted a photon. Solving the Equations 4.27 with the appropriate initial conditions $S_0(0) = 1$, $S_1(0) = 0$, $T_1(0) = 0$ yields that the probability to have a state $X(t)$ populated at the time t is given by an expression of the shape:

$$X(t) = \sum_{i=1}^{3} A_i e^{\lambda_i t}. \tag{4.28}$$

Here, A_i and λ_i are the components of the eigenvectors and eigenvalues of the equation system above. Some illustrative considerations on electron transition (see Reference [137]) yield the eigenvalue λ_3 to be related to the population increase of the triplet state. It can be approximated as

$$\lambda_3 = -k_{31} - \frac{k_{12}k_{23}}{k_{12}+k_{21}}. \tag{4.29}$$

The fraction of fluorophores populating the triplet state can be approximated by the expression

$$f_T = \frac{k_{12}k_{23}}{k_{12}(k_{23}+k_{31}) + k_{31}(k_{21}+k_{23})}. \tag{4.30}$$

We assume now that fluorescence intensity fluctuations contributing to the fluorescence autocorrelation function $AC(\tau)$ are caused either by concentration fluctuations or by molecules that enter or leave the triplet state. This yields that the autocorrelation function $AC(\tau)$ derived in Section 4.3.2 by considering just concentration fluctuations has to be multiplied by the following term to take in account also triplet transitions [137]:

$$F_{triplet}(\tau) = 1 - f_T + f_T e^{-\frac{\tau}{\tau_T}}. \tag{4.31}$$

Here, $\tau_T = 1/\lambda_3$ denotes the triplet relaxation time.

Signal and background

In the detected fluorescence intensity signal $F(t)$, also background light is included. It is generated by reflexions of the laser beam at optical components and by light scattering on impure glass surfaces or the specimen. This background noise is uncorrelated and has therefore no influence on the signal correlations. However, relatively strong noise leads to a apparent increase of the measured fluorophore concentration, since the total recorded fluorescence has increased relatively to the signals that are assigned by autocorrelation to single fluorophores. Therefore, in the case of strong noise a correction of $AC(\tau)$ is necessary by the factor:

$$F_{Background} = (1 - \frac{\langle I_{Background} \rangle}{\langle I_{TotalSignal} \rangle})^2 \tag{4.32}$$

Nevertheless, a powerful and stable laser and interference filters which are optimized to the emission spectrum of the used fluorophores guarantee a fluorescence yield in the detection volume which lies about 3 orders of magnitude over the background. Thus, typically no correction for background light has to be done.

Generally, the fluorescence fluctuations caused by concentration fluctuations must be large enough that they do not vanish in the background noise. The fluorescence fluctuations due to concentration fluctuations are largest when caused by few molecules; therefore the concentration of the molecule species under investigation has to be small in the system (c.f. Section 4.2). The largest fluctuations are measured when the observation volume is smaller than the 'territorial volume' V_t of a single molecule. V_t is defined as $V_t = \frac{1}{\langle C \rangle}$, where $\langle C \rangle$ is the average molecule concentration in the observation volume.

Other disturbing processes

For large objects that are labeled with many fluorophores, rotational motions of the object and inhomogeneous excitation due to size do influence the fluorescence fluctuations detected in the observation volume and thus the FCS measurement. However, this effect can be neglected if only molecules with radii smaller than some ten nanometers are investigated.

Another reason for intensity fluctuations at the detector is the photobleaching of fluorophores. To avoid a fast bleaching, the intensity of the laser illumination is set to a low value during FCS measurements. With an appropriate low laser power, the photochemical average life time of the molecule is much higher than the typical diffusion time of a molecule. Thus, no correction for photobleaching is necessary.

4.4 Determination of a fluid's complex shear modulus

A fundamental mechanical property of any material is its response to shear stress [1]. By examining a material's behaviour under shear deformation we can distinguish the two basically different classes of solid and fluid materials. Solids are elastic and store the deformation energy which is induced by applying a shear strain, whereas fluids are viscous and dissipate the deformation energy. Many materials, however, show both viscous and elastic behaviour: they store a proportion of the deformation energy and dissipate the rest; these materials are called *viscoelastic*. A material class which shows viscoelastic behaviour is, for example, the class of complex fluids, which includes colloidal dispersions, polymer solutions or solutions of self-assembled surfactants.

The viscoelastic behaviour of a material can be quantified by determining its complex shear modulus $G(\omega)$ which measures the stress induced in the material when an oscillatory shear strain of frequency ω is applied. $G(\omega)$ is a complex parameter of the form $G(\omega) = G'(\omega) + iG''(\omega)$. The real part $G'(\omega)$ is the elastic storage modulus which measures the phase response of the medium to an oscillatory strain and thus shows the ratio of the elastic component of the induced stress to the applied strain. The imaginary part $G''(\omega)$ is the viscous loss modulus which measures the out of phase response and thus gives the ratio of the viscous component of the induced stress to the applied strain. Purely viscous media like water with a viscosity η are characterised by $G'(\omega) = 0$ and $G''(\omega) = i\eta\omega$, whereas purely elastic materials like rubber exhibit $G''(\omega) = 0$. In viscoelastic media, both $G'(\omega)$ and $G''(\omega)$ have values significantly larger than zero, with their relative contribution being dependent on the frequency of shearing. In fact, $G(\omega)$ is the fourier transform of the stress relaxation modulus $G_r(t)$ which parametrises the temporal stress relaxation behaviour of a material. Since the single real function $G_r(t)$ determines both real and imaginary part of $G(\omega)$, G' and G'' are not independent but are related by the Kramers-Kronig relations.

The complex shear modulus $G(\omega)$ can be measured either in the bulk of a medium or locally. The local modulus is typically identical to the bulk modulus of small samples and yields information about the small-scale structure of the medium. The bulk modulus of a medium is ususally determined by measuring directly the strengths of a deforming strain applied to the medium and of the induced stress, which can be done, for example, with a strain rheometer or a torsion pendulum. Local moduli can be measured by embedding test particles in a medium and detect either their active behaviour upon manipulation with a field gradient or their passive thermal fluctuations [115].

In the present thesis, measurements of the nanoscale viscoelasticity of cells are presented which were done by determining the mean square displacement *MSD* of

probe particles diffusing within the cells and converting the *MSD* via a mathematical relation to $G(\omega)$. This method was proposed in 1995 by Mason and Weitz [1] as a technique that is, in principle, generally applicable to measure the local complex shear modulus of viscoelastic media.
Following Mason & Weitz [1], the relation of the *MSD* to the complex shear modulus $G(\omega)$ is done under the assumption that the response of a small particle to the thermal stochastic forces leading to Brownian motion is determined by the bulk mechanical susceptibility of the embedding medium (see derivation below). The relation is:

$$\tilde{G}(s) = \frac{s}{6\pi a} \cdot \left(\frac{6k_B T}{s^2 \cdot \widetilde{MSD}(s)} - m \cdot s \right). \tag{4.33}$$

Here, G and the *MSD* are both in the Laplace domain, which is denoted by the tilde. The parameter s is the Laplace frequency, k_B is Boltzmann constant, T denotes the absolute temperature. The first term in brackets describes the dissipation of thermal fluctuations in the medium. The second term is due to inertia and becomes important only at very high frequencies. Neglecting the inertial term, equation 4.33 can be regarded as a generalised, frequency-dependent Einstein-Stokes relation. For a particle diffusing in a purely viscous fluid and having the diffusion coefficient D, $\widetilde{MSD}(s) = \frac{6D}{s^2}$ and the frequency-independent case is recovered: $\eta_0 = \frac{k_b T}{6\pi a D}$.

To determine $\tilde{G}(s)$ of a complex fluid in practice, the *MSD(t)* of probe particles embedded in the fluid is measured. This can, in principle, be done with any method, provided that the measurement does not disturb the rheological properties of the material. The probe particles, however, are required to be spherical and rigid. After having recorded the *MSD(t)*, its Laplace transform to $\widetilde{MSD}(s)$ is performed and $\tilde{G}(s)$ is calculated with equation 4.33. To get $G(\omega)$, one would in principle have to calculate the stress relaxation modulus $G_r(t)$ by taking the inverse unilateral Laplace transform of $\tilde{G}(s)$. A Fourier transform of $G_r(t)$ then would yield $G(\omega)$. Alternatively, $\tilde{G}(s)$ can be fitted with a functional form in the real variable s. $G(\omega)$ is then obtained by using analytic continuation, substituting $i\omega$ for s in the fitted form. The proposed procedure allows to determine a mediums rheological behaviour on different length scales (depending on the probe particles' radii) and over a broad range of excitation frequencies (depending on the time resolution of the *MSD* measurement).
The applicability of this technique was demonstrated in several studies [1, 25, 26]. In Reference [1] the complex shear moduli $G(\omega)$ of various viscoelastic media were determined with two different methods: a) recording the *MSD* of embedded test particles by a scattering light technique and b) by an oscillatory mechanical bulk measurement with a strain rheometer. For the three test cases of a colloidal suspension, a polymer suspension and an emulsion, the results of both measuring techniques agreed very well. Other studies [25, 26] showed that recording the

MSD of test particles in polymer solutions with two different techniques (laser deflection, light scattering) led to the same $G(\omega)$ which again was in agreement with rheometrical bulk measurements.

The described method already was used for various measurements related to biology. Examples include studies on the viscoelasticity of DNA [25], actin solutions [138, 114] and the cytoplasm [11, 27] and the nucleoplasm [113] of living cells.

Derivation of Equation 4.33

To show the relation between a diffusing particle's *MSD* and the embedding medium's $G(\omega)$, we will follow the derivation of Mason & Weitz [1].

The motion of a particle in a viscoelastic medium can be described with a generalized Langevin equation, incorporating a memory function to account for the viscoelasticity [139, 140]:

$$m \cdot \dot{v} = f_R(t) - \int_0^t \zeta(t-\tau) v(\tau) d\tau \tag{4.34}$$

where m is the particle mass and $v(t)$ the particle velocity. $f_R(t)$ represents the random forces acting on the particle, including both the contribution from direct forces between the particles and the stochastic Brownian forces. The integral term represents the viscous damping of the fluid and incorporates a generalized time-dependent memory function $\zeta(t)$.

Since the energy which is stored in the medium leads to changes in the temporal correlations of the stochastic forces acting on the particle at thermal equilibrium, the appropriate fluctuation-dissipation differs from the case of a purely viscous fluid and has the form [139]:

$$< f_R(0) \cdot f_R(t) >= k_B T \zeta(t). \tag{4.35}$$

Here, k_B is Boltzmann's constant and T is the temperature.

The viscoelastic memory function $\zeta(t)$ can be related to the particle's *MSD* by taking the unilateral transform [141] of the generalized Langevin equation Eq. 4.34 and using the fluctuation-dissipation theorem Eq. 4.35.

The assumption is made that $\zeta(t)$ is proportional to the bulk frequency-dependent viscosity η of the fluid:

$$\tilde{\eta}(s) = \frac{\tilde{\zeta}(s)}{6\pi a} \tag{4.36}$$

where s is the Laplace frequency and a the particle radius. For Equation 4.36 to be valid, the used probe particles are required to to have a firm radius a (i.e. they must be spherical and rigid).

Equation 4.36 can be regarded as a generalised, frequency-dependent Stokes law for viscoelastic media, which is a complex function for the particle's resistance to motion. It is based on the assumption that Stokes drag for viscous fluids (no-slip boundaries) can be generalised to viscoelastic fluids at all frequencies s. Since this assumption is not necessarily true, Equation 4.36 is phenomenological. The calculation of the complex shear modulus in the Laplace domain by the formula $\tilde{G}(s) = s \cdot \tilde{\eta}(s)$ yields finally Equation 4.33.

Chapter 5

Results I – Diffusion of nano-particles in living cells and nanorheology of intracellular fluids

In this chapter the results from FCS diffusion measurements are presented in which the intracellular diffusion of fluorescent nanogold particles and, in association, the complex shear moduli of the intracellular fluids were determined; the measuring procedure, the obtained results and their interpretation are described and discussed in detail.

5.1 Problem definition

Although diffusion of proteins and protein-sized test particles in cells has been the subject of several studies, the picture of intracellular diffusion has remained fragmentary in many points. Early measurements with the FRAP method showed a reduction of a macromolecule's diffusion coefficient in living cells compared to water [61]. Recent measurements with the more sophisticated FCS method, however, brought new insights, in that selected proteins (GFP, IgG antibody) and protein-sized dextran molecules were detected to move by subdiffusion [67, 44]. This was ascribed to the dense occupancy of intracellular fluids with macromolecules ('macromolecular crowding') which obstruct the motion of indiviual tracers. Since subdiffusion of molecules can have significant implications on many processes related to biology [73, 74, 76, 83], its detection and quantification for macromolecule in cells is of particular interest. While the occurrence of subdiffusion in itself was convincingly demonstrated [44, 68], the strength of the subdiffusion as specified by the anomaly parameter α is not really clear. The available studies are in this respect problematic either in their choice of the tracers (branched dextran chains and the non-spherical IgG antibody in ref. [44], the GFP fluorophore in ref. [67]) or in their choice of the

experimental environment (crowded model solutions instead of cells in ref. [68]).
The present thesis aims at extending the current understanding of nanoparticle diffusion in living cells. In the experiments which are described in the following section, fluorescent labeled nanogold beads were introduced into living cells as spherical, inert, protein-sized tracers. With FCS their diffusion characteristics both in the cytoplasm and the nucleoplasm were determined. Comparative measurements were done on diffusing BSA proteins. To investigate the cell-specificity of diffusion, various cell lines of different origins and health states were examined.
In further work, the diffusion measurements on nanogold were used to conclude on the rheological state of the cellular interior. Generally, the (sub)diffusive characteristics of particle motion is related to the rheological properties of the embedding environment. Available studies on cell rheology showed entire cells and the intracellular environment to be viscoelastic on the scale of micrometers, mainly due to the stabilising cytoskeleton [11, 102, 108]. In the work presented in the following, however, the rheological properties of intracellular fluids were determined on a lengthscale of some ten nanometers, by transforming the *MSD* of nanogold via a generalised Einstein-Stokes relation into the complex shear modulus $G(\omega)$ that quantifies the viscoelastic behaviour of an embedding medium. Since the mechanical behaviour of cells on the nanoscale can expected to be determined mainly by macromolecular crowding, the determination of $G(\omega)$ gives a description of the crowding state in terms of rheology. In particular, the measurements highlight if macromolecular crowding contributes to the over-all cell stability. To gain further insights into the crowing state of intracellular fluids, a change of crowding was induced by stressing cells osmotically and determining again the complex shear modulus.

5.2 Materials and Methods

Nanogold particles

Colloidal nanogold particles (Molecular Probes, Eugene, OR) are spherical, have a diameter of 5 nm and are labeled with the fluorophore dye Alexa 488. The dyes are linked covalently to the gold via conjugation and streptavidin-biotin binding. The nanogold was kept in a specific buffer based on Tris, with physiological pH = 7.4 and a 0.1 mass% extra content of BSA. Potentially unoccupied streptadin binding sites were saturated by incubating the nanogold with biotin.
For our purpose, the nanogold particles were appropriate because the particles are supposed to be spherical and to not to bind or stick nonspecificly to components of the cellular interior. The latter is avoided by saturating the goldbeads in BSA, which covers potential sites of nonspecific interactions of the gold surface with proteins.

BSA

In comparative diffusion measurements, the protein bovine serum albumin (BSA)

(Molecular Probes) labeled with the fluorophore Alexa 488 was used as a probe particle with well-defined molecular weight of about 66000 daltons.

Fluorophores

The fluorophore Alexa 488 which labeled in the diffusion measurements presented here nanogold and BSA has an absorption maximum at a wavelength of 488 nm and an emission maximum at 530 nm (see Figure 5.1).

For marking microinjected cells, TexasRed labeled dextran (10,000 mol wt; Molecular Probes) was used. The TexasRed fluorophore has an absorption maximum at a wavelength of 596 nm and an emission maximum at 615 nm (see Figure 5.2).

In comparative experiments the diffusion of the eGFP (enhanced green fluorescent protein) fluorophore in HeLa cells was measured with FCS. For this purpose, eGFP was expressed from a pEGFP plasmid vector (Clontech) which was transfected using the reagent Fugene 6 (Roche). The eGFP fluorophore has an absorption maximum at a wavelength of 489 nm and an emission maximum at 507 nm (spectra not shown).

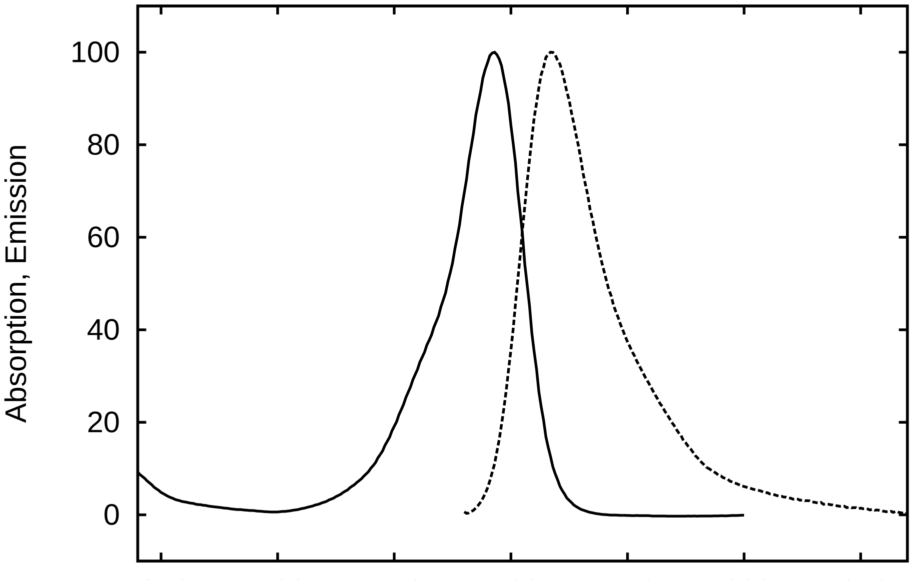

Figure 5.1: Spectra of absorption (full line) and emission (dashed line) of Alexa 488.

Cells

Wild-type HeLa, HepG2, U2OS, PLC and NIH-3T3 cells were grown at 37^{o}C in DMEM medium (+10% fetal calf serum, +1% penicillin-streptomycin). BXPC and CHO cells were grown at 37^{o}C in RPMI medium (+10% fetal calf serum, +1%

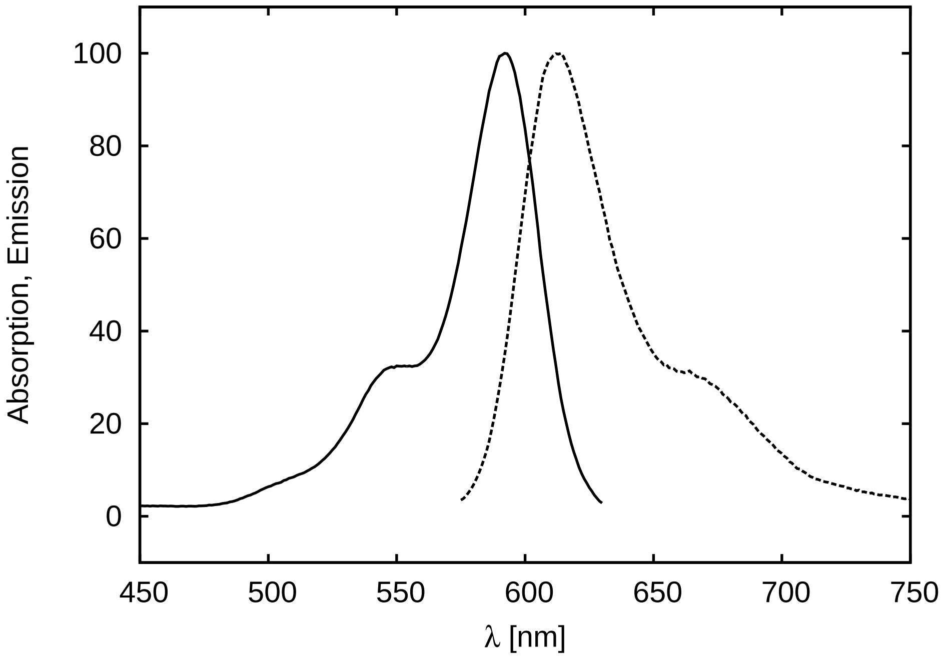

Figure 5.2: Spectra of absorption (full line) and emission (dashed line) of the fluorophore TexasRed.

penicillin-streptomycin). TP366 and TP98G cells were grown at 37^{o}C in MEM medium (+10% fetal calf serum, +1% penicillin-streptomycin). THLE cells were grown at 37^{o}C in bronchial epithelial cell basal medium (Clonetics, San Diego, CA).

Xenopus egg cell extract

Extract from egg cells of *Xenopus laevis* was kindly provided by T. Surrey (EMBL Heidelberg, Heidelberg, Germany). The protein concentration of the extract was determined using the Bradford method [142] to be c = 12.8 mg/ml, which is in agreement with previous reports [143].

Microinjection

Microinjection of Nanogold in cells was done with an AIS2 microinjection system (Cellbiology Trading, Hamburg, Germany) based on an Eppendorf Femtojet injection system. Injection tips were pulled with a P97 tip puller (Sutter Instruments, Novato, CA) from borosilicate thin-wall capillaries with filament (length, 100 mm; OD, 1.2 mm; ID, 0.94 mm).

Microscopy
FCS measurements were performed with a Leica SP2-TCS confocal-laser scanning microscope equipped with a water immersion objective (HCX PL APO 63 x 1.2W CORR) and an FCS unit (both, Leica Microsystems, Mannheim, Germany). Samples were illuminated with a 488-nm Ar laser, the fluorescence was detected using a bandpass $500 - 530$ nm and a pinhole size of 1 Airy unit. The sample and the microscope were held at 37°C by a climate chamber (Life Imaging Services, Reinach, Switzerland).

5.3 Experimental procedure

Introduction of nanogold into cells

Cells were splitted onto non-coated glass cover slips one to five days before the FCS measurement, depending on the growth rate of the individual cell line. At the day of the experiment cells covered about 10 - 50 % of the glass cover slips' area.

Nanogold beads were introduced into the cells via microinjection 2 - 3 hours before the FCS measurement. Microinjection is a technique that is used to insert fluid substances into living cells. The fluid substance is filled into a glas needle with a fine diameter of 500 nm at the top. Having the cells adherent to glass cover slips, the needle penetrates the plasma membrane and the fluid is injected by applying a pressure of about 30 to 200 hPa at the back of the needle. The process of microinjection is performed under a special microscope setup equiped with a micromanipulator. The needle is moved with a step motor, allowing precise positioning within accuracy of about 500 nm. The exact injection pressure is chosen individually for every cell line, to ensure the injection process to be as gentle as possible for the cells.

The dissolved fluorescent labeled nanogold was injected into the cells in amounts that resulted in a nanomolar concentration of gold in the cell (detected with FCS), which is appropriate for FCS measurements. The microinjected fluid dispersed over the whole cellular interior within seconds.

Fluorophore concentrations of some nanomoles are optimal for FCS measurements, but can not be visualised in microscope pictures. Thus, a fluorescent marker had to be co-injected to be able to recognize the cells in which nanogold was present. As marker the fluorophore Texas Red was used, which is not excited at the wavelength of 488 nm used for the FCS measurements (c.f. the spectrum of TexasRed in Figure 5.2). Light at the emission wavelengths of TexasRed also was prevented by a bandpass filter $500 - 530$ nm from arriving at the detector. Thus, the Texas Red marker did not disturb the FCS measurements.

FCS measurements

The FCS measurements in cells were performed at a temperature of 37^oC. During a FCS measurement, the cells were kept in transparent imaging medium, which lacked the pH indicator dye Phenol Red that is commonly present in growing media.

Before each FCS measurement a differential interference contrast (DIC) image of the cell under investigation was recorded. Representative images of 3 cell types are shown in the Figures 5.4, 5.5, 5.6. In the cell images, cytoplasm and nucleus could be clearly distinguished. For a FCS measurement the laser spot was placed at the locus of interest in the cytoplasm or in the nucleus. As locus of interest an arbitrary position was chosen which allowed the observation of free nanogold diffusion in three dimensions. To this end, some distance was kept between the laser spot and the plasma membrane, the nuclear envelope and other membrane structures (as far as identifiable in the cell image) which could have restricted the nanogold diffusion.
The spot was illuminated with laser light of the wavelength 488 nm. The laser power was set to values between 10 to 100 mW. This yielded a fluorescence intensity signal of typically 8000 to 20000 cps (photon counts per seconds) at the detector.

For each individual cell that was inspected with FCS, two measurements in the cytoplasm and two measurements in the nucleus were performed. For the measurement in one point, the fluorescence intensity was recorded for 50 s.
Typically, FCS experiments were performed in 12 to 15 individuals from each cell line. In the case of Hela cells, 35 untreated individuals and 34 indiviuals incubated in hyperosmotic medium were tested, in order to monitor the distribution of the τ_s and α values.

The calculation of the autocorrelation curve from the recorded fluorescence signal was done by the microscope's software (Leica Microsystems, Mannheim, Germany). The autocorrelation analysis resulted in the characteristic decay curve that describes the diffusion of fluorescent molecules in solution (see Figures 5.4, 5.5, 5.6 for representative curves).

The fluorescence intensity signals recorded from different points in an individual cell were of similar strength, both for the cytoplasm and for the nucleus. Autocorrelating the recorded fluorescence series yielded good correlation curves both for the cytoplasm and the nucleus. The fitting of the curves showed similar nanogold concentrations in both compartments. The conclusion from these observations is that nanogold particles were distributed equally in the cells. This is in agreement with the expectation that molecules with diameters smaller ≈ 9 nm (like the nanogold particles) can diffuse freely into and out of the nucleus [34].

FCS measurements on 'empty' cells in which no nanogold had been injected, yielded only low fluorescence signals of 500 to 2000 cps and autocorrelation curves that were fluctuating about the zero line without showing a characteristic decay. This observation made sure that the high fluorescence signal and the characteristic autocorrelation curve measured in cells containing labeled nanogold was indeed due to the diffusing nanogold and was not caused by autofluorescence of the cells.

Analysis of FCS curves

The recorded FCS curves were fitted using XMGRACE, a free software program for processing and plotting data (see *http://plasma-gate.weizmann.ac.il/Grace/*). As fit function for a potentially subdiffusive process, typically the product of Equations 4.26 and 4.31 is used [144, 44, 68]. Equation 4.26 is the theoretical expression for an autocorrelation function of fluorescence fluctuations arising due to fluorophore (sub-)diffusion in a small observation volume of Gaussian shape, while Equation 4.31 represents a correction term to account for the fluorophore photophysics (i.e. electron transitions into nonfluorescent triplet states).
Since subdiffusion is generically a transient phenomenon that turns to normal diffusion beyond a certain time scale (c.f. Section 2.2.2), both subdiffusion and normal diffusion might contribute to the autocorrelation curve. Thus, in the present work the formula Eq. 4.26 was modified by replacing the term $(\frac{\tau}{\tau_s})^\alpha$ with the empirical expression $\frac{\tau}{\tau_d} + (\frac{\tau}{\tau_s})^\alpha$. The resulting fit formula is:

$$AC(\tau) = \frac{1 - f_T + f_T e^{\frac{\tau}{\tau_T}}}{< N >} \cdot \frac{1}{1 + \frac{\tau}{\tau_d} + (\frac{\tau}{\tau_s})^\alpha} \cdot \frac{1}{\sqrt{1 + \frac{\tau}{S^2 \tau_d} + \frac{1}{S^2}(\frac{\tau}{\tau_s})^\alpha}} \tag{5.1}$$

Here, ω_0 is the lateral diameter of the observation volume. The shape factor S gives the distortion of the observation volume in axial direction, f_T is the fraction of fluorophores in the triplet state, τ_T is the triplet relaxation time (c.f. Section 4.3.2).

The fit of a FCS curve with Equation 5.1 reveals three parameters that characterise the diffusion of the fluorescing particles:
a) the characteristic time τ_d of the transition to normal diffusion (typically $\tau_d \gg$ 10 ms).
b) the characteristic particle spreading time τ_s below the transition to normal diffusion, i.e. in the subdiffusive regime. τ_s is the mean residence time of a fluorophore in the confocal volume, determining the decay time of the autocorrelation curve, and has typically values $\tau_s \ll 10$ ms.
c) the anomaly α. The deviation of α from unity (normal diffusion) specifies the degree of anomaly of the measured diffusion process which can be subdiffusion ($0 < \alpha < 1$) or superdiffusion ($\alpha > 1$). α determines the shape of the decay of the autocorrelation curve.

With these three parameters, the mean square displacement $\mathit{MSD}(\tau)$ of the measured diffusion can be calculated as

$$\mathit{MSD}(\tau) = \omega_0^2 \frac{\tau}{\tau_d} + \omega_0^2 (\frac{\tau}{\tau_s})^\alpha \tag{5.2}$$

$\mathit{MSD}(\tau)$ is a measure for the spatial spreading of particles during a certain time period τ.

In the measurements, the average τ_s and α values of a cell line for 1) the cytoplasm and 2) the nucleus were calculated as the arithmetic means of the cytoplasmic/nucleoplasmic τ_s and α values of all measured individual cells.

Calculation of complex shear modulus

From the *MSD* of the nanogold particles as determined from the FCS measurements with equation 5.1, the complex shear modulus $G(\omega)$ of cytoplasm and nucleoplasm was calculated, following the strategy of Mason & Weitz [1] (c.f. Section 4.4). The 5 nm nanogold beads were rigid and spherical, and thus satisfied the requirement of Mason & Weitz [1].

To calculate $G(\omega)$, first a Laplace transform of the *MSD* was done:

$$\widetilde{\mathit{MSD}}(s) = \int_0^\infty \mathit{MSD}(\tau) e^{-s\tau} d\tau \tag{5.3}$$

which led for the *MSD* as specified in Equation 5.2 to

$$\widetilde{\mathit{MSD}}(s) = \frac{\omega_0^2}{\tau_d s^2} + \frac{\omega_0^2 \alpha!}{\tau_s^\alpha s^{\alpha+1}} \tag{5.4}$$

Setting this in equation 4.33 and neglecting the inertia term $-m \cdot s$, resulted in $\tilde{G}(s)$, the complex shear modulus in the Laplace space:

$$\tilde{G}(s) = \frac{k_B T}{\pi R \omega_0^2} \frac{s}{\frac{1}{\tau_d} + \alpha! \frac{s^{1-\alpha}}{\tau_s^\alpha}} \tag{5.5}$$

Substituting s with $i\omega$ yielded:

$$G(\omega) = \frac{k_B T}{\pi R \omega_0^2} \cdot \frac{\frac{\alpha!}{\tau_s^\alpha} \omega^{2-\alpha} \sin(\phi) + i(\frac{\omega}{\tau_d} + \frac{\alpha!}{\tau_s^\alpha} \omega^{2-\alpha} \cos(\phi))}{\frac{1}{\tau_d^2} + \frac{2\alpha!}{\tau_d \tau_s^\alpha} \omega^{1-\alpha} cos(\phi) + \frac{\alpha!^2}{\tau_s^{2\alpha}} \omega^{2-2\alpha}} \tag{5.6}$$

where $\phi = \frac{\pi}{2} - \frac{\pi}{2}\alpha$. For the conversion, $i^\alpha = e^{\frac{i\pi}{2\alpha}}$ was used. $\alpha!$ was calculated via $\alpha! = \Gamma(\alpha + 1)$, with the gamma function $\Gamma(x)$ being defined as

$$\Gamma(x) = \frac{e^{-cx}}{x} \cdot \prod_{k=1}^{\infty} (1 + \frac{x}{k})^{-1} e^{x/k}. \tag{5.7}$$

In the limit $\tau_d \rightarrow \infty$, the complex shear modulus Eq. 5.6 shows an asymptotic scaling

$$|G(\omega)| \sim (\tau_s \omega)^{\alpha} \tag{5.8}$$

Using FCS, diffusion on a timescale from 10^{-6} s to 1 s was investigated. With $\omega = \frac{1}{\tau}$, the complex shear modulus $G(\omega)$ as calculated from FCS data hence covered frequencies ω from 1 Hz to 10^6 Hz.

The question may arise whether the Laplace transformation as described by Equation 5.3 (defined from $\tau = 0$ to ∞) is allowed for a parameter like $MSD(\tau)$ that is only known within a limited range of τ. To examine if the unknown course of the $MSD(\tau)$ outside the experimentally determined τ-domain might influence $G(\omega)$ as calculated via the Laplace transformation, exponential deviations were artificially introduced at the beginning and the end of $MSD(\tau)$. In the resulting $G(\omega)$, changes were observed hardly more than half an order of magnitude away from the boundaries of the corresponding frequency range. This result shows that the extraction of the $G(\omega)$ via the Laplace transformation is a rather robust approach.

Stressing cells osmotically by incubation in hypertonic medium

For some of the FCS measurements, cells were stressed osmotically by incubating them in hypertonic medium. The term osmosis denotes the net flux of solvent across a semi-permeable membrane (permeable to solvent, impermeable to solute molecules) from a solution with lower solute concentration to a solution with higher solute concentration. The movement of solvent here happens without any input of energy, but is entropy-driven. This physical effect can be used to extract water from cells, which is the solvent of the molecules in cytoplasm and nucleoplasm. If cells are put into growing media which have a higher solute concentration (hypertonic) than the cellular interior, water is forced to leave the cells to reduce the difference in concentration due to osmotic pressure.

In the experiments presented here, the medium was made hypertonic by adding one of the osmotic stress agents sucrose, raffinose, NaCl and urea.

The osmotic stress agent sucrose (or saccharose) is a di-saccharid, i.e. a molceule that consists from two sugars. Due to its size, it can not enter living cells [145]. Therefore, effects observed upon addition of high sucrose concentrations to the growing medium must be ascribed to the cell's osmotic loss of water, whereas chemical or biological reactions due to an over-saturation of the cell with sucrose can be excluded. Raffinose on the other hand is a tri-saccharid and is also too large to enter cells. NaCl is twice as osmolar as the other agents, because it dissociates into a positive and a negative ion. Stressing cells osmotically with addition of NaCl to the medium may cause both effects of a) water detraction from the cell and b) the entering of Na^+ and Cl^- into the cell, because these ions are rather small. The cell's loss of water may therefore be weaker than under osmotic stressing with sucrose or raffinose. Urea molecules are comparable in size to water molecules and may thus enter cells.

Cells may react to osmotic stress by enabling a volume regulation. This potentially happens by changing their ion flux across membrane channels and in producing osmolytes (i.e. molecules which affect osmosis) [146]. However, these volume control regulations do not start during the first 2.5 hours after hypertonic incubation [147]. In the present experiments, the FCS measurements were performed about 30 min after having put the cells in hypertonic media, and a FCS measurement session lasted about 1h. Thus, the FCS measurements should not have detected effects due to cell internal volume compensation reactions.

To examine if cells survive the treatment with osmotic stress agents, we replaced in a test experiment the hypertonic growing medium (500mM sucrose) after 1.5 hours with normal growing medium. Cells were afterwards normally cultured in the incubator and observed for one week. They showed normal growing and division behaviour.

Determining the ratio of the cell size to the nucleus size

To estimate the tumor aggressivity of the different cell lines, the area ratio of entire cells with respect to their nucleus area was determined. For this purpose transmission light pictures of cross sections of about 25 individuals of each cell line were recorded. On the cell images nucleus and cytoplasm could be clearly distinguished. The area sizes of the entire cell and of the cell nucleus on the images were quantified with the 'area measurement' tool of the Leica Confocal Software. All included cells were selected under the restriction to have one clearly recognizable nucleus, i.e. to not be within a division process.

FCS calibration measurement

As a calibration measurement the diffusion of labeled gold beads in water was determined with FCS (see Figure 5.3 for a representative measurement curve). The gold beads were detected to show the characteristics of normal diffusion, with a diffusion time $\tau_s = 125\ \mu s$. The result of normal diffusion is in agreement with the expectations for the motion of spherical particles in diluted solution, which assures that the confocal microscope is properly aligned, i.e. that the confocal volume has the correct shape and does not suffer from distortions. Perturbations of the confocal

volume falsifying the measurements could lead e.g. to the detection of a wrong anomaly α with FCS [148, 149].
The width of the confocal volume was determined to be about $\omega_0 = 210$ nm by comparing the measured diffusion coefficient $D = \frac{\omega_0^2}{4\tau_s}$ with the theoretically expected D of nanogold in water which was calculated from the Einstein-Stokes-relation as $D = 90\ \mu m^2/s$. The detected ω_0 is also in fair agreement with the microscope's resolution limit at $\lambda = 488$ nm which can be estimated to be ≈ 244 nm according to Abbe's formula $\omega_0 \approx \frac{\lambda}{2}$.

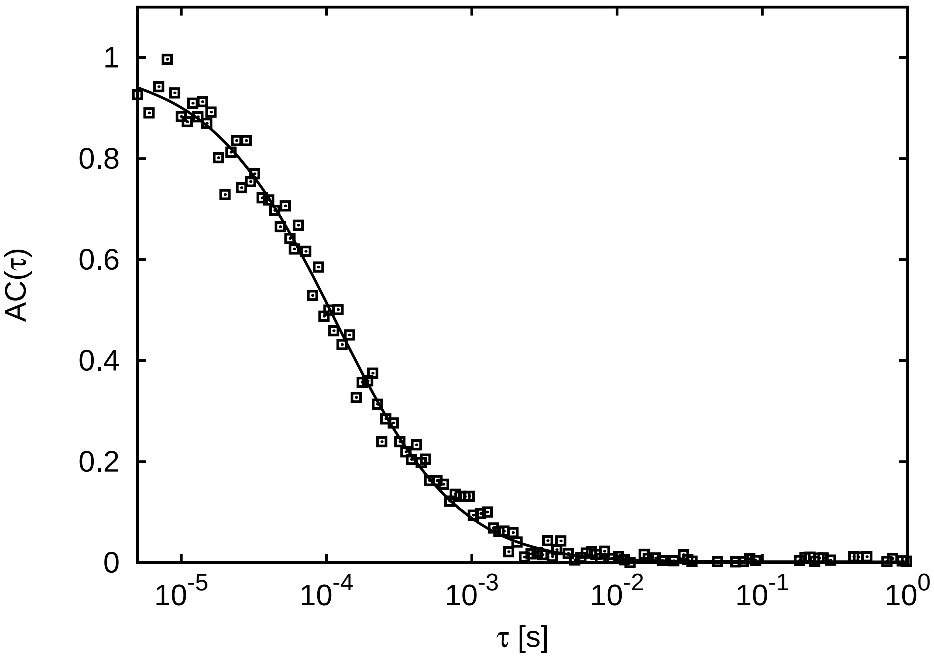

Figure 5.3: FCS measurement of 5 nm gold beads in water (symbols). Fitting with Equation 5.1 yields normal diffusion with $\tau_s = 125\ \mu s$ (full line).

5.4 Results

5.4.1 Diffusion of nanogold in cells

To examine the diffusive behaviour of nanosized particles in living cells, fluorescently tagged nanogold beads (diameter 5nm) were introduced via microinjection into individuals of different mammalian cell types. As a representative collection of cells the 10 well-established cell lines NIH-3T3, CHO, Thle-3, HepG2, PLC, HeLa, BXPC, TP98G, TP366 and U2OS were examined. These cell lines cover a broad range of origins: they are derived from different mammalian species (hamster, mouse and human), from different tissues (liver, brain, cervix, ovaries, muscles, bone) and are of different health state (originally healthy but immortalized cells and different cancer cell species) (see Table 5.1).

The nanogold diffusion in the cytoplasm and the nucleus of the cells was measured using fluorescence correlation spectroscopy (FCS). Representative DIC images and FCS curves of 3 cell lines can be seen in the Figures 5.4, 5.5, 5.6. In all cell lines, the nanogold particles were detected to show the characteristics of strong subdiffusion, both in the cytoplasm and the nucleoplasm. The values of the average residence times τ_s in the confocal volume varied between 100 and 900 μs in the different cell lines. Thus, compared to nanogold diffusion in water ($\tau_s = 125\ \mu s$), τ_s was typically increased in cells by factors from 2 to 7, with exception of PLC cells which showed residence times similar to water. The average anomaly degrees α were between 0.48 and 0.63 (see Table 5.1). For times $\tau_d > 0.85$ ms, normal diffusion was recovered. The latter observation is consistent with previous proposals that subdiffusion due to obstruction/crowding should be rather a transient than an asymptotic phenomenon [44, 52, 150]. The triplet times τ_T typically were about $\tau_T \approx 1$ to 10 μs which is consistent with the current knowledge about the Alexa 488 dye.

For experiments in Hela cytoplasm the distributions of measured τ_s and α values were monitored. The residence times τ_s displayed an exponential to uniform distribution, while α was Gaussian distributed around a mean value of 0.51 with a standard deviation of 0.07 (see Figure 5.13).

The parameters τ_d, τ_s and α determine the mean square displacement *MSD* of the diffusing particles. Logarithmic plots of the average *MSD*s of nanogold in the cytoplasm and the nucleoplasm of HeLa cells are shown in Figure 5.7. The scaling with an exponent $\alpha < 1$, characteristic for subdiffusion, is clearly visible.

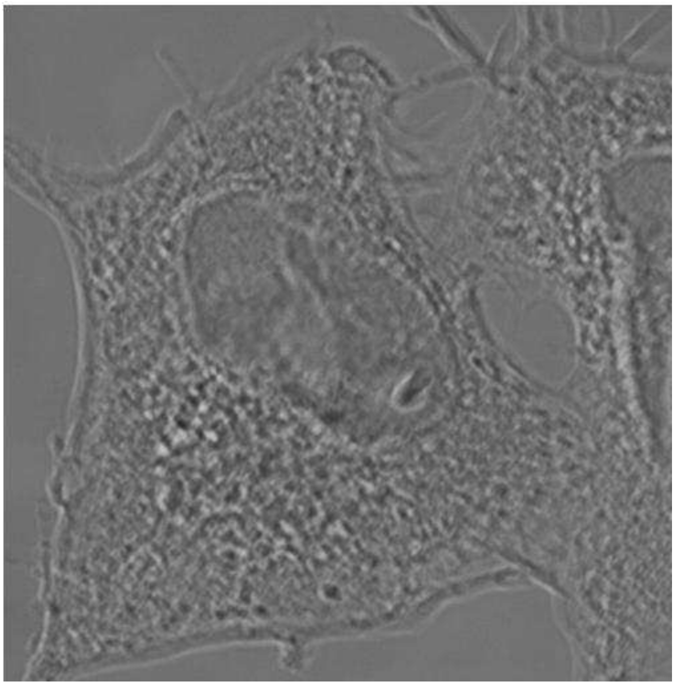

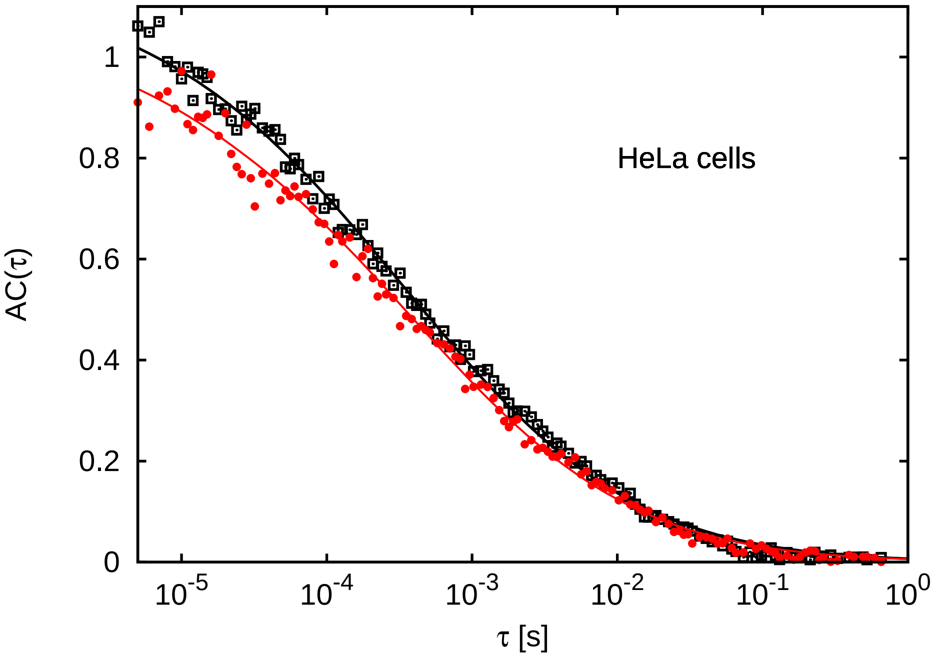

Figure 5.4: DIC image of a HeLa cell; representative FCS curves of 5 nm gold beads diffusing in the cytoplasm (black squares) and the nucleus (red dots). Fitting with Equation 5.1 yields subdiffusion (full lines) with $\alpha = 0.51$ (cytoplasm) and $\alpha = 0.56$ (nucleus).

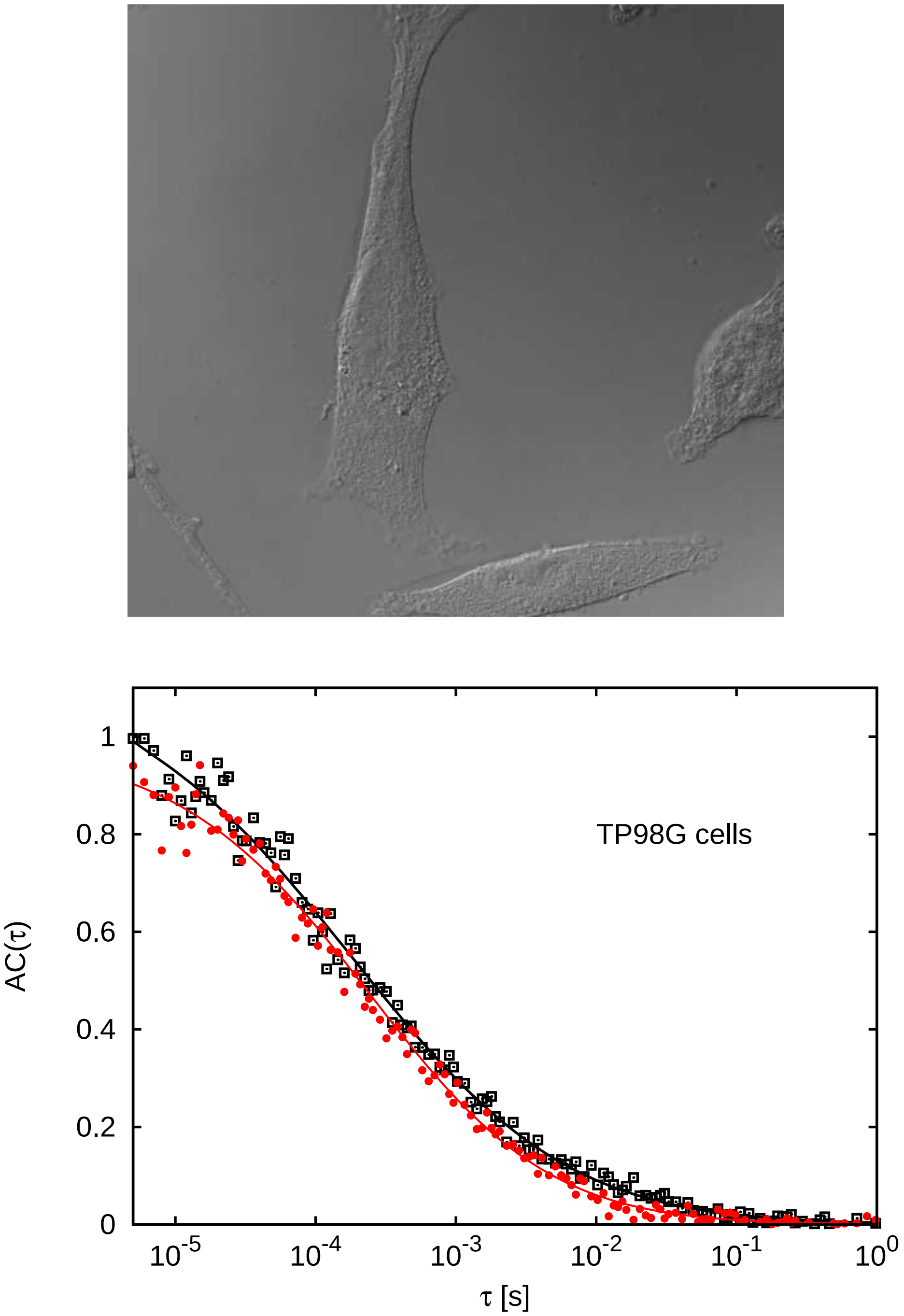

Figure 5.5: DIC image of a TP98G cell; representative FCS curves of 5 nm gold beads diffusing in the cytoplasm (black squares) and the nucleus (red dots). Fitting with Equation 5.1 yields subdiffusion (full lines) with $\alpha = 0.56$ (cytoplasm) and $\alpha = 0.63$ (nucleus).

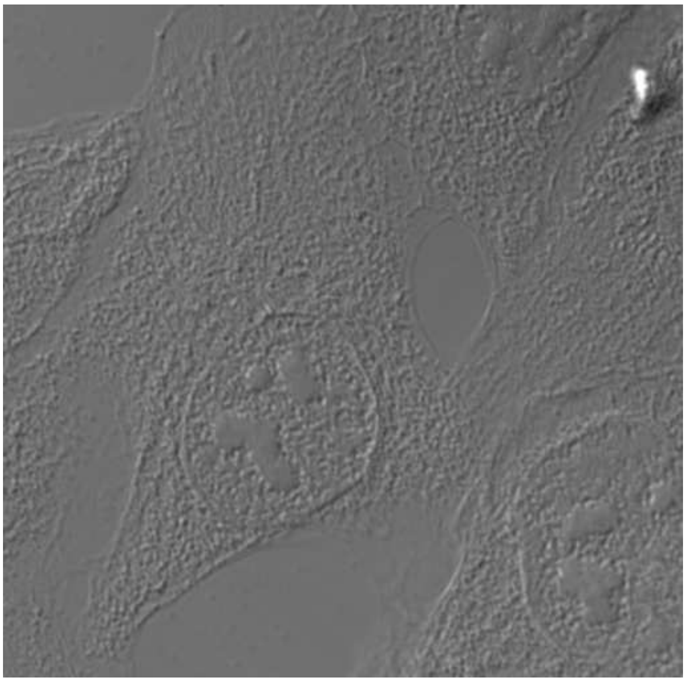

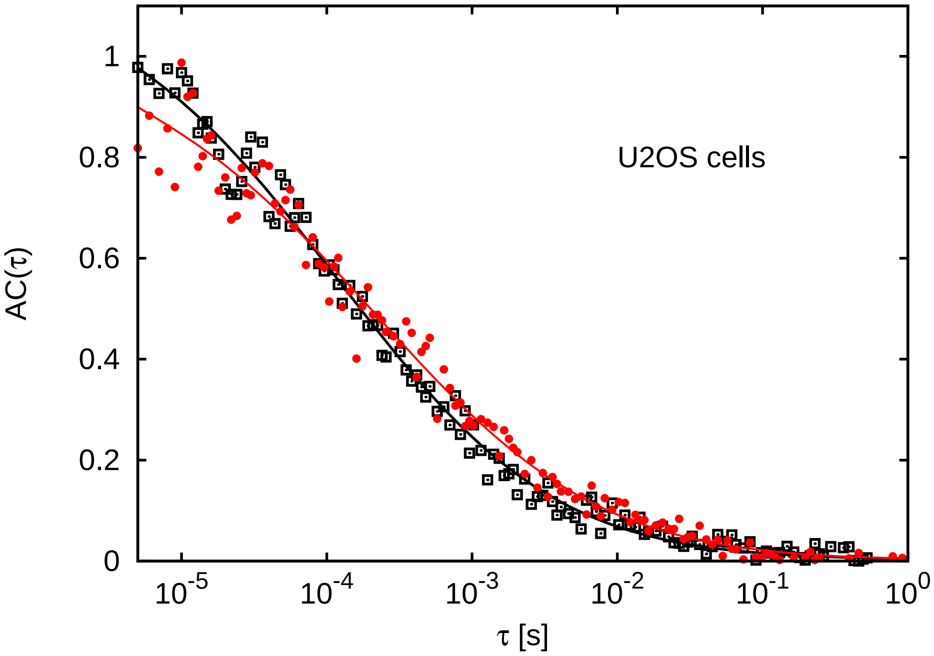

Figure 5.6: DIC image of a U2OS cell; representative FCS curves of 5 nm gold beads diffusing in the cytoplasm (black squares) and the nucleus (red dots). Fitting with Equation 5.1 yields subdiffusion (full lines) with $\alpha = 0.53$ (cytoplasm) and $\alpha = 0.62$ (nucleus).

Cell line	**Cytoplasm**		**Nucleus**	
	τ_s [μs]	α	τ_s [μs]	α
HeLa (human cervix cancer)	270	0.51	160	0.56
BXPC (human adenocarcinoma)	590	0.52	260	0.56
TP366 (human glioblastoma)	250	0.55	165	0.55
TP98G (human glioblastoma)	309	0.56	275	0.63
U2OS (human osteosarcoma)	260	0.53	240	0.62
PLC (human hepatoma)	130	0.52	98	0.62
HepG2 (human hepatoma)	780	0.52	500	0.58
Thle (human liver)	330	0.48	270	0.53
3T3 (mouse fibroblasts)	544	0.59	915	0.60
CHO (chinese hamster ovary)	646	0.52	895	0.54

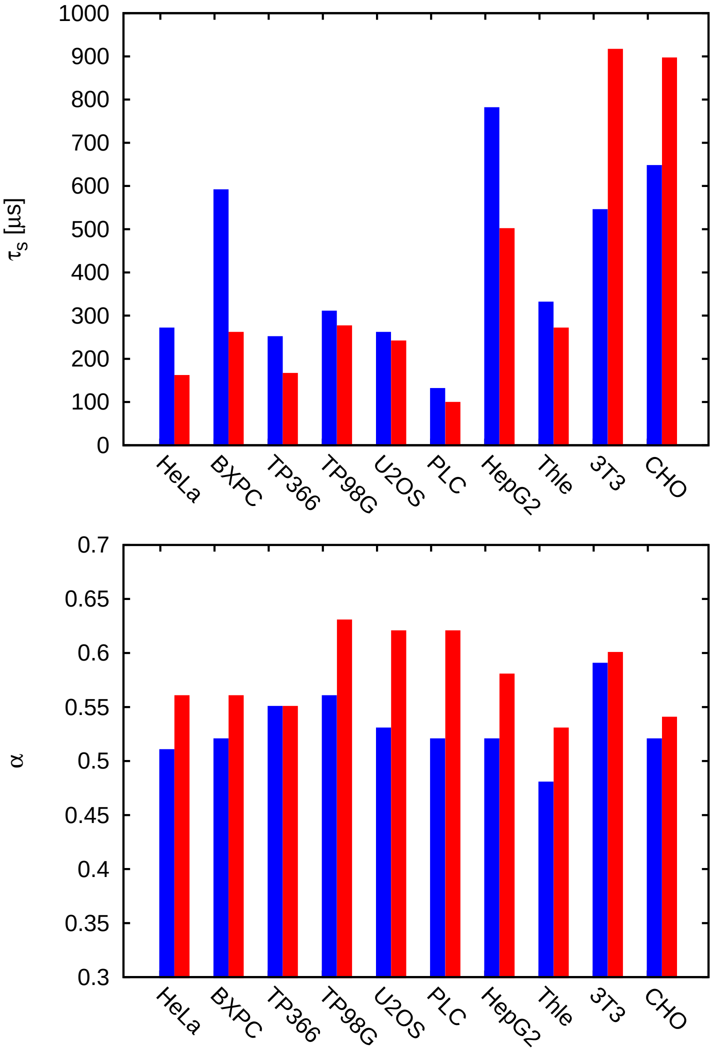

Table 5.1: Table: Average mean residence times τ_s and diffusion anomaly degrees α of 5 nm gold beads in the cytoplasm (blue, left columns) and the nucleus (red, right columns) of 10 different cell lines.

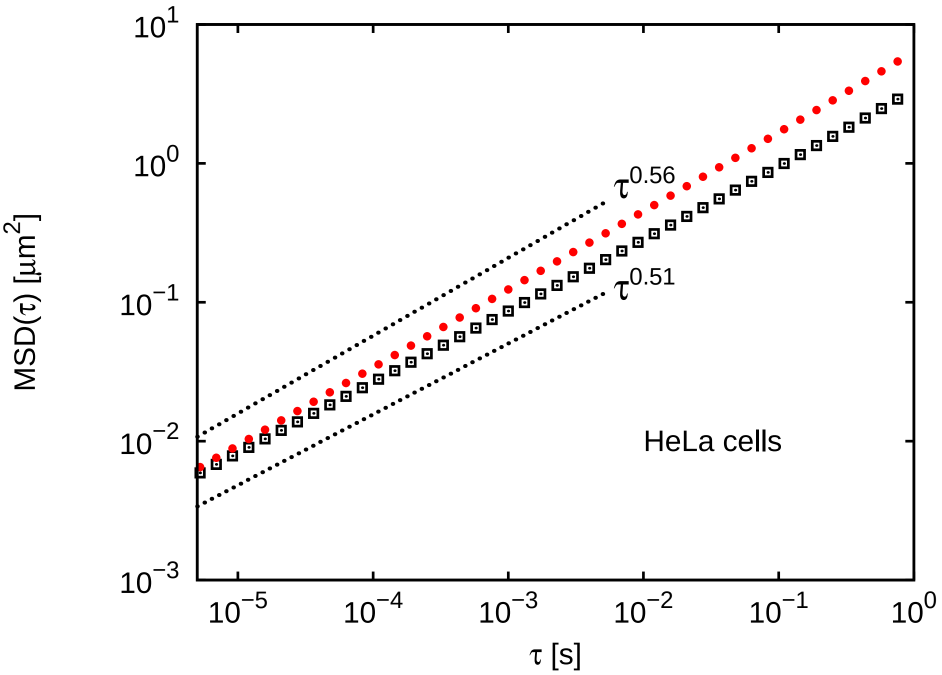

Figure 5.7: Average mean square displacements of 5 nm gold beads in the cytoplasm (black squares) and the nucleoplasm (red dots) of HeLa cells, calculated from FCS data.

Subdiffusion occurs due to obstruction of tracers by macromolecular crowding

The result that nanogold particles move by subdiffusion in cells is in accordance with previous intracellular diffusion measurements on proteins and dextrans [67, 44]. As shown in Reference [44], the most probable reason for subdiffusion of nanoparticles in cells is the obstruction of tracers by macromolecular crowding, i.e. by macromolecules like proteins or RNA molecules which are dissolved in the intracellular fluids. Due to crowding the cytoplasm and the nucleoplasm appear to nanosized tracers as a maze-like environment of fractal geometry on small length scales which leads – as shown in percolation theory – to a slowdown of tracer diffusion on the associated time scales and therefore to subdiffusion (c.f. Section 2.2.2).

Some other parameters which possibly affect nanoparticle diffusion in cells may be discussed in the following. The authors of Reference [53] suggest an influence of the cytoskeletal actin network on diffusion. However, the cytoskeleton should not play a role for nanoparticle subdiffusion since Reference [44] showed that the degree α of subdiffusion for dextran tracers did not change upon depolymerization of cytoskeletal components. In principle, also transient binding of particles can cause subdiffusion, but is here excluded since nanogold particles are inert due to their coating with BSA. Generally, subdiffusion due to binding only appears either in infinite hierarchies of traps or in systems which are not in equilibrium, the latter meaning that the binding process would have to be actively turned on and off by the cell [21, 22]. We can assume that in cells neither an infinite trap hierarchy nor an active binding mechanism for an unspecific object like nanogold exists.

The anomaly degree α as a measure for a fluid's crowding state

According to percolation theory the anomaly degree α of a particle diffusing in an obstructed environment decreases with an increasing obstacle concentration (i.e. subdiffusion becomes stronger). The lowest α-value that can be caused by obstruction in a three-dimensional environment is $\alpha_P = 0.526$, which is reached for high obstacle concentrations C at the critical percolation threshold C_P (c.f. section 2.2.2).

In the present work, typical values of $\alpha \approx 0.55$ were measured for nanogold subdiffusion in cells, which is very close to α_P. Thus, the crowded intracellular fluid seems to appear as an environment of very high obstacle concentration to the nanogold beads. The authors of the study [44] in a similar context suggested α to be a measure for the crowding degree of a fluid, in the meaning that the degree of crowding is high when probe particles show small α values. The degree of crowding of a fluid, however, is a more qualitative than quantitative measure. It is influenced by several parameters, e.g. the individual concentrations of different crowder molecule species present in a fluid, but also by their geometrical shapes, sizes and modes of interaction. When crowding is probed by measuring the diffusion of a tracer particle also the properties of this tracer will be reflected in the observed α since an environment will appear differently to tracers of different sizes and shapes.

To do now a qualitative classification of the crowding degree of the cytoplasm and the nucleoplasm on base of the performed FCS mesurements, the anomaly degrees α of nanogold diffusion in cells were compared with α values of nanogold in crowded test fluids, whose concentrations of crowder molecules could be varied by dilution.

The first series of test measurements was done in solutions of unlabeled dextran molecules (molecular weight: 60 - 90 kDa) in PBS buffer (an aqueous solution with physiological pH = 7.4). Dextrans are inert hydrophilic electroneutral, highly branched polymers of glucose; concentrated solutions of these molecules represent crowded environments causing subdiffusion of nanosized tracers [44, 68].

The test measurements were performed in dextran solutions with dextran concentrations between 30 and 360 g/l. At 360 g/l, a dextran solution is close to the saturation limit. With FCS, nanogold beads were observed to show subdiffusion at all concentrations, with anomaly degrees α that decreased with increasing dextran concentrations from 0.89 to 0.72 (see Figure 5.8 for representative FCS curves and a table with the measured values). The measured residence times τ_s increased with increasing dextran concentration from $\tau_s = 150\ \mu s$ to $\tau_s = 2000\ \mu s$. These findings are in agreement with earlier studies [44, 68].

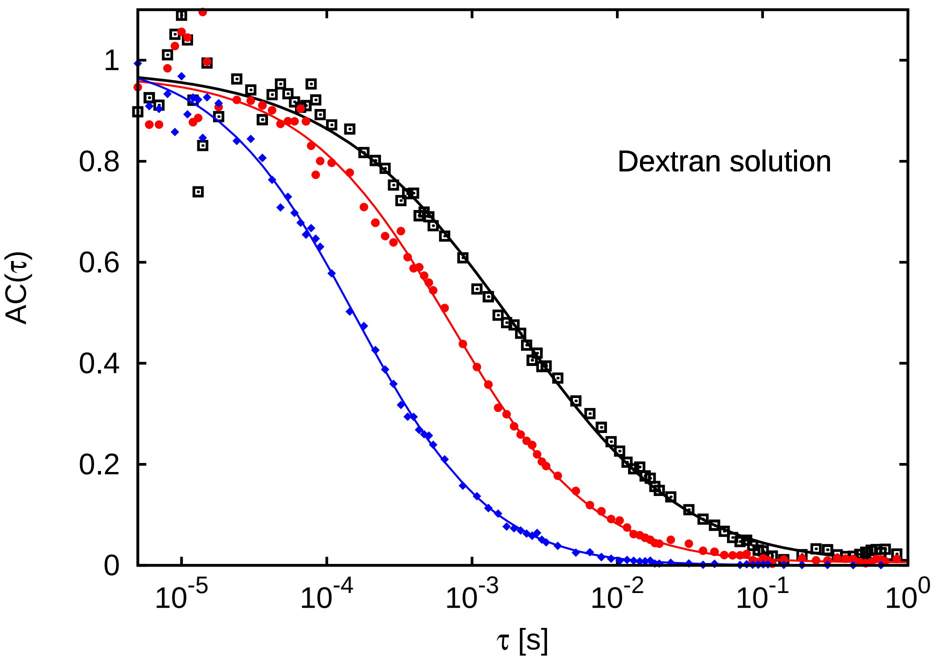

Dextran solution		
Concentration	τ_s [μs]	α
30 g/l	150	0.89
100 g/l	300	0.85
140 g/l	670	0.82
360 g/l	2000	0.72
100 g/l, solvent: water + EtOH (60:40)	960	0.97

Figure 5.8: Representative FCS curves of 5 nm gold beads diffusing in dextran solutions with concentrations of 30 g/l, 140 g/l, 360 g/l (blue diamonds, red dots, black squares). Fitting with Equation 5.1 yields subdiffusion with an anomaly α that declines when the concentration increases (full lines).

The second series of test measurements was done for nanogold in a fluid extract from egg cells of the frog Xenopus Laevis. Xenopus egg extract is typically used to do in-vitro studies of biochemical and biophysical processes under conditions which are similar to living cells. The extract is obtained by breaking large egg cells and preserving their contents, i.e. proteins, lipids and other macromolecules, in similar concentrations as they occur in cells.

Here, nanogold diffusion was measured with FCS in undiluted and diluted Xenopus egg extract (see Figure 5.9 for representative FCS curves and a table with the measured values). For the undiluted extract, an anomaly degree $\alpha = 0.52$ and a residence time $\tau_s = 370\ \mu s$ was detected, which is similar to the values in the cyto-

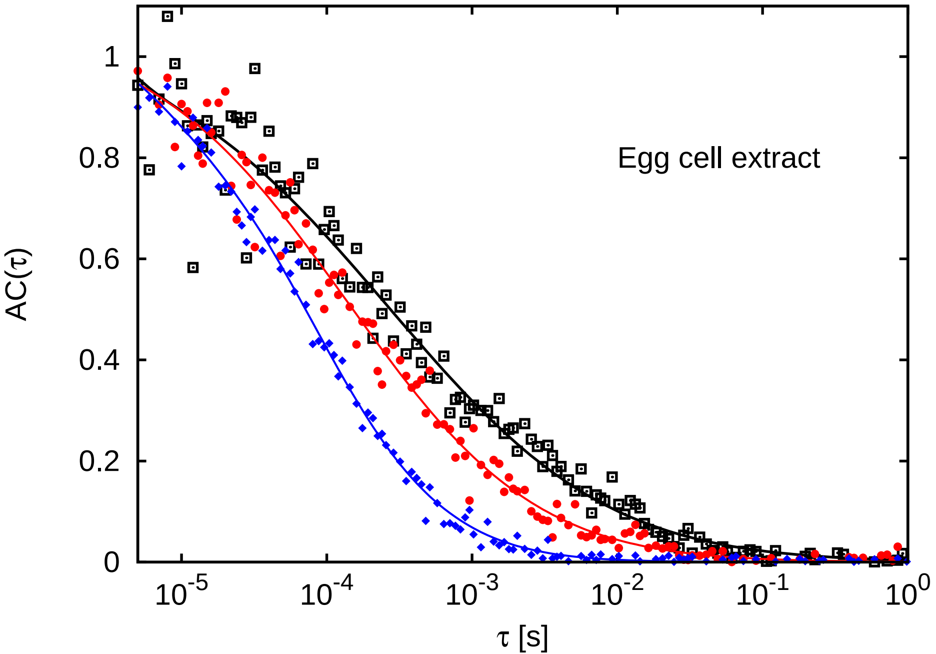

Xenopus egg cell extract				
Concentration	τ_s [μs]	α	$G'(100Hz)$ [Pa]	$G''(100Hz)$ [Pa]
100%	370	0.52	1.11	1.22
50%	283	0.54	0.87	1.00
25%	244	0.57	0.67	0.86
12.5%	172	0.60	0.46	0.64
6.25%	120	0.59	0.40	0.54
3.125%	124	0.68	0.21	0.39
1.5%	141	0.74	0.15	0.35
1%	120	0.80	0.08	0.24
0.1%	121	0.91	0.02	0.15
0.01%	122	1.00	0.00	0.10

Figure 5.9: Representative FCS curves of 5 nm gold beads diffusing in (diluted) Xenopus egg cell extracts with concentrations of 0.1%, 3.125%, 50% (blue diamonds, red dots, black squares). Fitting with Equation 5.1 yields subdiffusion with an anomaly α that increases under dilution of the extract (full lines).

plasm and the nucleoplasm of living cells. Upon dilution of the extract, α increased towards unity, while τ_s subsided (see Figure 5.9 and Figure 5.10).
Both measurement series in dextran solutions and egg extract show that the anomaly degree α of nanogold diffusion depends at least partially on the molecule concentration in an examined fluid and can thus be used to estimate the 'crowdedness' of the fluid, in agreement with [44]. The measurements underline that cytoplasm and nucloplasm of cells have to be regarded as very crowded environments. Their 'crowdedness' is clearly higher than that of dextran solutions: Macromolecule concentrations in cells lie typically between 100 and 400 g/l [36], and cells show $\alpha \approx 0.55$, whereas dextran solutions with similar concentrations (30 - 360 g/l) produce only $\alpha \approx 0.89$ - 0.7. A reason for this enhanced crowding degree in cells may be that the differently sized and typically compact macromolecules in cells cause a higher volume occupancy than the long and branched polymers in dextran solutions. Further, interactions between the intracellular macromolecules may contribute to crowding. The latter assumption is supported by the observation that in diluted egg extracts low α values (and thus high crowding degrees) were detected over a broad range of dilutions.
The qualitative rating of cytoplasm and nucleoplasm as very crowded environments is of special interest since strong crowding has consequences for the hydrodynamics and the thermodynamics of a system (c.f. Sections 3.1.3.3 and 3.1.4). In particular in cells it may have significant effects e.g. on protein folding, protein stability, protein aggregation, pattern formation and chemical and enzymatic reactions.

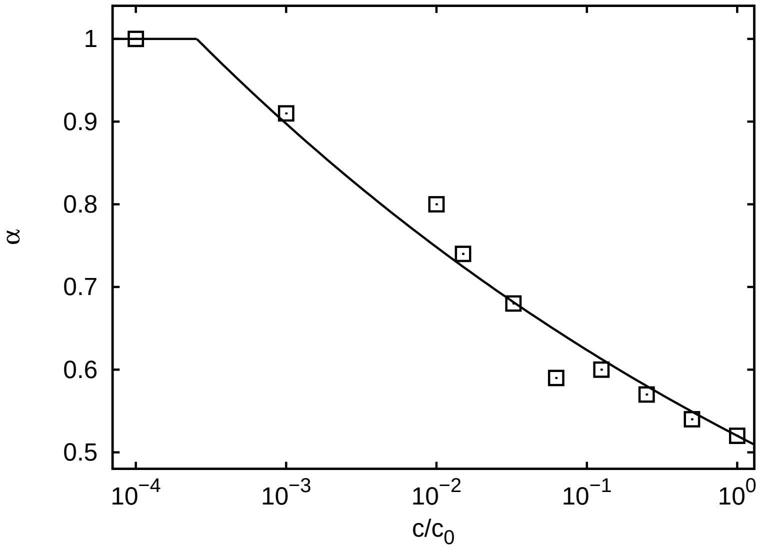

Figure 5.10: The anomaly degree α measured in Xenopus egg cell extracts (initial concentration c_0) tends to unity upon dilution of the extract. The full line interpolates below which extract concentration $\alpha = 1$ (i.e. normal diffusion) should be reached.

Different tracers

The appearance of subdiffusion depends a) on the crowding state of the embedding fluid and b) on the tracer size and shape. To test the behaviour of other tracers than nanogold, fluorescently labeled BSA protein (diameter 6 nm) was microinjected in Hela cells and its diffusion was measured with FCS (see Figure 5.11 for a representative curve). The average diffusion time of BSA in the cytoplasm was $\tau_s \approx 320$ μs, the anomaly degree was $\alpha \approx 0.5$, which is comparable to the values of nanogold. Further on, the fluorescent protein eGFP (diameter 3 - 4 nm) was expressed in Hela cells and its diffusion was measured with FCS. As a result, eGFP showed in the cytoplasm an average diffusion time of $\tau_s \approx 500$ μs and an anomaly $\alpha \approx 0.95$. This finding of nearly normal diffusion of eGFP in cells agrees with Reference [67] and is very likely due to the smaller size of eGFP as compared to nanogold and BSA.

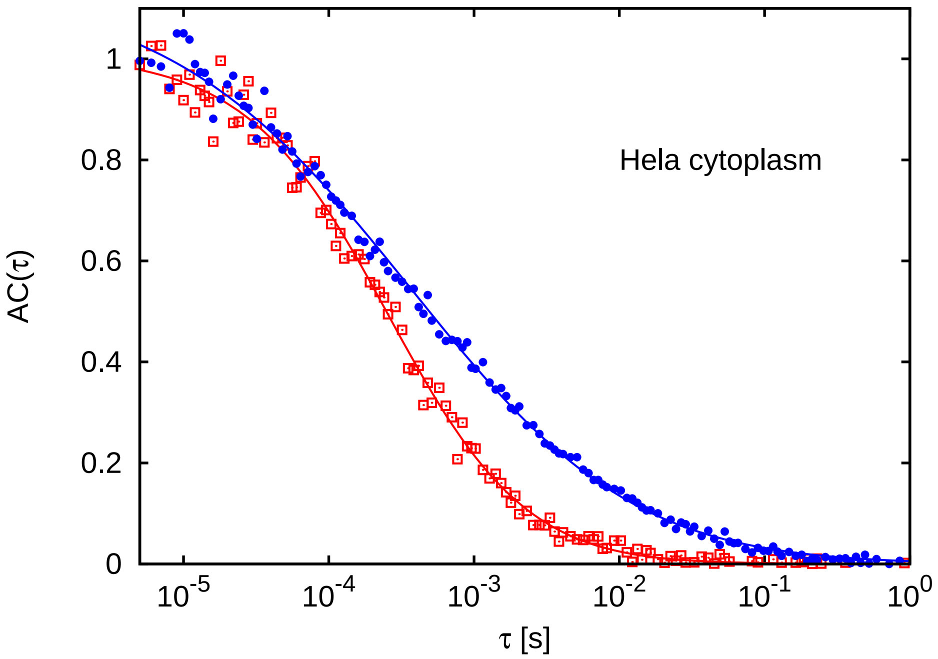

Figure 5.11: FCS measurement of BSA proteins (blue dots) and eGFP fluorophores (red squares) diffusing in the cytoplasm of Hela cells. Fitting with Equation 5.1 yields strong subdiffusion with $\alpha = 0.5$ for BSA, but only weak subdiffusion with $\alpha = 0.95$ for eGFP (full lines).

General conclusion for macromolecule diffusion in cells

It was determined here that spherical nanogold particles (diameter 5 nm) show strong subdiffusion ($\alpha \approx 0.55$) in the cytoplasm and the nucleoplasm of cells. When we compare this result to available intracellular FCS measurements on proteins of similar size, we find that these proteins show a similar behaviour: For the BSA protein (diameter $\approx$ 6 nm) subdiffusion with $\alpha \approx 0.5$ was detected (see above), while in an earlier study for the IgG antibody protein (diameter $\approx$ 10 nm) subdiffusion with $\alpha \approx 0.55$ was measured [44]. Also the diffusive behaviour of nanogold in dextran solutions of different concentrations is comparable to measurements on proteins in dextran solution: while for nanogold here subdiffusion with $\alpha \approx 0.72$ - 0.89 was observed, the streptavidin protein (diameter $\approx$ 5 nm) showed subdiffusion with $\alpha \approx 0.7$ - 0.8 [68]. We can conclude from these agreeing measurements that many intracellular macromolecules which are comparable in size will show a similar subdiffusive behaviour as nanogold does. This is an important consideration since subdiffusion of molecules can have strong effects on many processes in which they are involved: the kinetics and equilibria of chemical and enzymatic reactions change significantly [71, 72, 73, 74, 76] and the formation of patterns is stabilised [83]. And, as a another noteworthy effect, it will be shown in Chapter 6 that subdiffusion facilitates under suitable conditions the target finding of a diffuser.

5.4.2 Rheological properties of the cellular interior

From the diffusion parameters of nanogold in cells the rheological properties of cytoplasm and nucleoplasm on the nanoscale were determined. To do so, the procedure proposed by Mason & Weitz was used, in which the complex shear modulus $G(\omega)$ of a medium is obtained via a generalised Einstein-Stokes relation from the mean square displacement *MSD* of diffusing probe particles (c.f. Section 4.4). The nanogold particles used here to probe the interior of cells fulfilled the requirements to be spherical and rigid made by Mason & Weitz [1]. The *MSD* of the nanogold particles was calculated from the diffusion parameters τ_d, τ_s and α as measured with FCS (c.f. Methods Section 5.3). It is important to realise here that the validity of $G(\omega)$ as determined from diffusion data depends on the size of the probe particles. If the medium under investigation is not homogenous but has different types of structuring elements on different length scales, it will also show different rheological behaviour when examined on different length scales, i.e. with probe particles of different sizes. With the nanogold particles used here, the rheological behaviour of cells on the nanoscale was probed.

Cytoplasm and nucleoplasm are viscoelastic on the nanoscale
Calculating $G(\omega)$ from the *MSD* of nanogold beads yielded for all examined cell lines that cytoplasm and nucleopasm have the characteristics of viscoelastic fluids. Their elastic moduli $G'(\omega)$ and the viscous moduli $G''(\omega)$ were clearly larger than zero for all frequencies between 10^1 and 10^5 Hz. Both $G'(\omega)$ and $G''(\omega)$ were described by a power-law scaling: $G(\omega) \sim \omega^\alpha$, with $\alpha \approx 0.55$ (see Table 5.2), i.e. cytoplasm and nucleoplasm become stiffer and more viscous with increasing frequency of shearing. Typically, cytoplasm and nucleoplasm were governed by the viscous modulus $G''(\omega)$ for small frequencies $\omega < 1$ Hz, while for larger frequencies the elastic and the viscous moduli were of the same order of magnitude.
The detected viscoelastic behaviour of $G(\omega)$ was similar for all 10 tested cell lines, with slight differences in the scaling exponents and the relative strengths of G' and G'' (see table 5.2). Curves of $G'(\omega)$ and $G''(\omega)$ for cytoplasm and nucleoplasm of HeLa cells are shown in Figure 5.12. Typical values of the moduli at $\omega =$ 10 Hz were $G' \approx G'' \approx 0.3$ Pa, which compares favourably to measurements in concentrated/crowded actin solutions [151].

Previous measurements on cell rheology determined already that cells are viscoelastic on the micron scale, where their rheological behaviour is determined mainly by the cytoskeleton; also nuclei were shown to be viscoelastic on the micron scale. Absolute values $|G(\omega)|$ of the intracellular viscoelasticity on the micron scale are larger by factors of 20-50 than the absolute values of $|G(\omega)|$ measured here on the nanoscale. In some of the micron-scale studies, the complex shear modulus was observed to follow over several decades in ω a power-law $G(\omega) \sim \omega^x$, similar to the behaviour detected here on the nanoscale. Measuring methods

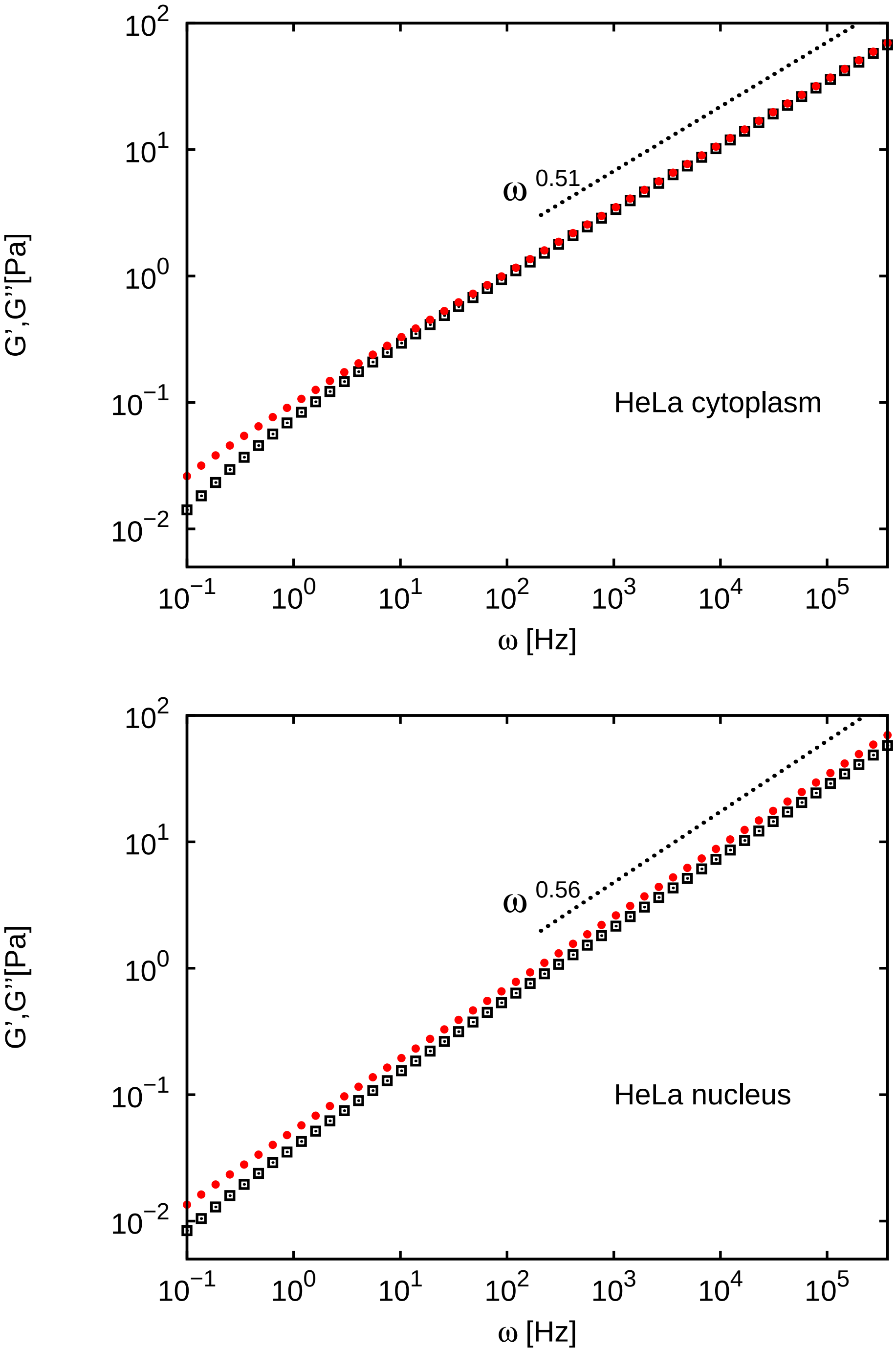

Figure 5.12: Average real (elastic; black squares) and imaginary (viscous; red dots) parts of the complex shear modulus $G(\omega)$ in the cytoplasm and nucleus of HeLa cells. The dashed lines highlight the power-law increase $G(\omega) \sim \omega^{\alpha}$.

Cell line	**Cytoplasm**		
	α	$G'(100Hz)$ [Pa]	$G''(100Hz)$ [Pa]
HeLa (human cervix cancer)	0.51	1.00	1.06
BXPC (human adenocarcinoma)	0.52	1.40	1.55
TP366 (human glioblastoma)	0.55	0.77	0.92
TP98G (human glioblastoma)	0.56	0.82	1.01
U2OS (human osteosarcoma)	0.53	0.88	0.99
PLC (human hepatoma)	0.52	0.65	0.71
HepG2 (human hepatoma)	0.52	1.26	1.82
Thle (human liver)	0.48	1.28	1.24
3T3 (mouse fibroblasts)	0.59	0.96	1.31
CHO (chinese hamster ovary)	0.52	1.47	1.63

Cell line	**Nucleoplasm**		
	α	$G'(100Hz)$ [Pa]	$G''(100Hz)$ [Pa]
HeLa (human cervix cancer)	0.56	0.57	0.70
BXPC (human adenocarcinoma)	0.56	0.75	0.92
TP366 (human glioblastoma)	0.55	0.63	0.75
TP98G (human glioblastoma)	0.63	0.52	0.80
U2OS (human osteosarcoma)	0.62	0.50	0.75
PLC (human hepatoma)	0.62	0.29	0.43
HepG2 (human hepatoma)	0.58	0.96	1.28
Thle (human liver)	0.53	0.90	1.01
3T3 (mouse fibroblasts)	0.60	1.24	1.76
CHO (chinese hamster ovary)	0.54	1.59	1.88

Table 5.2: Scaling exponent α, real (elastic) part $G'(100Hz)$ and imaginary (viscous) part $G''(100Hz)$ of the complex shear modulus $G(\omega) \sim \omega^{\alpha}$ for 10 cell lines.

relying on the external deformation of entire cells, like atomic force microscopy or magnetic twisting cytometry, detected power-law exponents x between 0.1 and 0.4 [102, 108], whereas intracellular measurements detected exponents $x \approx 0.75$ [11]. In these micron scale measurements, the elastic component typically was stronger than the viscous component, while in the measurements on the nanoscale presented here both components were about equal. For low ω values, the micron scale structure of cells was determined to respond almost purely elastically [11], whereas the low-ω-response in the nanoscale measurements was mainly viscous.

The Zimm model for diluted polymer solutions yields a heuristic description of viscoelastic intracellular fluids

Measuring the nanoscale viscoelasticity gives a quantitative description of the rheological properties of intracellular fluids as caused by dissolved macromolecules. The previous conclusion that the degree of macromolecular crowding is very high in intracellular fluids represents a more qualitative statement. The rheological description enhances the crowding picture since the viscoelasticity of a fluid depends not only on the number of dissolved macromolecules but also on their mobilities and their mutual interactions.

The power-law increase of $G(\omega) \sim \omega^{\alpha}$ with $\alpha \approx 0.55$ measured in cells indicates a power-law distribution of relaxation times for the intracellular fluids [152]. Generally, each macromolecule in a crowded fluid is obstructed and may be connected with other molecules via weak unspecific bindings, i.e. with energies of the order of thermal energy. The movement of a macromolecule therefore requires unentangling, reptation, dissociation and/or the circumvention of obstacles. These actions possess local relaxation time scales that differ greatly and may lead to a power-law spectrum of relaxation times. A particular realisation of a complex fluid with a broad spectrum of relaxation times is given by the Zimm model for dilute polymer solutions [153], which predicts for the scaling of the complex shear modulus:

$$G(\omega) \sim B \left\{ \begin{array}{ll} (\tau_R \omega)^{5/9} & \text{good solvent} \\ (\tau_R \omega)^{2/3} & \Theta\text{-solvent} \end{array} \right. \tag{5.9}$$

with $B \approx 1$ and $\tau_R = \frac{\eta R_g^3}{2 k_b T}$. Here, η denotes the pure solvent viscosity and R_g the radius of gyration of the polymers. A 'good' solvent is in the Zimm model defined as a fluid where the solvent molecules and solute molecules attract each other, whereas the solute molecules repel each other. A 'bad' solvent would mean the opposite: solvent and solute repel each other while the solvent molecules attract each other (thus leading to an agglomeration of solute molecules). The Θ-solvent describes the intermediate case between good and bad solvent: here repulsion and attraction balance each other exactly.

Comparing the complex shear modulus $G(\omega) \sim \omega^{\alpha}$, $\alpha \approx 0.55$ which is typically measured in cells with Equation 5.9 yields a surprisingly good agreement of the cell's nanoscale viscoelasticity with the Zimm model under good solvent conditions. This observation suggests that the Zimm model gives a heuristic description for the cytoplasm and the nucleoplasm of living cells, i.e. that the intracellular fluids behave similar to dilute polymer solutions. Taking this idea serious allows one to make several predictions from the Zimm model for the behaviour of intracellular fluids.

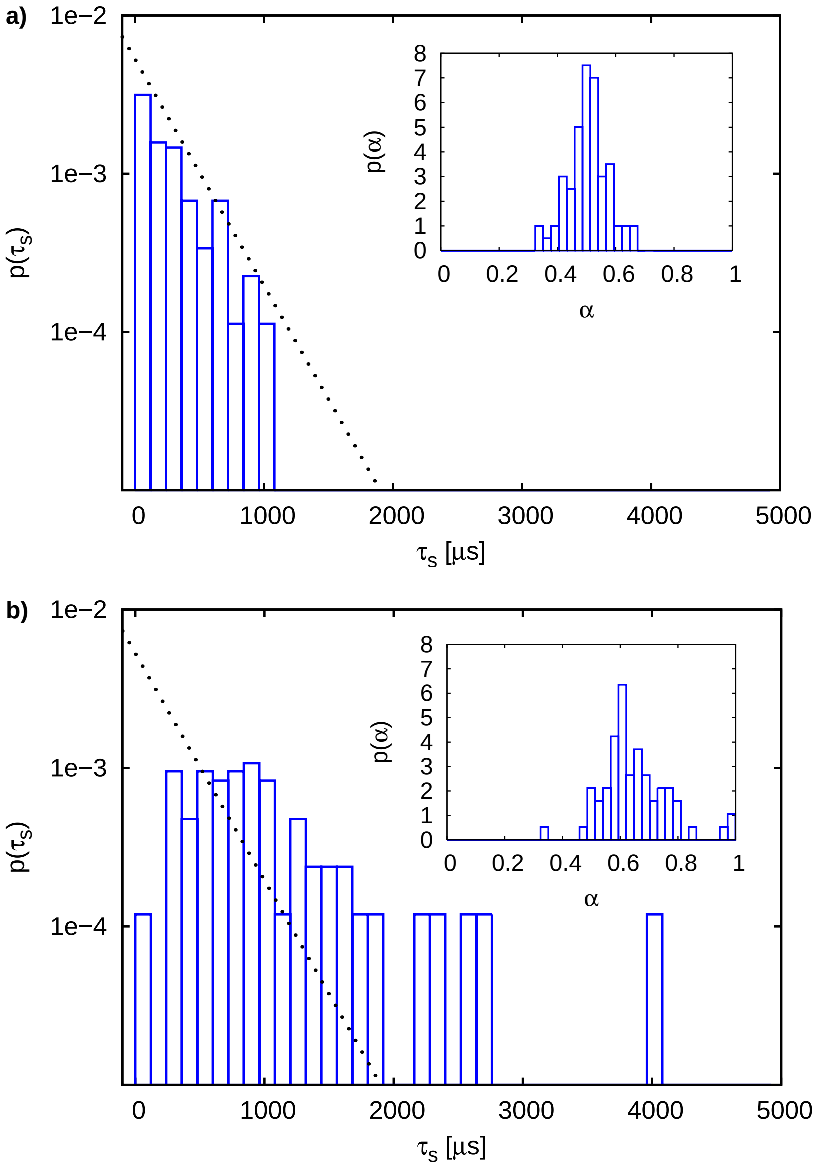

Figure 5.13: a) Distribution of the residence times $p(\tau_s)$ measured in the cytoplasm of unstressed HeLa cells. The dotted line indicates an exponential distribution $p(\tau_s)$. b) In HeLa cells stressed with 500 mM sucrose, the distribution $p(\tau_s)$ broadens and approaches a more uniform distribution. *Insets:* a) The distribution of anomalities $p(\alpha)$ is roughly Gaussian. b) Upon osmotic stress, a shift of the mean α is clearly visible.

At first, the distribution of residence times $p(\tau_s)$ can be estimated using the Zimm model. Since the mass m of a Zimm polymer is proportional to the number of monomers N and because the radius of gyration is given by $R_g \sim N^{3/5}$, it can be expected $\tau_R \sim R_g^3 \sim m^{9/5}$. Neglecting the crossover to normal diffusion for large times, i.e. assuming that anomalous subdiffusion is also the asymptotic mode of motion, one obtains $G(\omega) \sim (\tau_s \omega)^\alpha$ (c.f. Methods Section 5.3) and thus $\tau_s \sim \tau_R \sim m^{9/5}$. Since the distribution of masses in the cytoplasm is roughly exponential [44], the Zimm model predicts $p(\tau_s) \sim exp(\lambda \tau_s)/\tau_s^{4/5}$, i.e. for large residence times ultimately an exponential decay of p(τ_s) should be observed. This prediction is in fairly good agreement with the experimental data on the distribution of measured τ_s in Hela cells (see Figure 5.13).
The Zimm model further predicts a change in the scaling of the complex shear modulus $G(\omega)$ when the solvent conditions become worse, i.e. when the transition from a good solvent to a Θ-solvent takes place. To test the behaviour of intracellular fluids under a change of solvent conditions, the available solvent in Hela cells was reduced by stressing the cells osmotically. Then the complex shear moduli of the cytoplasm and the nucleoplasm were measured. The osmotic stressing was applied by putting cells into hypertonic growing media, i.e. media which have a higher solute concentration than the cellular interior and thus cause the osmotic extraction of water from the cells (see Methods Section 5.3 for details). The media were made hypertonic by adding osmolytes (sucrose, raffinose, NaCl or urea). Different osmolyte concentrations were tried, i.e. different 'strengths' of osmotic treatment:

a) sucrose: 300 mM, 500 mM and 1000 mM
b) raffinose: 500 mM
c) NaCl: 250 mM and 500 mM
d) urea: 300 mM and 500 mM

As a result, in osmotically stressed cells a significant change of nanogold diffusion was measured with FCS as compared to unstressed cells. In parallel, also $G(\omega) \sim \omega^\alpha$ as calculated from the diffusion parameters τ_s and α changed. Representative FCS curves from HeLa cells stressed with 500 mM sucrose are shown in Figure 5.14; the associated complex shear moduli $G(\omega)$ are shown in Figure 5.15.

Under weak osmotic treatment with 300 mM sucrose, a shift of the anomaly was observed from $\alpha = 0.51$ (unstressed) to $\alpha = 0.56$ in the cytoplasm of Hela cells. The diffusion time increased from $\tau_s = 300$ μs to $\tau_s = 850$ μs. Stronger osmotic stress with 500mM sucrose yielded an increase to alpha=0.66 and $\tau_s = 950$ μs (see Table 5.3). In the nucleoplasm, a similar effect for α was observed. τ_s showed an even stronger increase from $\tau_s = 200$ μs to $\tau_s = 1300$ μs at 300 mM sucrose and to $\tau_s = 1500$ μs at 500 mM sucrose. Inducing a stronger osmotic stress with 1000 mM sucrose, even a slightly higher increase to $\alpha = 0.68$ was observed and a considerable

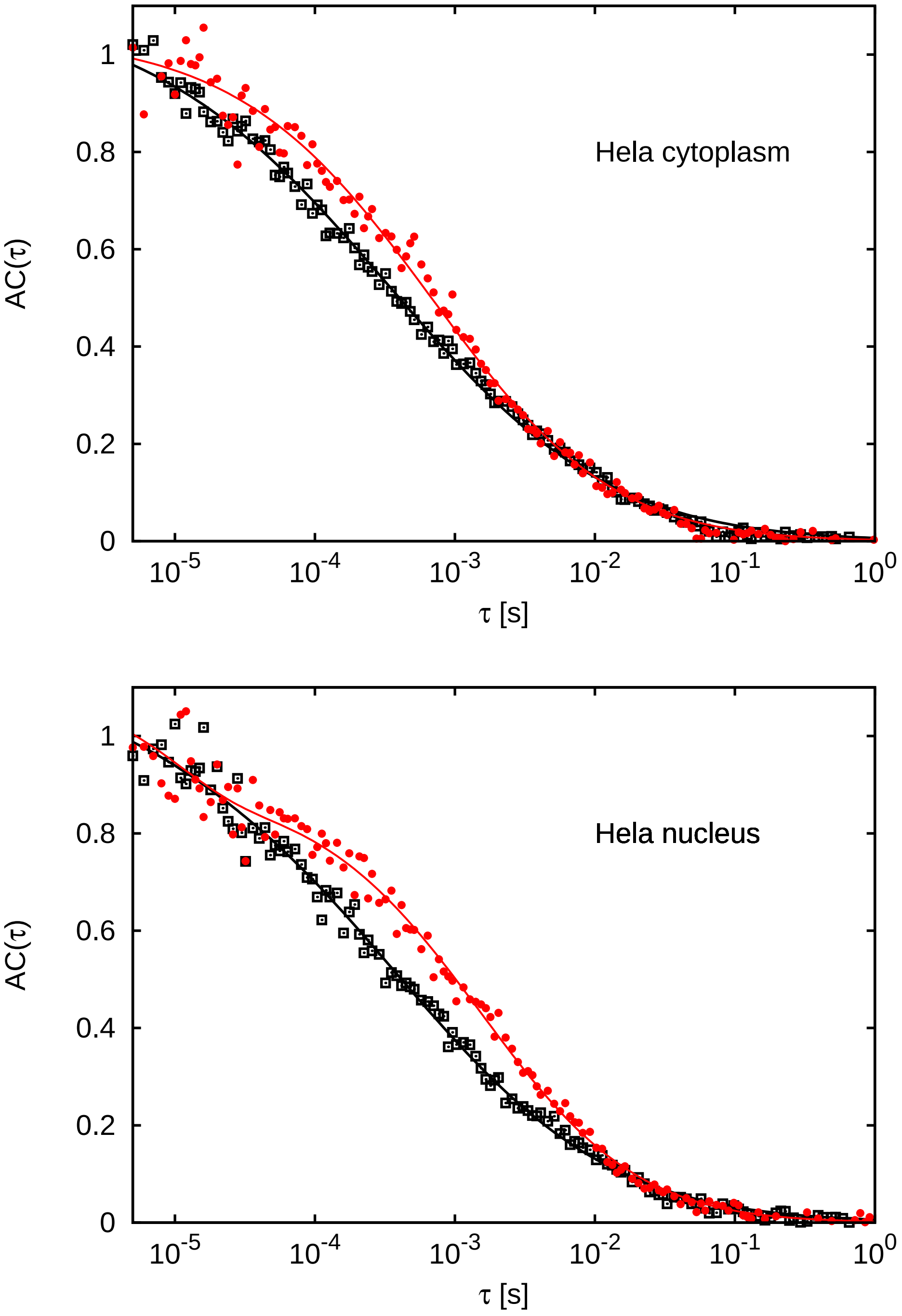

Figure 5.14: Representative FCS measurement curves of 5 nm nanogold beads diffusing in the cytoplasm and the nucleus of unstressed Hela cells (black squares) and Hela cells stressed with 500 mM sucrose (red dots). Fitting with Equation 5.1 yields subdiffusion (full lines) with $\alpha = 0.51$ (unstressed cells) and $\alpha = 0.66$ (osmotically stressed cells).

higher increase of $\tau_s = 2000\ \mu s$.
Similar effects were seen when using 500 mM raffinose and 500 mM NaCl as stress agents. Regarding the stress agents sucrose, raffinose, and NaCl, comparable concentrations induced the same effect on the measurements. NaCl, however, may represent a special case here, since it is twice as osmolar as sucrose due to its ionic composition and also is smaller in size, which means that it may be taken up by the cells in higher amounts than sucrose. A direct comparison between the two stress agents thus may not be appropriate. Adding urea hardly affected any of the parameters found for the cytoplasm of untreated cells, but did affect the parameters for the nucleus: the diffusion time τ_s was not strongly increased, whereas the anomaly was relaxed in a strength similar to that found with sucrose, raffinose, or NaCl (see Table 5.3). To assure that the detected change of diffusion under osmotic stress was not specific to Hela cells, also Thle and HepG2 cells were measured under osmotic conditions (500 mM sucrose) and showed similar effects (see Table 5.3).
In summary, in hyperosmotically stressed cells both the residence time τ_s and the anomaly α increased. In terms of the complex shear modulus, this means that $G(\omega) \sim \omega^\alpha$ changed its scaling to a larger exponent upon osmotic stress, and the elastic contribution decreased with respect to the viscous modulus.

The obvious expectation for the experiment of reducing the amount of solvent water in cells is that crowding would be increased, and thus the anomaly be enhanced and the fluid be 'stiffened'. Although the detected increasing of the dwell time τ_s is in agreement with this expectation, the reduction of the anomaly (i.e. an increase of α) is surprising, since it indicates rather a reduction than an enhancement of crowding. Comparing the experimental findings for $G(\omega)$ to the prediction of the Zimm model Eq. 5.9, however, yields a good agreement: $G(\omega)$ changed its scaling to a larger exponent when the solvent became worse, and the elastic contribution decreased with respect to the viscous modulus (see Table 5.3).
An illustrative picture of the dynamics in a polymer solution wherein a solvent change takes place is the partial collapse of individual polymers, which reduces the degree of entanglement and the associated restoring forces. Changing solvent conditions in the heterogeneous intracellular fluids may also lead to a partial disentanglement and aggregation/collapse of protein complexes, and in consequence to the emergence of more aqueous voids; thereby the long-range restoring forces within the crowded fluids are reduced. Since a partial collapse/aggregation changes the distribution of the radii of gyration R_g, also a change in p(τ_s) can be expected for the measurements in osmotically stressed cells. Indeed, the distribution of residence times τ_s showed not only a considerable increase in the mean dwell time, but also a broadening of the entire distribution toward a more uniform appearance (see Figure 5.13).
In the measurements in osmotically stressed cells, the residence times τ_s had already increased at comparatively low concentrations of stress agents, whereas the anomaly α had gone up only slightly. In terms of the Zimm model, this behavior may reflect that the intracellular conditions did not change abruptly from a good to a Θ-solvent

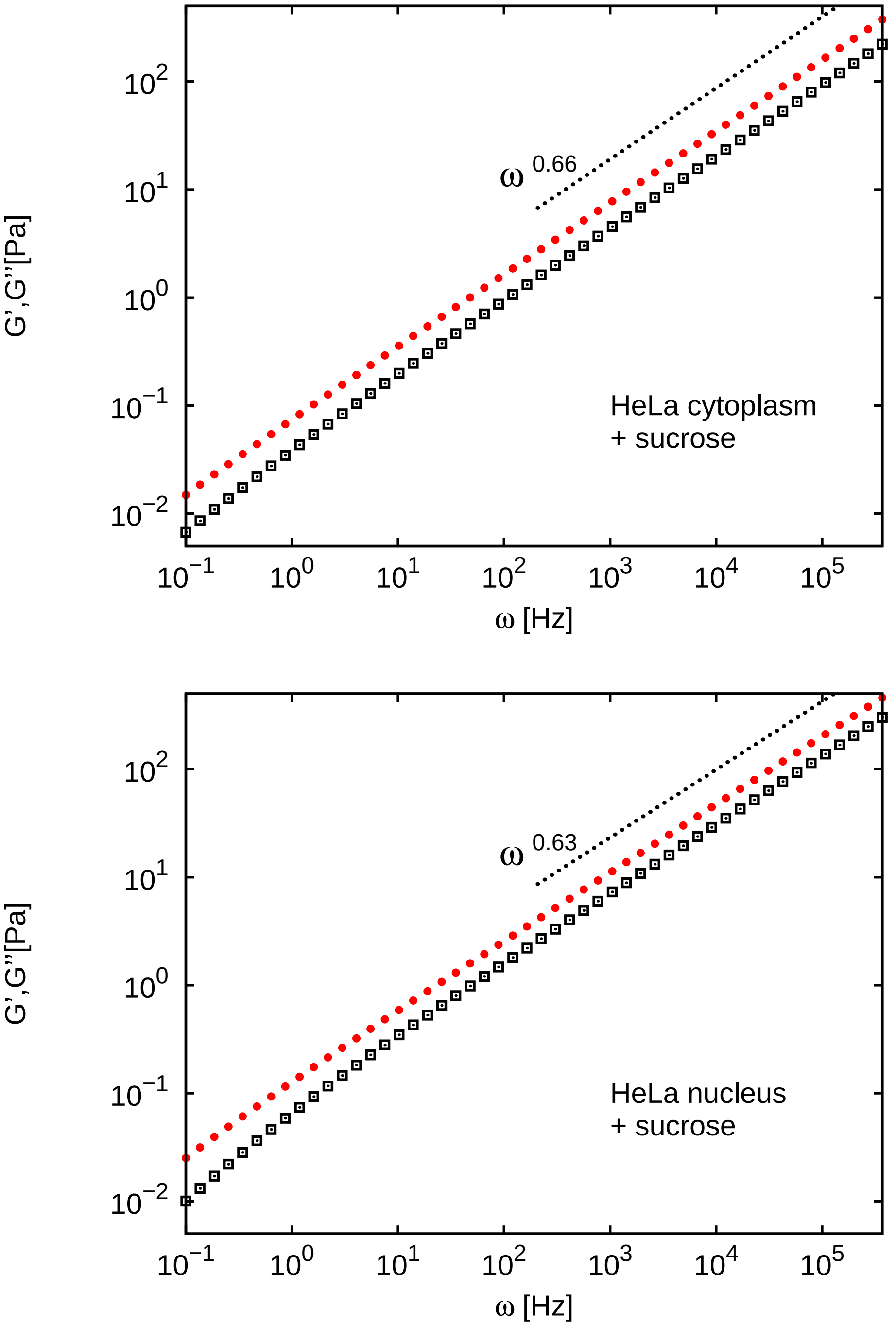

Figure 5.15: Average real (elastic; black squares) and imaginary (viscous; red dots) parts of the complex shear modulus in the cytoplasm and nucleus of HeLa cells stressed with 500 mM sucrose.

Cell line	**Treatm. [mM]**	**Cytoplasm**			
		τ_s $[\mu s]$	α	$G'(100Hz)$ [Pa]	$G''(100Hz)$ [Pa]
HeLa	none	270	0.51	1.00	1.06
HeLa	sucrose, 300	853	0.56	1.41	1.78
HeLa	sucrose, 500	954	0.66	0.94	1.64
HeLa	sucrose, 1000	1933	0.68	1.32	2.52
HeLa	raffinose, 500	1520	0.65	0.31	0.51
HeLa	NaCl, 250	742	0.52	1.57	1.74
HeLa	NaCl, 500	629	0.67	0.73	1.30
HeLa	urea, 300	361	0.5	1.26	1.82
HeLa	urea, 500	399	0.49	1.26	1.82
HepG2	none	767	0.52	1.60	1.78
HepG2	sucrose, 500	962	0.60	1.26	1.81
Thle	none	329	0.48	1.28	1.24
Thle	sucrose, 500	1164	0.60	1.41	2.02

Cell line	**Treatm. [mM]**	**Nucleoplasm**			
		τ_s $[\mu s]$	α	$G'(100Hz)$ [Pa]	$G''(100Hz)$ [Pa]
HeLa	none	162	0.56	0.57	0.70
HeLa	sucrose, 300	1830	0.55	2.18	2.71
HeLa	sucrose, 500	1799	0.63	1.60	2.55
HeLa	sucrose, 1000	2020	0.69	1.30	2.58
HeLa	raffinose, 500	2387	0.65	0.41	0.68
HeLa	NaCl, 250	932	0.51	1.83	1.98
HeLa	NaCl, 500	655	0.60	0.59	1.18
HeLa	urea, 300	396	0.6	0.76	1.07
HeLa	urea, 500	212	0.65	0.38	0.63
HepG2	none	502	0.58	0.96	1.28
HepG2	sucrose, 500	1840	0.53	2.33	2.74
Thle	none	270	0.53	0.90	1.01
Thle	sucrose, 500	940	0.68	1.84	1.57

Table 5.3: Mean residence time τ_s and anomaly degree α of 5 nm gold beads diffusing in osmotically stressed cells, real (elastic) part $G'(\omega)$ and imaginary (viscous) part $G''(\omega)$ of the complex shear moduli $G(\omega) \sim \omega^\alpha$ of osmotically stressed cells.

(which changes α), but rather there was a smooth transition with an initial increase in crowding (thus, a more hindered diffusion).

As described above, FCS measurements of nanogold diffusion in egg extract yielded similar results as in cells, i.e. $\alpha = 0.52$. Calculating the associated complex shear modulus $G(\omega)$ shows that the egg extract is also viscoelastic on the nanoscale, with $G(\omega) \sim \omega^{\alpha}$, $G'(100Hz) = 1.00\ Pa$, $G''(100Hz) = 1.09\ Pa$. The similarity of cell extract to living cells is evident, since the extract has the same macromolecule composition and a similar state of dilution as the intracellular fluids of the egg cells from which it is taken. Upon dilution of the extract with water, α increased only slowly, i.e. the subdiffusive and viscoelastic features were only slowly replaced by diffusive and purely viscous water-like behavior (see Figures 5.10 and 5.16). This observation highlights that the complexity of intracellular fluids is not a mere excluded-volume effect. Since subdiffusion and viscoelasticity still appear upon strong dilution, they seem also to take into account the lateral (attractive) interactions of proteins.

To further examine the effect of a solvent change as predicted in the Zimm model Eq. 5.9, it was tried to induce a solvent detoriation in the egg extract and in dextran solution by addition of ethanol. In the egg extract, the addition of even minute amounts of ethanol led to massive flocculation, making FCS measurements meaningless. This observation supports indirectly the reasoning that a change in solvent in cells due to osmotic stress may lead to a (partial) protein collapse and/or aggregation, thus leading to a change in α that agrees with Eq. 5.9. As a substitute, a dextran solution (dextran concentration 100 mg/ml) with pure water as solvent was compared to dextran solution with a water/ethanol mixture (60:40) as solvent. FCS measurements on nanogold diffusion revealed a strong change in the subdiffusion and thus in the scaling of $G(\omega)$ when the water/ethanol solvent was used (see table associated to Figure 5.8). On average, water as solvent yielded $\alpha = 0.85$, $\tau_s = 300$ μs, whereas water/ethanol as solvent resulted in $\alpha = 0.97$, $\tau_s = 960\ \mu s$. Although the Zimm model Eq. 5.9 is not a good quantitative description here at least a good qualitative agreement with the findings on intracellular fluids can be stated. Most likely, the utilized (almost monodisperse and low-weight) dextran did not equip the crowded fluid with enough degrees of freedom to actually reach the fully developed broad range of relaxation times that underlies Eq. 5.9.

In conclusion, the experiments and observations described here support strongly the hypothesis that the cytoplasm and the nucleoplasm are phenomenologically described by the Zimm theory; the intracellular fluids behave thus – from a rheological point of view – similar to viscoelastic dilute polymer solutions. This can be understood in the sense that dissolved macromolecules in cytoplasm and nucleoplasm are connected via weak nonspecific interactions to network-like variable nanostructures which possess in their entirety the viscoelastic properties being described by $G(\omega) \sim \omega^{\alpha}$, $\alpha \approx 0.55$. Especially two of the observations mentioned above are in agreement with this picture. Firstly, the scaling exponent α was increased in hyperosmotically stressed cells compared to unstressed cells; an obvious explanation for this behaviour is a change of the average nonspecific interactions between macromolecules due to a reduction of the water solvent, leading to a change of the network's $G(\omega)$. Secondly, it was observed that intracellular fluids keep their strong viscoelastic behaviour even under a dilution up to a factors larger than 10; this finding indicates again that the nanoscale viscoelasicity appears not only due to steric repulsion of macromolecules, but also due to attractive interactions. A similar case for a network-like structure with viscoelastic properties can be found for example in the cytoskeleton.

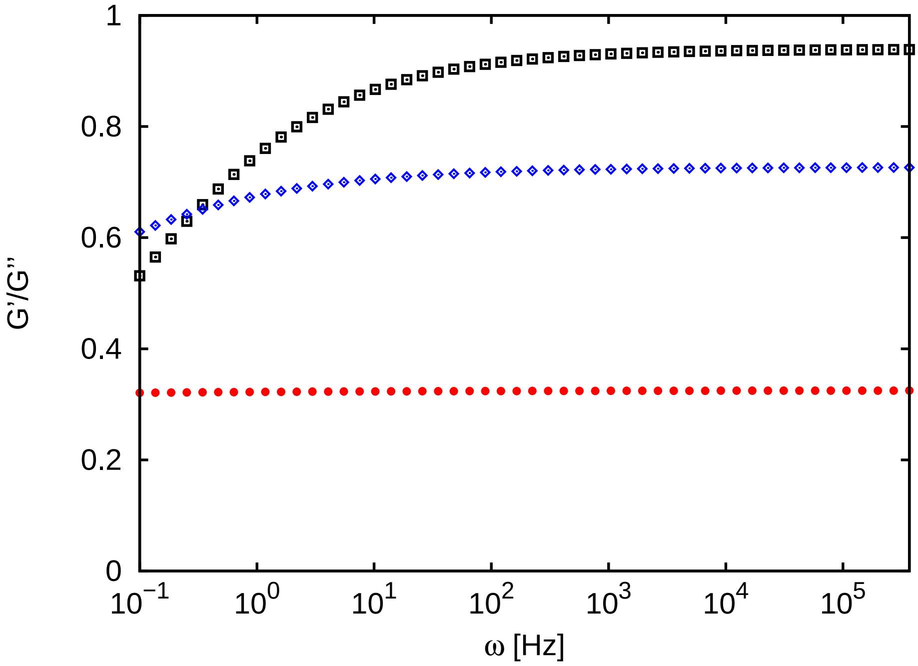

Figure 5.16: Ratio of the elastic modulus $G'(\omega)$ to the viscous modulus $G''(\omega)$ of cell extract. The ratio tends to zero upon dilution of the extract, i.e. the extract becomes purely viscous. $c/c_0 = 100\%$ (black squares), 12.5% (blue diamonds), 1% (red dots) (with c_0 being the initial concentration).

5.4.3 Comparison of different cell types

The measurements presented in this work were done in 10 different cell lines: 7 of them were cancer cell lines, 3 were derived from healthy tissue. The cell lines included samples from different organs and tissues (cervix, brain, bone, liver, muscels, ovaries) and from different mammalian species (human, mouse, chinese hamster). In all cell lines, microinjected nanogold showed strong subdiffusion in the cytoplasm and the nucleoplasm. As a consequence, the intracellular fluids in all cells were determined to be viscoelastic on the nanoscale, with a power-law scaling of the viscoelasticity $G(\omega) \sim \omega^{\alpha}$. The viscous and elastic contributions were typically similar at high frequencies ($\omega > 100$ Hz), whereas viscous behaviour was dominating for low frequencies, with a viscous modulus that was in maximum about fivefold larger than the elastic modulus.

Comparing the 10 investigated cell lines in detail, only minor differences became visible for the parameters τ_s and α. The anomaly degree α varied between 0.48 and 0.63 in the different cell lines; the residence time τ_s was measured to lie between 98 μs to 780 μs (see Table 5.1 and associated diagramms). A correlation of the cell-to-cell variations of α and τ_s with the health state of cells or with the tissue from which they were derived could not be discovered. In the three liver cell lines Thle, PLC and HepG2 (of which PLC and HepG2 are cancer cells), for example, the values of α and τ_s did not show a specific similarity, but rather covered almost the entire range between the maximum and minimum values detected in all cell lines. Accordingly, the viscoelastic behaviour as measured by the complex shear modulus $G(\omega)$ was very similar; to illustrate this, the absolute value $|G(\omega)|$ and the ratio of the elastic to the viscous modulus G'/G'' are plotted for two different cell lines in the Figures 5.17 and 5.18.

Previous studies on cell mechanics demonstrated that the macroscale viscoelasticity of entire cells was reduced in malignant cells compared to healthy specimen, which was ascribed to a more disordered structure of the cytoskeleton in cancer cells [121, 103, 122]. In particular, the study of Guck et al. [120] detected the metastatic potential of cancer cells to be reflected in a specific macroscale viscoelasticity. Bearing this in mind, a comparison of the nanoscale viscoelasticity of cancer cells and healthy ones was tried here. In cancer cells the nucleus is typically enlarged as compared to healthy cells. Thus, the ratio $\mathcal{R}$ of the cross section of the entire cell to the cross section of the nucleus is a simple measure for the aggresivity of a tumor cell. Here, this ratio was determined for all cell lines from microscopy images. A clear difference was visible for cells which were originally derived from healthy tissue ($\mathcal{R} \approx 6.5 - 7$) and cells from cancer tissue ($\mathcal{R} \approx 3.3 - 4.5$) (see Table 5.4). However, plotting τ_s and α of the different cell lines in dependence on $\mathcal{R}$ did not show any correlations (see Figure 5.19); a relation between the nanoscale viscoelasticity and cancer state of a cell therefore does not seem to exist.

The conclusion from the described observations is that the nanoscale viscoelasticity and thus the crowding state of cytoplasm and nucleoplasm are highly conserved in

Cell type	**Area ratio entire cell/nucleus**
HeLa (human cervix cancer)	3.38
BXPC (human adenocarcinoma)	3.58
TP366 (human glioblastoma)	4.51
TP98G (human glioblastoma)	4.00
U2OS (human osteosarcoma)	4.48
PLC (human hepatoma)	3.86
HepG2 (human hepatoma)	3.81
Thle (human liver)	6.70
3T3 (mouse fibroblasts)	6.52
CHO (chinese hamster ovary)	7.09

Table 5.4: Ratio of the cross section area of the entire cell to the cross section area of the nucleus for 10 different cell lines.

mammalian cells and do not depend on the cells' particular development or disease state.

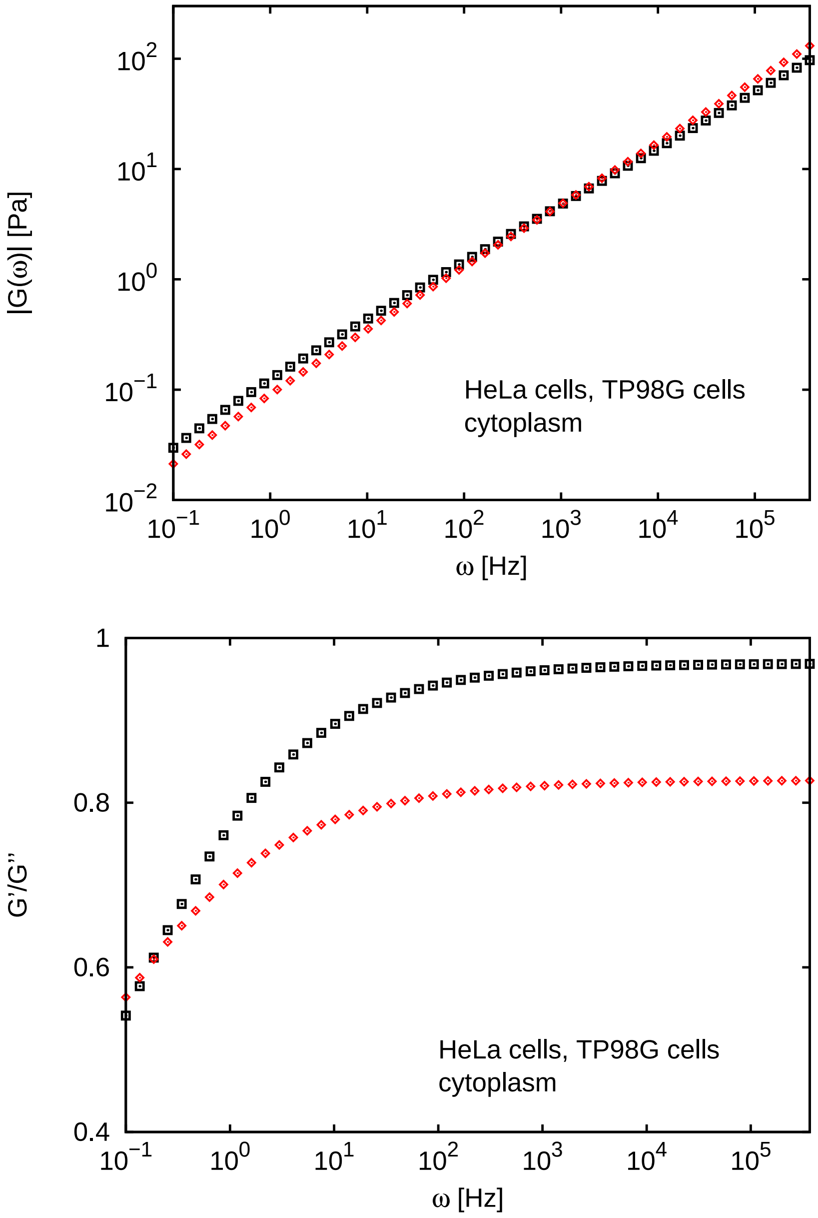

Figure 5.17: Absolute value $|G(\omega)|$ of the complex shear modulus and ratio between elastic (G') and viscous (G'') modulus for the cytoplasm of HeLa cells (black squares) and TP98G cells (red diamonds); the curves illustrate the similarity of the viscoelastic behaviour of both cell lines

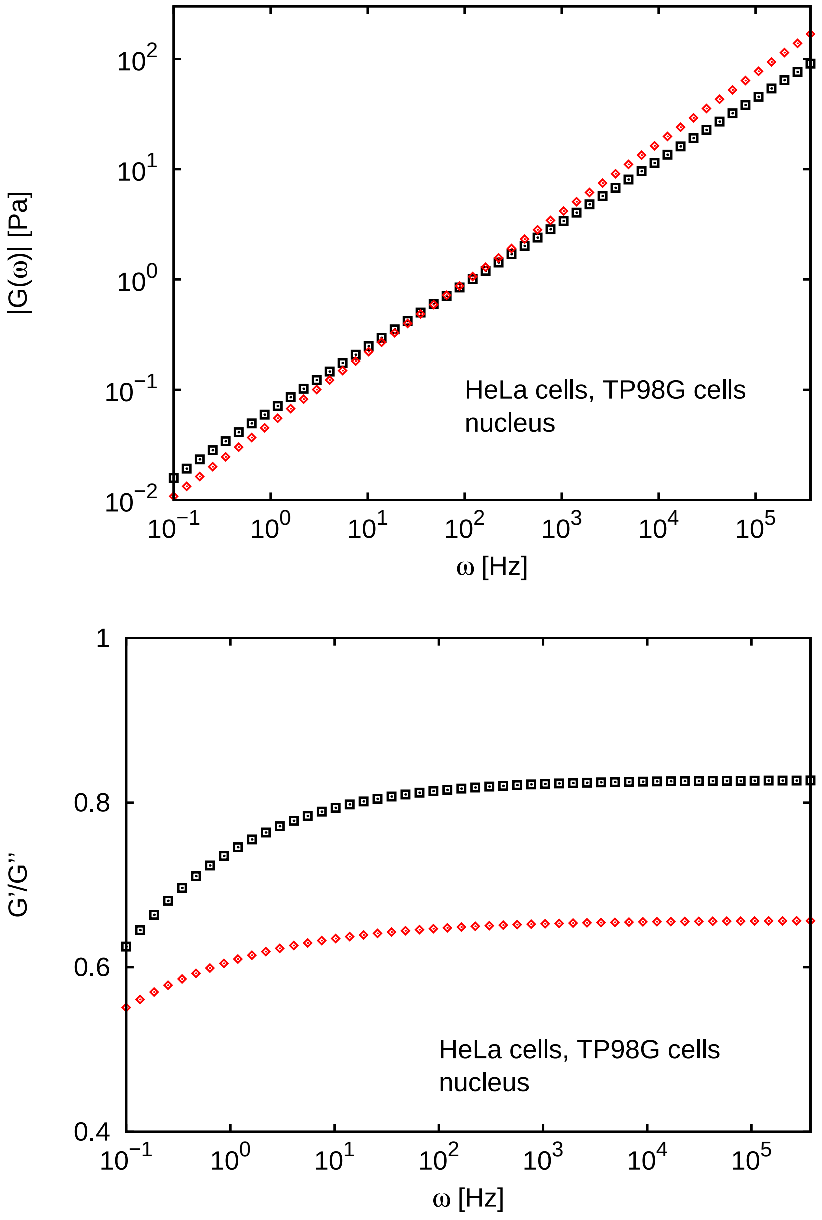

Figure 5.18: Absolute value $|G(\omega)|$ of the complex shear modulus; ratio between elastic (G') and viscous (G'') modulus; both for the nucleus of HeLa cells (black squares) and TP98G cells (red diamonds); the curves illustrate the similarity of the viscoelastic behaviour of both cell lines.

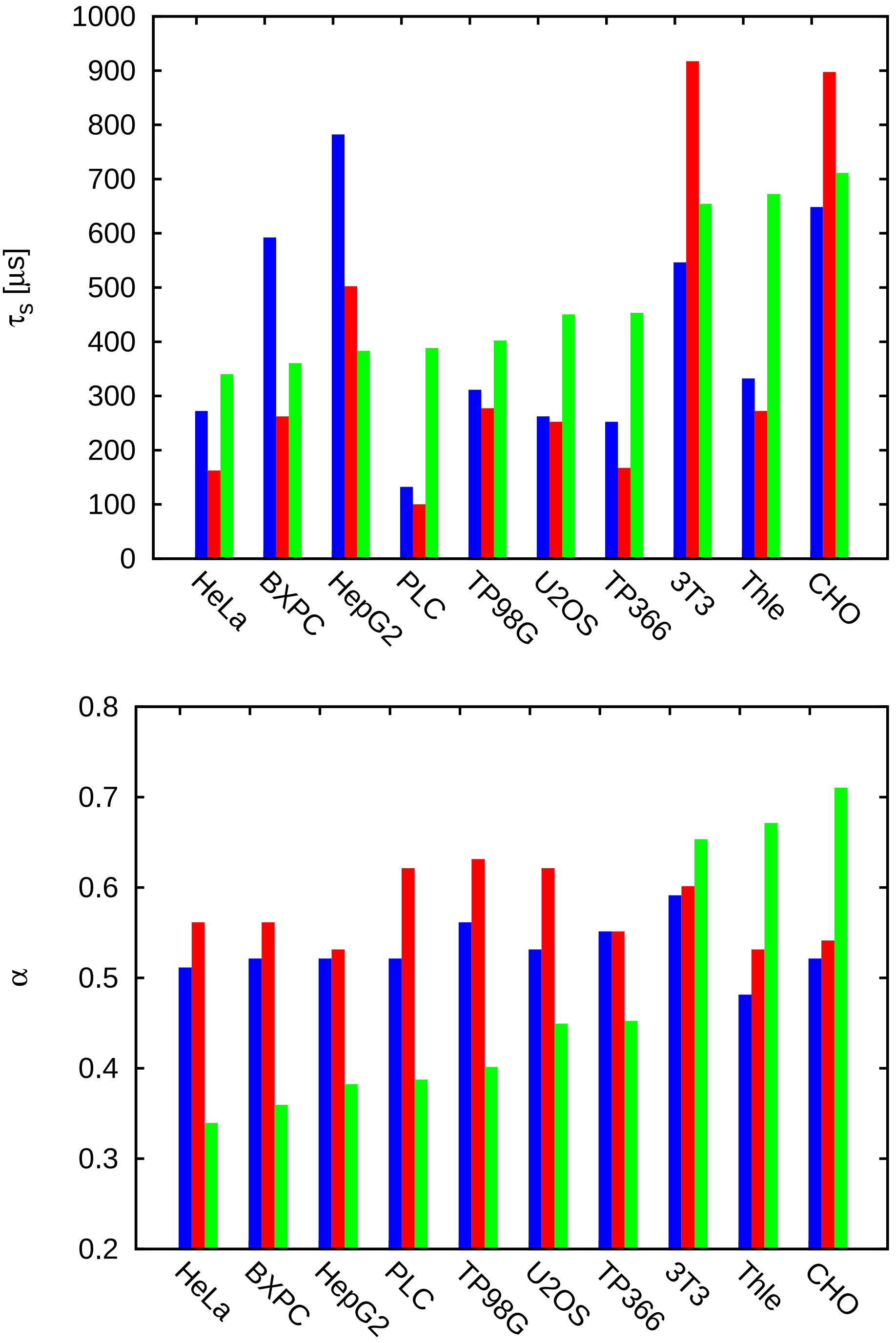

Figure 5.19: Residence times τ_s and diffusion anomalies α of 5nm gold beads diffusing in cytoplasm (blue, left columns) and nucleus (red, middle columns) for 10 cell lines, in order of the parameter $\mathcal{R}$ (green, right columns) that indicates the metastatic potential of a cell. No correlation between τ_s or α and $\mathcal{R}$ is seen.

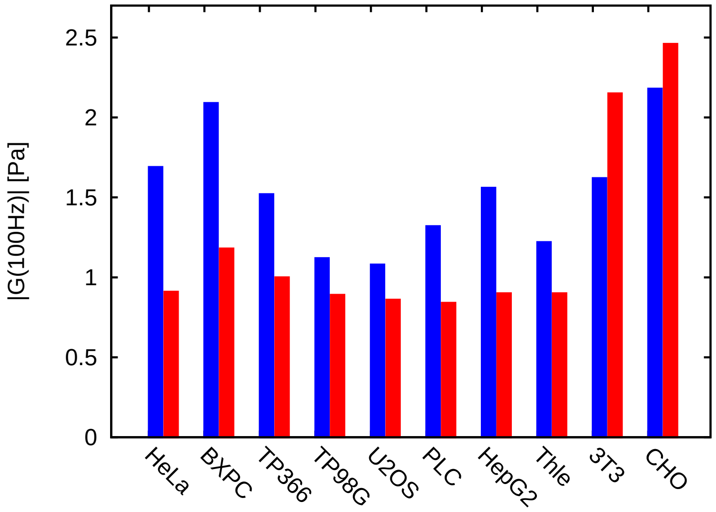

Figure 5.20: Absolute values of the complex shear modulus $|G|$ at $\omega = 100$ Hz for cytoplasm (blue, left columns) and nucleus (red, right columns) of 10 different cell lines.

5.4.4 Comparison of cytoplasm and nucleoplasm

The values of τ_s and α were compared for cytoplasm and nucleoplasm. In 9 of 10 investigated cell lines, α was consistently larger in the nucleus than in the cytoplasm. The differences of a cell's $\alpha_{cytoplasm}$ and $\alpha_{nucleus}$ were between 0.01 (3T3 cells) and 0.1 (PLC cells), which corresponds to α-differences by factors between 0.02 and 0.2. Only in TP366 cells, α_{nuceus} and $\alpha_{cytoplasm}$ were equal. τ_s was in 8 of 10 cell lines higher in the cytoplasm than in the nucleus by factors between 2.3 and 1.1, with the exceptions of 3T3 cells and CHO cells which showed the inverse behaviour of τ_s values that were higher in the nucleoplasm (see Table 5.1).

Elastic and viscous moduli were typically slightly higher in the cytoplasm than in the nucleoplasm (see Table 5.2 and Figure 5.20); the average ratio of the absolute values of the complex shear modulus was $\frac{|G_{cytoplasm}(100Hz)|}{|G_{nucleus}(100Hz)|} \approx 1.4$. This indicates that the cytoplasm was typically slightly stiffer and more viscous.

Since lower α values are a criterion for an increased crowding [44], the difference of α between cytoplasm and nucleus indicates that the interior of the nucleus is slightly less crowded than the cytoplasm. The particular organisation of the nucleus may be reflected here: the cytoplasm and the nucleus differ in their specific content of macromolecules, and especially the exclusive presence of condensed DNA chains in the nucleus may contribute to the particular crowding state of the nucleoplasm [34]. Nevertheless, although the crowding degree of the nucleus may be slightly lower than that of the cytoplasm, the nucleus is still in a regime that has to be regarded as highly crowded.

Chapter 6

Results II – Searching targets via subdiffusion

In this chapter the results of computer simulations are presented in which the probabilities of diffusive and subdiffusive particles to approach a target were determined; the simulation procedure, the obtained results and their interpretation are described and discussed in detail.

6.1 Problem definition

The experiments presented in Chapter 5 strongly indicate - in agreement with previous studies [67, 44, 68, 69] - that many macromolecules in cells move by subdiffusion due to obstruction via macromolecular crowding, or, in another picture, due to the nanoscale viscoelasticity of the intracellular fluids. In particular, for the diffusion of various proteins and nano-sized testparticles in cells, anomaly values were measured that lie in a range of $\alpha \approx 0.5$ - 0.8. This is an important observation, since subdiffusion of molecules was demonstrated to influence various processes relevant in biology, for example chemical and enzymatic reactions and pattern formation (see Section 3.1.3.3).

In the present section, a more fundamental effect of subdiffusion will be studied. Considering biological reactions, typically at least one of the involved molecules is free in the intra- or extracellular environment and must approach its specific target (e.g. a reaction partner or a binding site) by (sub)diffusion. At this, the question arises if the target finding efficiency of a tracer is different for normal and subdiffusive motion. Generally, it was shown already in various contexts that the efficiency of diffusive searching depends on the characteristics of the underlying random walk. It has been demonstrated, for instance, that – under particular conditions – target encounter rates increase when searchers use superdiffusive Lévy walks instead of normal Brownian motion [31, 32, 33]. As another example, it was highlighted that

average search times are reduced when diffusion is transiently restricted to a one or two-dimensional structure instead of taking place in three dimensions [30].
In the following, the efficiency of subdiffusion as a search mechanism will be quantified in terms of the target encountering probability P. To this end, computer simulations of a diffuse-to-capture scenario were performed, in which P was determined for particles moving by normal diffusion and subdiffusion of different anomaly degrees α. The results of the simulations was set into a biological context.

6.2 Simulation procedure

Simulation procedure

To determine the probability of getting captured at a target with radius a, a number of N individual, non-interacting particles were started on a sphere with radius R around the target's center. The (sub)diffusive random walk of each particle was followed up to a maximum time t_{max}, and the fraction of particles which contacted the target was recorded. The target's radius was used as an intrinsic length scale and set to unity for simplicity. The (sub)diffusive motion of the particles was simulated using the forward integration of the Langevin equation, i.e. the positions at times $t = 1, 2, \ldots, t_{max}$ were obtained via $x_i(t+1) = x_i(t) + \xi_i$ with $i = 1, 2, 3$. As a model for subdiffusion, the spatial increments ξ_i in each spatial direction $i = 1, 2, 3$ were calculated via the Weierstrass-Mandelbrot function [154, 52]:

$$W(t) = \sum_{n=-\infty}^{\infty} \frac{\cos(\phi_n) - \cos(\gamma^n t^* + \phi_n)}{\gamma^{n\alpha/2}} \tag{6.1}$$

Here, ϕ_n are random phases in the interval $[0, 2\pi[$, $\gamma > 1$ is an irrational number, t_{max} is the length of the desired time series. The parameter α denotes the degree of anomaly that appears in the particle means square displacement $MSD \sim t^{\alpha}$. In accordance with Reference [52], $\gamma = \sqrt{\pi}$ was chosen and the sum was restricted to the terms $n = -8, \ldots, 48$. The increments $\xi_i = W(t+1) - W(t)$ were chosen in such a way that the *MSD* for all α-values coincided at $t = 1$. By this approach, it was taken into account that in the realm of anomalous diffusion random motion in a viscoelastic fluid ($\alpha < 1$) will be hampered by elastic restoring forces with respect to a purely viscous fluid with normal diffusion ($\alpha = 1$). Thus, anomalous diffusion should be subordinated with respect to the normal diffusion.
To ensure that the particle number N was choosen high enough in the simulations to guarantee good statistics, $P(R)$ was determined in several test simulations with fixed α and t_{max} for particle numbers of $N = 100, 1000, 10000, 100000$. The resulting $P(R)$ was always observed to be the same smooth curve for $N = 1000, 10000, 100000$, while it showed strong fluctuations for $N = 100$. Therefore, a number of $N = 1000$ particles is suitable to yield good statistics in the simulations.

Conversion to SI units

The conversion of the simulation data to SI units was done as follows. The target radius a was used as unit of length in the performed simulations, i.e. defining the respective targets a) DNA operon (a = 2 nm) and b) Golgi membrane patch (a = 100 nm) automatically fixed the length scale. To gauge the time scale, it was assumed that subdiffusion may not occur for very small time periods at which a moving particle does not approach any obstacles [22] or, in the viscoelasticity picture, essentially experiences a thin layer of a homogenous, viscous fluid. A tracer may thus be regarded as being normal diffusive during time periods in which it moves less than its own radius. It was therefore assumed in the simulations that normal diffusion governed the tracer motion on time scales smaller than a single (sub)diffusion step in the simulations ($t < 1$), whereas anomalous diffusion appeared for $t > 1$. The crossover time $t = 1$, i.e. a single diffusive time step in the simulations, was translated to real time via the time τ a tracer needs to move about its own radius r. This time can be calculated with the Einstein-Stokes equation as:

$$\tau = \frac{r^2}{6D} = \frac{r^3 \pi \eta}{k_B T}. \tag{6.2}$$

Here, k_B is the Boltzmann constant, T denotes the absolute temperature, r gives the radius of the diffuser (e.g. a protein) and η is the viscosity of the fluid. With $\eta \approx 3 \cdot 10^3$ Pa s for the cytoplasm [155], a single simulation time step corresponded to a) $\tau = 0.02$ μs for LacI (r = 2 nm) and b) $\tau = 0.3$ μs for the coatomer complex (r = 10 nm).

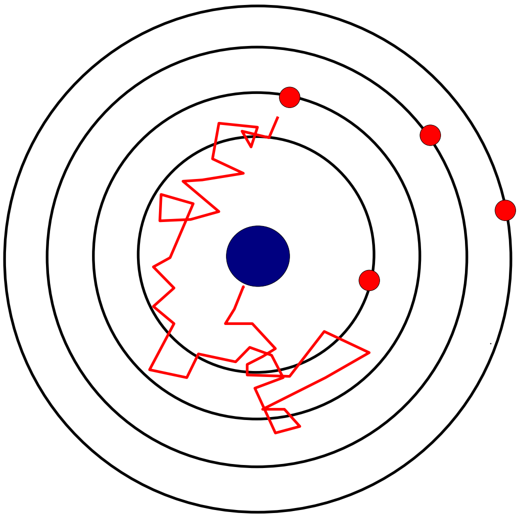

Figure 6.1: Schematic illustration of the diffuse-to-capture scenario. Particles (red) start from different initital distances R (rings) to the target in the center (blue). The fraction of particles approaching the target via normal diffusion and subdiffusion in the three dimensional space is recorded as $P(R)$.

6.3 Results

To determine the probability of a particle to reach a fixed binding target when moving either by normal diffusion or by subdiffusion, computer simulations of a diffuse-to-capture scenario were performed (see Figure 6.1 for illustration). A number of N non-interacting point particles were set on a sphere of the radius R. In the sphere center, a binding target of radius a was placed. Then the particles were allowed to move in three-dimensional space either by normal diffusion or by subdiffusion. When a particle hit the target, it was absorbed. After t_{max} timesteps, the fraction of absorbed particles was recorded as $P(R)$, which denotes the probability for a particle to reach the target in dependence on its starting distance R. This procedure was repeated for various R and for particles which moved by subdiffusion with different α.

In the simulations, the subdiffusive path of individual particles was calculated via the Weierstrass-Mandelbrot function (WMF) which yields a path of indiviual steps that are not statistically independent but correlated. The choice of a non-Markovian process seemed appropriate since the experimentally observed subdiffusion is a consequence of the viscoelasticity of the intracellular fluids (c.f. Section 5.4.2), i.e., the WMF here models the fluid's memory that is reflected in a nontrivial creep function [28]. In principle, one would have the alternative to model subdiffusion with a continuous time random walk (CTRW) that describes subdiffusion due to intermittent

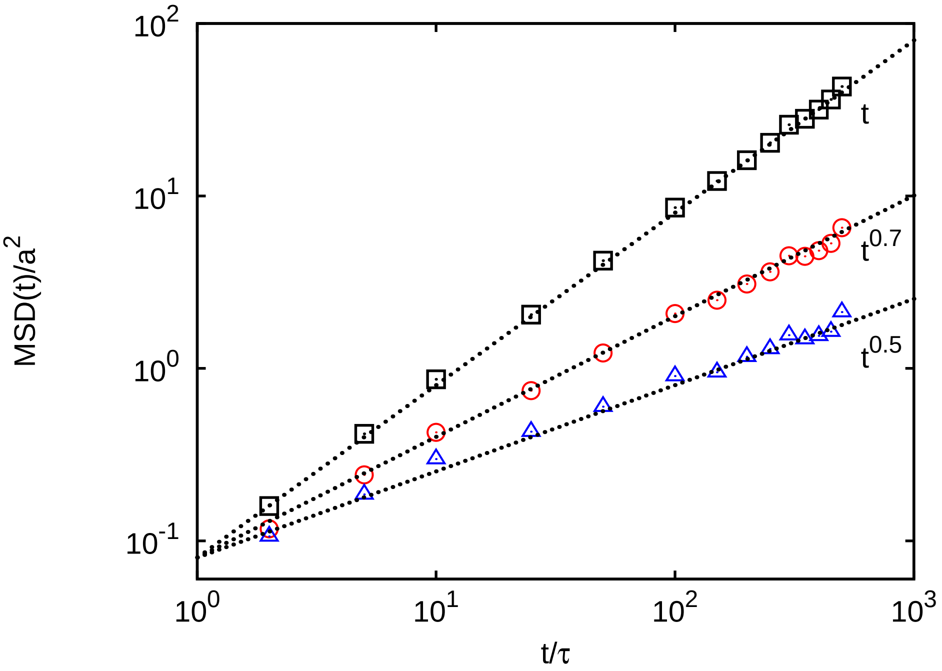

Figure 6.2: Mean square displacement of normal diffusion and subdiffusion as used in the simulations; subdiffusion is modeled as fractional Brownian motion using the Weierstrass-Mandelbrot function Eq. 6.1. The dashed lines highlight the scaling *MSD* $\sim t^{\alpha}$. The *MSD* of a single timestep *MSD(t=1)* was chosen equal for all simulations. The parameter a denotes the target radius, τ is the time a tracer needs to move about its own radius.

binding. In the CTRW, subdiffusion appears due to a power-law distribution of the waiting times of tracers between diffusive steps (c.f. Section 2.2.2). Bearing in mind, however, that subdiffusion of macromolecules in cells occurs due to obstruction by macromolecular crowding or the viscoelasticity of the intracellular environment, the Weierstrass-Mandelbrot function seems to be the more suitable model here.

The simulations of subdiffusion using the WMF yielded the expected scaling of the *MSD* $\sim t^{\alpha}$ (see Figure 6.2). To ensure a fair competition between the different random walks, the mean square displacement *MSD* for a single time step, i.e. *MSD(t=1)*, was chosen equal for all simulations (see also Figure 6.2). The target radius a was taken as the unit of length, and the time was measured in number of diffusion steps. The particle number N for each starting radius and each α was set to 1000, which is sufficient to yield a good statistics. For the sake of simplicity, it was neglected that subdiffusive processes typically are transient and change to a normal diffusive behaviour at asymptotically large times [150, 22]. A conversion to SI units will be done below in the context of biological examples.

For particles moving by normal diffusion the relation $P(R) \sim a/R$ was determined

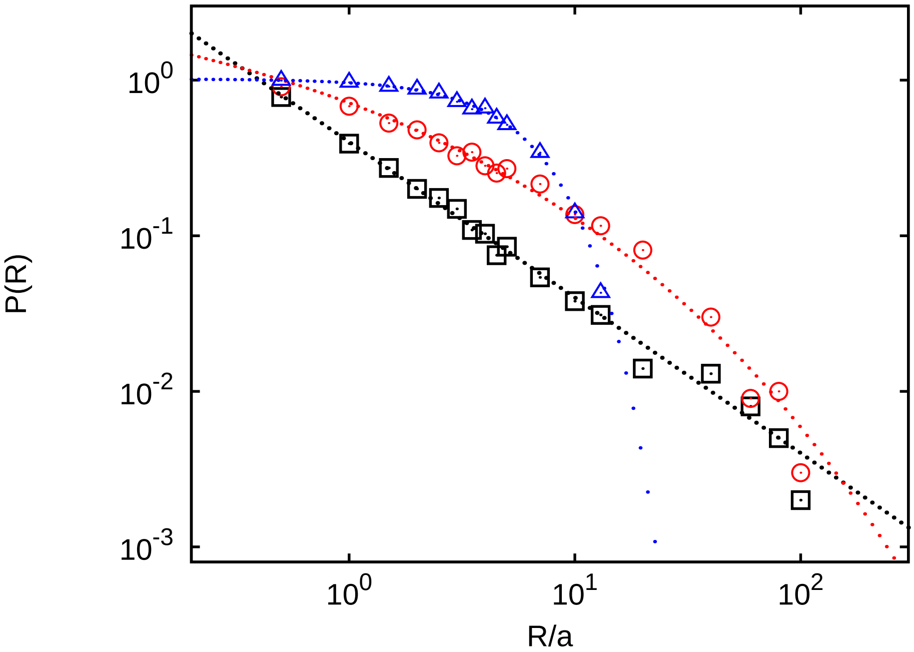

Figure 6.3: Probability $P(R)$ that particles reach a target when they start from an initial distance R and have a maximum search time $t_{max} = 2{\cdot}10^6\ \tau$. Normal diffusion yields $P(R) \sim 1/R$ (black squares). For subdiffusion of different degrees α, the probability is strongly increased ($\alpha = 0.7$: red circles; $\alpha = 0.5$: blue triangles). The parameter a denotes the target radius; dashed lines are a guide to the eyes.

as a result of the simulations, i.e. the probability to find the target decreased quite rapidly and became less than 1% when starting in a distance that exceeded the target's 10 fold radius (see Figure 6.3). This result is in agreement with the analytical solution of the diffuse-to-capture problem (see Equation 2.19), which confirms that the used simulation procedure is a suitable approach to examine the diffuse-to-capture scenario.

For particles moving by subdiffusion of different anomaly degrees $\alpha < 1$, the capturing probability $P(R)$ differed significantly from the normal diffusive case. For small starting radii R, the probability $P(R)$ was considerably larger than for normal diffusion by factors up to 10, whereas for large radii a sudden drop of $P(R)$ below the efficiency of normal diffusion could be observed (see Figure 6.3). Both, the increased $P(R)$ at small radii and the crossover radius R_i of the intersection of $P(R)$ for normal diffusion and subdiffusion were observed to depend on the anomaly degree α and on the maximum searching time t_{max}. For a fixed t_{max}, the probability $P(R)$ at small radii was seen to increase for smaller α, whereas the crossover radius R_i decreased (see Figure 6.3). For a fixed anomaly α, both $P(R)$ for small radii and R_i were seen to increase with a growing maximum search time t_{max} (see Figures 6.4 and 6.6).

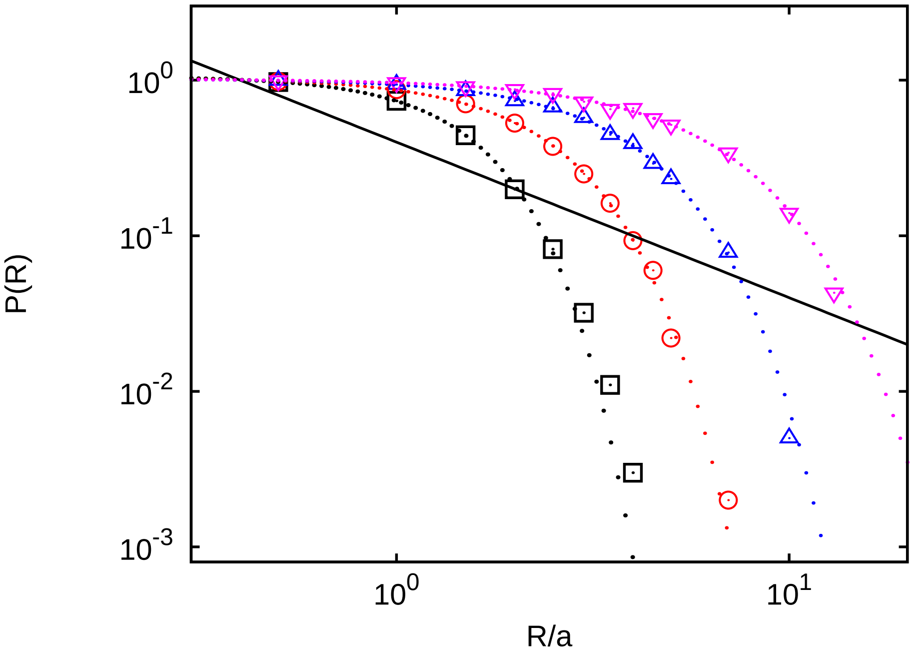

Figure 6.4: Probability $P(R)$ that subdiffusive particles ($\alpha = 0.5$) reach a target when they start from an initial distance R and have maximum search times t_{max} $= 2{\cdot}10^3$ (black squares), $2{\cdot}10^4$ (red circles), $2{\cdot}10^5$ (blue triangles), $2{\cdot}10^6$ (purple inverted triangles). The full line shows $P(R) \sim 1/R$ of normal diffusion; a denotes the target radius; dashed lines are a guide to the eyes. The range in R where $P(R)$ of subdiffusion is increased compared to normal diffusion enlarges with growing t_{max}.

The described dependency of $P(R)$ on α and t_{max} can be understood when the geometric properties of the underlying (subdiffusive) random walk are considered, i.e. the fractal dimension d_F. The fractal dimension of a random walk essentially determines how complete a diffuser explores the embedding space for infinitely large times. Normal Brownian motion and continuous time random walks have a fractal dimension $d_F = 2$. In these cases, a random walker explores a surface complete, but only visits a negligible subspace when it moves in a three-dimensional solution. In the case of subdiffusion due to viscoelasticity modeled via the WMF, however, a diffuser explores more than just a surface because the fractal dimension of its trace is given by $d_F = 2/\alpha$. Thus, for $\alpha < 1$, the sampled subspace is considerably larger than a surface ($d_F = 2$) and may even exceed the dimension of the three-dimensional bulk ($d_F = 3$).

In this context, the increased target finding probability $P(R)$ detected for subdiffusive particles starting close to the target becomes comprehensible. Subdiffusive tracers sample the three-dimensional space more dense than normal diffusive particles; therefore it can be expected that $P(R)$ increases with growing d_F (i.e. reduced α). Indeed, in the presented simulations, $P(R)$ for subdiffusion was increased com-

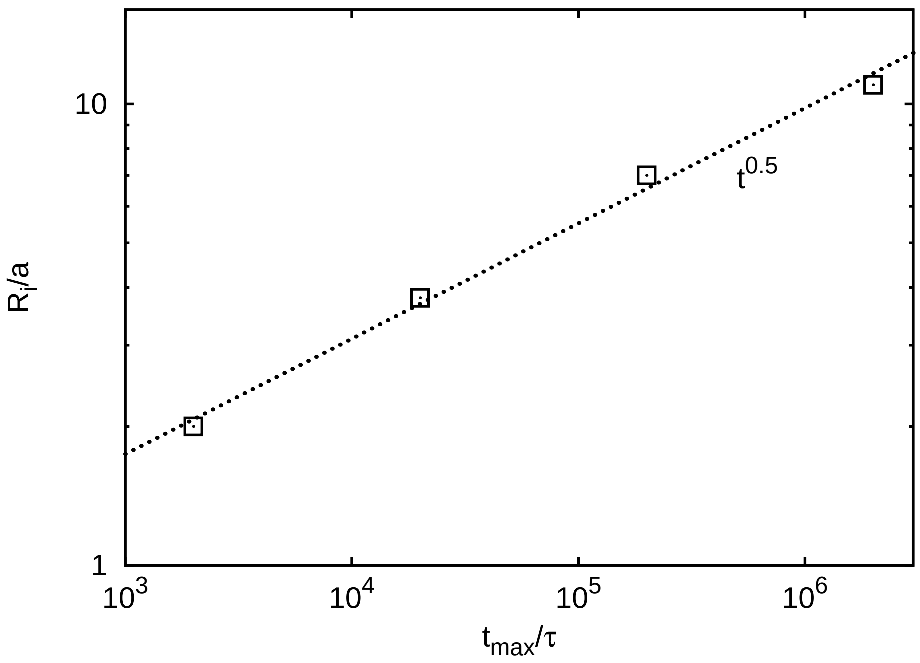

Figure 6.5: The crossover radius R_i increases with a growing maximum search time t_{max} according to $R_i \sim t^{\alpha/2}$, which is in accordance with the expectation $R_i \approx \sqrt{MSD(t_{max})}$, $MSD \sim t^{\alpha}$. Here, values for $\alpha = 0.5$ are shown; the parameter a denotes the target radius, τ is the time a tracer needs to move about its own radius.

pared to normal diffusion ($\alpha = 1$) maximally by a factor ≈ 6 for $\alpha = 0.7$ and by factor ≈ 10 for $\alpha = 0.5$. However, why is $P(R)$ increased only for a certain realm of R? It has to be considered that a decreasing α also has the effect of a weaker spatial spreading of tracers, as can be seen from the mean square displacement $MSD(t) \sim t^{\alpha}$. In particular, tracers travel in average a maximum excursion length $L_{max} = \sqrt{MSD(t_{max})}$, with the consequence that regions beyond L_{max} are rarely or never encountered; therefore it can be expected $P(R) \to 0$ for $R > L_{max}$. In agreement with this consideration, the presented simulations show the subdiffusive $P(R)$ to fall under the diffusive $P(R)$ at the crossover radius R_i and to drop then steeply towards 0. It can be expected $R_i \sim L_{max}$, in other words $R_i \sim a \cdot t_{max}^{\alpha/2}$ due to $MSD(t) \sim a^2 \cdot t^{\alpha}$. The numerical data indeed yields $R_i = c \cdot a \cdot t_{max}^{\alpha/2}$ (with some constant $c \approx 3$) for all α values, i.e. R_i increases exponentially with α and algebraically with t_{max} (see Figures 6.5 and 6.6). This means that particles starting beyond R_i, have typically no chance to reach the target by (sub)diffusion (except a few fast particles). For particles starting below R_i, however, subdiffusion is the most effective search strategy.

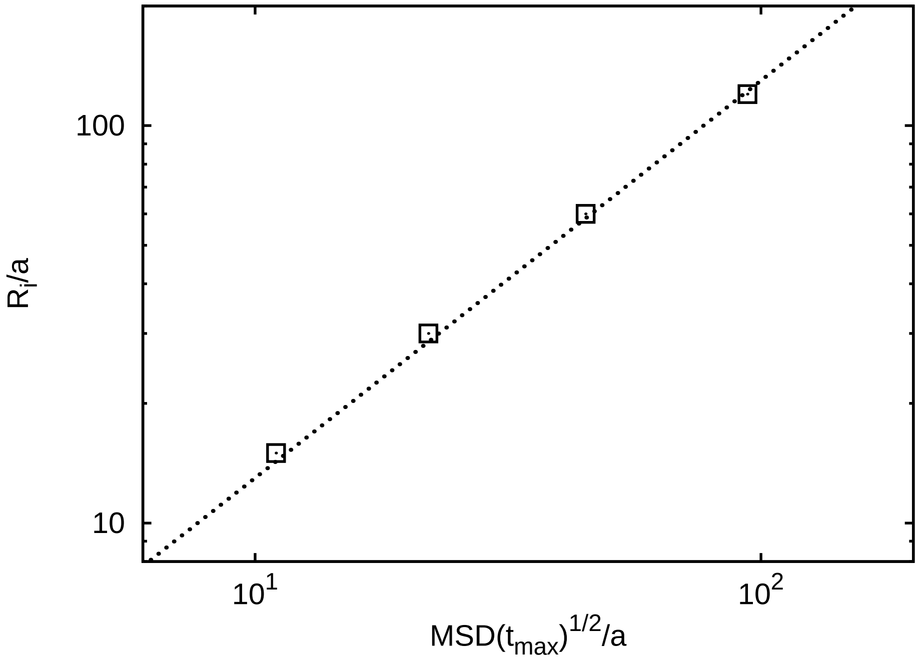

Figure 6.6: The crossover radius R_i increases linearly with a growing maximum excursion length $L_{max} = \sqrt{MSD(t_{max})}$, i.e. exponentially with α since $MSD \sim t^{\alpha}$. Here, values for $\alpha = 0.5$ are shown; the parameter a denotes the target radius.

Consequences for biological processes

Diffusion measurements in cells detected several proteins and protein-sized tracers to show subdiffusion with anomaly values $\alpha \approx 0.5$ - 0.8. It is therefore of high interest to relate the described effects of subdiffusion on target searching to a biological context.

At first, signal propagation and the formation of functional complexes (such as ribosomes) are considered. Both processes consist of a sequence of events, which are in signal propagation the cascade-like activation of consecutive subunits and in complex formation the assembly of multiple individual macromolecules. In both cases, the sequence of events can be described as a chain of states: $A_1 \rightarrow A_2 \rightarrow A_3 \rightarrow \ldots$, where the indices of the states A_i set the number of already activated sub-modules in the signaling cascade or the number of macromolecules which already joined the complex. The transition from one state to another happens with a probability p_i which basically depends on the (diffusion-mediated) encountering probability of two involved reaction partners. When a typical distance $R = 10\ a$ between the reaction partners is assumed and the number of states is restricted to $i \leq 3$, normal diffusion yields a very low probability $p = 0.043^3 \approx 6 \cdot 10^{-5}$ to approach the final state A_3. In contrast, subdiffusion with $\alpha = 0.5$ and a search time $t_{max} = 2 \cdot 10^6$ yields a roughly 100-fold higher probability $p = 0.133^3 \approx 2 \cdot 10^{-3}$ to reach A_3, i.e. signal propagation and complex formation become much more reliable. The effect of subdiffusion becomes even more significant when the number of intermediate states before the final state increases. With $i = 8$ for example, subdiffusion yields a 10^4-fold higher probability to reach the final state A_8.

Next, two examples from cell biology will be considered which may benefit from subdiffusion as a search strategy: a) the search of the transcription factor LacI for its DNA operon [156] and b) the binding of the coatomer complex by Golgi cisternae [157]. In both cases, tracers will be assumed to move subdiffusive with an anomaly $\alpha = 0.5$. The conversion from simulation units to SI units was done as described in the Methods Section 6.2.

For the LacI protein (radius $\approx$ 2 nm), the average time for approaching its DNA operon ($a = 2$ nm) can be estimated to be about 1 s via the tumbling frequency of the bacterium [158], which corresponds to $5 \cdot 10^7$ simulation steps. When this time is set as the relevant t_{max} of the problem, the crossover radius within which subdiffusion is more efficient than normal diffusion becomes $R_i = 500$ nm via $R_i = c \cdot a \cdot t_{max}^{\alpha/2}$. Given that only about 10 copies of the LacI protein are present in a bacterium with a volume 1 μm^3, the typical distance between a LacI protein and the operon of interest is 450 nm. This value is smaller than R_i, i.e. subdiffusion is the most advantageous strategy for LacI to search for the operon. If the nucleoplasm would be more diluted, with the consequence that proteins move by normal diffusion instead of subdiffusion, LacI may not bind the operon with a sufficient probability, thus compromising the cells gene expression pattern. Here, subdiffusion alone already provides an improved efficiency of finding the respective binding target, but of course also other mechanisms, e.g. the reduction of dimensionality and coupled diffusion [30] may contribute to an advanced search in the considered examples.

For coatomer (radius 5 nm), the typical search time for a membrane patch on Golgi cisternae ($a = 100$ nm) is given by the turnover time $t = 10$ s of its adaptor protein ARF-1 [155], which corresponds to $3.4 \cdot 10^7$ simulation time steps. Setting the turnover time as t_{max}, the crossover radius becomes $R_i \approx 13$ μm which corresponds approximately to the radius of the entire cell. The conclusion is that also here subdiffusion yields the most favorable searching strategy.

A strong anomaly (low α) not only is associated with an increasing probability of target finding but also with a long search time. An optimal searching efficiency with fractional Brownian motion might therefore be given at $\alpha = 2/3$ (i.e. $d_F = 3$). At this value, the three-dimensional space is fully explored while the subdiffusive spreading is not too slow. The α values measured for protein diffusion in cells are about this optimal α, i.e. intracellular fluids interestingly seem to have just the right amount of crowding to guarantee an optimal searching efficiency of tracers.

Part II

Diffusion of membrane inclusions

Chapter 7

Studying membranes via Dissipative Particle Dynamics (DPD) simulations

In this chapter first a general introduction to the structure and functionality of biological membranes is given (Section 7.1). The problem of the size-dependent diffusion of membrane constituents is discussed, based on available theoretical and experimental studies (Section 7.2). Dissipative particle dynamics is introduced as a class of computer simulations adequate to study soft-matter systems like membranes (Section 7.3).

7.1 An introduction to membranes

Biological membranes are entities of central importance for all living organisms. They enclose entire cells and surround compartments within cells, like organelles or vesicles. All biological membranes have a common gross structure. Each membrane is a film of lipid molecules which are arranged as a continuous bilayer with a typical thickness of $\approx$ 5 nm [159]. Lipids are molecules consisting of a polar headgroup and two hydrocarbon tails. They have an approximately cylindrical shape and are amphiphilic, i.e. their headgroup is hydrophilic and their fatty acid tails are hydrophobic. Due to their amphiphilic nature, lipids form spontaneously membranes or micelles when they are dissolved in water.

In membranes, lipids are ordered in such a way that the hydrophilic headgroups are exposed at both bilayer surfaces to the surrounding water whereas the hydrophilic tails are buried in the core of the bilayer and thus are protected from contact with water (see Figure 7.1 for a schematic illustration). The forces which make lipids form membranes are mainly of entropical origin. The hydrophobic groups of lipids have disruptive effects on the hydrogen-bond network of the water

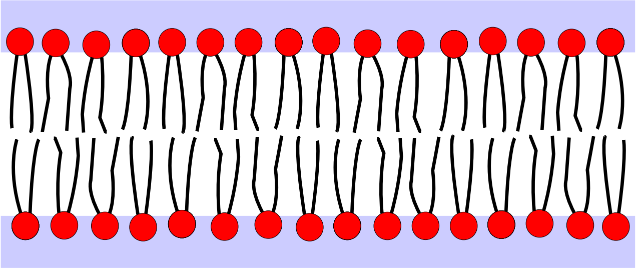

Figure 7.1: Schematic illustration of a lipid bilayer membrane (cross section). Lipids expose their polar headgroups (red) to the surrounding water, while the hydrocarbon tails (black) are buried in the membrane core.

surrounding, and it is entropically favourable for the system to minimise the disruption by seperating the lipid tails from water [34]. To a certain extent, also non-covalent attractive interactions between the lipid tails may contribute to preserve the membrane integrity, e.g. Van-der-Waals forces or hydrogen bonds [160].

Biological membranes are in principle impermeable to molecules soluble in water, due to their structure as lipid bilayers with a hydrophobic core. Membranes represent thus an ideal material to enclose compartments like cells, cellular organelles or vesicles which exist in an aqueous environment and contain aqueous fluids of a well defined composition. The lipid species which are present in biological membranes are manifold. A membrane's specific lipid composition determines its properties like thickness and stability. Generally, the different lipid species in biological membranes can be subdivided into the main classes of phospholipids, sphingolipids and sterol lipids (e.g. cholesterol).

Membranes are not just passive shells to the compartments which they surround, but they have also many active functions, for example molecule translocation into/ out of enclosed compartments, enzymatic catalysis, signaling or local formation of vesicles. The carriers of these active functions are proteins which are embedded in the membrane. Similarly to lipids, membrane proteins consist of hydrophilic and hydrophobic parts which specify how they are associated with a membrane. So-called transmembrane proteins have a hydrophobic top and bottom and a hydrophilic core; they are inserted into the lipid bilayer and span its entire thickness. Other protein species are inserted only in one half of the bilayer or are attached to the membrane surface by being anchored with a hydrophobic finger.

The number of membrane protein species in cells is very large due to their multitude of functions. The importance of membrane proteins for the proper functioning of membranes and of entire cells is emphasised by the fact that 30% of a cell's genome codes for transmembrane proteins [161].

Membrane bilayers are dynamic structures which are fluid in two dimensions due to their non-convalent design that is based on entropic interactions and on weak non-covalent forces. This means that lipids and membrane proteins can in principle diffuse freely in the membrane plane. A lipid in a membrane for example has typically a two-dimensional diffusion coefficient about $D \approx 4\ \mu m/s$ [162] and a rotational diffusion coefficient $D_{rot} \approx 10 \cdot 2\ \pi/\mu s$ [163].

Early membrane models proposed membranes to be unstructered two-dimensional fluids where lipids could be regarded as a randomly distributed solvent and proteins were low in concentration compared to lipids [164]. In the current view, however, a more structured picture of cellular membranes is assumed. Several lines of evidence have been given that proteins and lipids form domains ('rafts'), for example functional protein complexes, separated areas of different lipid composition and regions of functional specialization [165, 166]. Such segregated regions in membranes were shown to differ for example in thickness and fluidity [167, 168]. The size of domain-like entities in biomembranes has been reported to cover a wide range, from a few nanometers to some 100 nm [169]. Also in contrast to earlier points of view, protein occupancy in membranes was detected to be very high, in that membrane proteins make out about 50 % of the membrane mass in a cell [34].

7.2 The mobility of membrane inclusions

7.2.1 Theoretical studies on the diffusion of membrane inclusions

The two-dimensional diffusive mobility of membrane constituents is often crucial for their functionality, since most biological processes rely on the mutual finding of reaction or binding partners via diffusion. Functional membrane inclusions which move by diffusion include single lipids and proteins (e.g. receptors or enzymes) as well as large raft-like domains (e.g. assemblies of coat proteins which induce vesicle formation in the ER [170]).

While in three dimensions the lateral diffusion coefficient of a spherical particle in a viscous fluid is described by the Einstein-Stokes relation, a comparable expression of general validity is lacking for two-dimensional fluids. Notwithstanding, it is highly desirable to have such a equation, since it allows not only to conclude from a diffuser's radius R (which may be known from cristallography studies) on its mobility, but permits also to determine parameters like membrane viscosity or the diffuser size from measured diffusion coefficients. Furthermore, events like clustering can be detected from mobility measurements which are related to a change in diffuser size.

Due to pure geometrical considerations it seems to be appropriate to separate two regimes of diffusion in membranes: the first for inclusions which are comparable in size to the solvent lipid molecules and the second for inclusions which are large compared to the lipid solvent [171, 172].

Free area model

In the first regime, when solvent and inclusion have similar sizes, the inclusion's diffusion is influenced by the appearence of solvent molecules as discrete elements. Tracers show a lattice movement, i.e. they diffuse by jumping between discrete adjacent 'holes' in the solvent. A diffusive jump takes place when a hole with a free area a_f larger than a critical area a^* opens up next to the tracer. Free-area models [173, 174] predict in this context lateral diffusion coeffiecients $D \sim e^{-a^*/a_f}$, which are in a fair agreement with measurements for single lipids [162] and for lipid-sized proteins [175].

The Saffman–Delbrück relation

In the second regime, where diffusing entities are large compared to lipids, the solvent bilayer can be regarded as a continuum. For this case, a membrane inclusion's diffusion coefficient can be derived from hydrodynamic theory, analogously to the Einstein-Stokes equation.

Starting point for the calculation of a diffusion coefficient is typically the Einstein relation, which connects the lateral/ rotational diffusion coefficients $D_{lat/rot}$ of a particle to the system temperature T and to the particle's translational/rotational mobility $\mu_{lat/rot}$:

$$D_{lat/rot} = \frac{k_B T}{\mu_{lat/rot}}. \tag{7.1}$$

Here, k_B is the Boltzmann constant, while T denotes the absolute temperature. The lateral/rotational mobilities μ_{lat} and μ_{rot} are defined as the velocity/angular velocity produced by a steady unit force/torque.

For the three-dimensional case of a hard spherical particle with radius R embedded in a fluid of viscosity η, the mobilities can be calculated from standard hydrodynamics for laminar flows. This yields the Einstein-Stokes relation for translational diffusion and the Einstein-Stokes-Debye relation for rotational diffusion (using no-slip boundary conditions):

$$D_{lat} = \frac{k_B T}{6\pi\eta R}, \quad D_{rot} = \frac{k_B T}{8\pi\eta R^3}. \tag{7.2}$$

An analogous expression for the two-dimensional diffusion coefficient of an inclusion in a membrane was derived by Saffman and Delbrück in 1975 [2]. Here, the membrane was assumed to be an infinite plane sheet of an incompressible viscous liquid with thickness h and viscosity η_m. The membrane inclusion was considered as a hard cylinder of radius R with the axis perpendicular to the membrane.
The rotational diffusion coefficient D_{rot} of the cylinder about the axis perpendicular to the membrane was calculated with standard hydrodynamics using no-slip boundary conditions to be [2]:

$$D_{rot} = \frac{k_B T}{4\pi \eta_m R^2 h} \tag{7.3}$$

To derive D_{lat}, also the external fluid above and below the membrane had to be taken into account, because a calculation of a cylinder's translational movement in just two dimensions via the low-Reynolds number Navier-Stokes equations is not possible ('Stokes-Paradox'). The external fluid was in the model of [2] allowed to be dragged into motion by the flow of the membrane sheet and by the motion of the cylinder. It further was assumed that the external fluid added a surface traction on the sheet. A calculation with perturbation techniques yielded:

$$D_{lat} = \frac{k_B T}{4\pi \eta_m h} \cdot (\log\left(\frac{\eta_m h}{\eta_c R}\right) - \gamma) \tag{7.4}$$

where η_c is the viscosity of the external fluid and $\gamma = 0.5772$ is Euler's constant.
Formula 7.4 is commonly denominated the Saffman-Delbrück relation. It is characterised by its logarithmic scaling $\sim \log(\frac{1}{R})$, i.e. it predicts only a weak dependence of D_{lat} on the inclusion radius R.

Extension of the Saffman-Delbrück relation
Due to its logarithmic scaling, the Saffman-Delbrück relation predicts negative diffusion coefficients when $\eta_m h/(\eta_c R) < 1$, i.e. for membrane inclusion radii beyond a critical radius

$$R_c = \frac{\eta_m h}{\eta_c}. \tag{7.5}$$

R_c depends on the ratio of the viscosities, i.e. relation Eq. 7.4 breaks down when the influence of the external fluid viscosity η_c prevails the influence of the membrane viscosity on the cylinder diffusion.
To account for this, Hughes, Pailthorpe and White [176] performed an extended numerical calculation of the model of Saffman and Delbrück and derived a complex expression with an effective scaling:

$$D_{lat} \sim \frac{1}{R} \text{ for } R \gg R_c \tag{7.6}$$

According to relation 7.6, D decreases for large inclusions rather strongly with growing R, which deviates from the weak decrease of D for small inclusion as predicted in the Saffman-Delbrück relation.

7.2.2 Experimental studies on the diffusion of membrane inclusions

The size-dependence of the diffusion of membrane inclusions has been examined in several studies. Transmembrane protein radii as determined from diffusion coefficients via the Saffman-Delbrück relation were shown to agree with crystallography structural data [177, 178]. Further, diffusion coefficients of various membrane proteins and of small membrane protein oligomers were observed to depend only weakly on their radii, in accordance with the Saffman-Delbrück relation [179, 175]. While the mentioned studies support the Saffman-Delbrück relation for inclusions with radii between 0.5 and 5 nm, a more recent examination challenges the predictions [180]. Here, the diffusion coeffiecients of synthetic model peptides with known radii (0.55 - 1.8 nm) were measured and found to deviate from the D(R)-dependence stated in the Saffman-Delbrück relation. The authors of [180] proposed as an alternative an empirical expression $D \sim \frac{1}{\eta_m h R}$.

7.3 Dissipative Particle Dynamics

7.3.1 Investigating membranes with particle based computer simulations

Computer simulations represent a versatile approach to investigate the behaviour of membranes. The simulation technique which allows the most detailed insight is molecular dynamics (MD). MD represents an atomistic model based on realistic microscopic interactions. Here, every atom of a system is considered and all interactions between the atoms are taken into account, i.e. bonds, angles and dihedral angles within indiviual molecules and van-der-Waals forces, hydrogen bonds and electrostatic forces between molecules. Due to their exactness in detail, MD simulations are very demanding in computational power and calculation time. They are therefore restricted in their applicability to problems which happen on lengthscales of nanometers and timescales of nanoseconds. Nevertheless, MD simulations were already succesfully applied to study simple model membranes [181, 182, 183] as well as more complex systems which included for example membrane proteins [184] or DNA-lipid-complexes [185].

To examine more global quantities on mesoscopic lengthscales up to micrometer and timescales up to microseconds, so-called coarse-grained simulation models were developed in which atomic details are neglected. Coarse-graining means that functional atom groups in a molecule are summarised to clusters which interact by effective forces. Such models have, for example, been designed to study membrane systems [186] or DNA molecules [187]. On a certain low level, coarse-graining exists already in MD because the quantumchemical nature of the atomic interaction is neglected, assuming it is not important for the observed quantities.

7.3.2 Dissipative Particle Dynamics

A class of coarse-grained MD simulations that has found a broad utilisation in the investigation of soft matter and complex fluids is Dissipative Particle Dynamics (DPD). The DPD method was initially introduced in 1992 by Hoogerbrugge and Koelman for the simulation of hydrodynamic phenomena [188]. In DPD, a system of interacting soft beads is considered, each representing a volume of fluid that contains a functional group of atoms. A bead is large on the molecular scale, but still small from a macroscopic point of view. Beads move according to Newtons equations. They interact via effective forces that are chosen in a way that they reproduce the hydrodynamic behaviour of the fluid without Reference of the molecular structure. DPD fluids satisfy the Navier-Stokes equations [188].

Today, commonly a formulation of the DPD algorithm is used which was established by Espanol and Warren [189]. They modified the original DPD algorithm by introducing a fluctuation-dissipation theorem to ensure that the statistical mechanics of

the bead system corresponds to the Gibbs canonical ensemble. In the formulation of Espanol and Warren, DPD beads interact via three forces: a repulsive conservative force $\vec{F}^C$, a dissipative force $\vec{F}^D$ and a random force $\vec{F}^R$. The forces are pairwise additive, conserve momentum, have no hard core and are short-ranged, with the range of the forces defining the size of the beads. Extended objects in DPD, e.g. polymers, are formed by connecting particles via Hookean springs, and the stiffness of chain-like molecules is regulated via a bending potential. In available studies, DPD was applied for example to study colloids [190], vesicles [191] or membranes [192, 193, 194].
Compared to MD simulations, DPD allows access to larger lengthscales and timescales due to two major reasons. Firstly, the reduction of atomic detail in DPD saves computational time; for example 1 lipid in MD typically consists from about 100 atoms, whereas in DPD it is composed from less than ten beads. Secondly, the soft core potentials used in DPD permit a stable integration of the equations of motion with much larger time steps dt than the hard core potentials in MD (typically Lennart-Jones) do.

7.3.2.1 The DPD formalism

Equations of motion
In DPD, a set of interacting particles is considered, the temporal evolution of which is determined by Newton's equation of motion:

$$\frac{d\vec{r}_i}{dt} = \vec{v}_i \tag{7.7}$$

$$\frac{d\vec{v}_i}{dt} = \vec{F}_i \tag{7.8}$$

Here, $\vec{r}_i$ denotes the center of mass position of a particle, $\vec{v}_i$ its velocity, $\vec{F}_i$ the total force which acts on it. The mass m of each bead is set to unity.

Forces
The particles interact via three forces, all being pairwise additive:

$$\vec{F}_i = \sum_{i \neq j} (\vec{F}_{ij}^C + \vec{F}_{ij}^D + \vec{F}_{ij}^R) \tag{7.9}$$

Here, the sum includes all particles j which are within a certain cutoff radius r_0 around the particle i. The radius r_0 specifies the range of interaction between two beads; r_0 as the only length scale in the system is used as unit length, i.e. $r_0 = 1$.

$\vec{F}_{ij}^D$ denotes the dissipative or drag force. F^D is proportional to the relative velocity of a interacting bead pair. It arises due to unobserved internal degrees of freedom of the coarse-grained particles and destroys the relative momentum between two beads.

$$\vec{F}_{ij}^{D} = -\eta w^{D}(\vec{r}_{ij})(\vec{e}_{ij} \cdot \vec{v}_{ij}) \cdot \vec{e}_{ij} \tag{7.10}$$

where $\vec{r}_{ij} = \vec{r}_i - \vec{r}_j$, $\vec{r}_{ij} = |\vec{r}_{ij}|$, $\vec{e}_{ij} = \vec{r}_{ij}/|\vec{r}_{ij}|$, $\vec{v}_{ij} = \vec{v}_i - \vec{v}_j$. In DPD simulations, typically periodic boundary conditions are chosen, which must be accounted for in the calculation of $\vec{r}_{ij}$. The parameter η denotes the amplitude of the drag force; w^D is a weight function dependent on the distance r_{ij} of two beads.

$\vec{F}_{ij}^{R}$ is the random force. It occurs due to the coupling of the beads to the local temperature of their fluid environment and creates a relative momentum between two beads.

$$\vec{F}_{ij}^{R} = \sigma w^{R}(\vec{r}_{ij})\xi_{ij}(t)\vec{e}_{ij} \tag{7.11}$$

Here, the parameter σ is the amplitude $\vec{F}^R$; w^R is a weight functions. $\xi_{ij}(t)$ is a randomly fluctuating variable with Gaussian statistics. The mean value of ξ is zero: $\langle \xi_{ij}(0) \rangle = 0$, and the ξ variables are uncorrelated: $\langle \xi_{ij}(t) \cdot \xi_{kl}(t') \rangle = (\delta_{ik}\delta_{jl} + \delta_{il}\delta_{jk})\delta(t - t')$.

The forces $\vec{F}^D$ and $\vec{F}^R$ are related by the fluctuation-dissipation theorem. This connection relates σ and γ via k_BT and connects the two weight functions [189]. One of these functions can be choosen arbitrarily and defines thus the other one.

$$\sigma^2 = 2\gamma k_B T \tag{7.12}$$

$$w^D(r) = w^R(r)^2 \tag{7.13}$$

We choose according to Reference [195]: $\sigma = 3$, $\gamma = 4.5$,

$$w^D(r) = \begin{cases} (1-r)^2 & \text{for r} < r_0 \\ 0 & \text{for r} \geq r_0. \end{cases} \tag{7.14}$$

The interrelation of $\vec{F}^D$ and $\vec{F}^R$ ensures that the DPD system has an equilibrium distribution corresponding to the Gibbs-Boltzmann distribution. This is highly desirable, because then all standard thermodynamic relations (e.g. for the pressure) can be transferred to DPD [196].

The combined effect of $\vec{F}^D$ and $\vec{F}^C$ is that of a thermostat which conserves the linear and angular momentum of the total system and hence gives the correct thermodynamics at sufficient time-and lengthscales.

$\vec{F}_{ij}^C$ is the conservative repulsive force:

$$\vec{F}_{ij}^C = a_{ij} w^R(r_{ij}) \vec{e}_{ij} \tag{7.15}$$

Here, the constant $a_{ij} > 0$ specifies the strength of mutual repulsion between the two beads i and j. The weighting function $w^R(r_{ij})$ is the same as in the random force. Like $\vec{F}^D$ and $\vec{F}^R$, $\vec{F}^C$ conserves linear and angular momentum. The three DPD forces all are pairwise, therefore $\vec{F}_{ij} = -\vec{F}_{ji}$.

When a_{ij} is the same for all beads, the system represents just one fluid phase. With different bead species of various a_{ij}, there are multiple fluid phases in the system. When $a_{ij} = 25 k_B T$ is chosen, the DPD liquid has for a bead density $\rho = 3/r_0^3$ the same fluctuations as water. The fluctuations are measured in terms of the dimensionless compressibility κ^{-1} of the system, which is calculated via:

$$\kappa^{-1} = \frac{1}{k_B T} (\frac{\partial p}{\partial n})_T \tag{7.16}$$

where p is the pressure and n is the number density of molecules. For water at room temperature, $\kappa^{-1} = 15.9835$ [196]. With this calibration, a water bead in DPD corresponds to three water molecules 'in nature'.

Membranes

The ability of DPD to simulate self-assembled lipid bilayers was demonstrated in a paper by Shillcock [192]. In the membrane model proposed there, 3 types of beads are used to simulate membrane systems: water beads, hydrophilic and hydrophobic beads. The repulsion between water and hydrophilic beads is rather weak, whereas hydrophobic beads and water repel each other strongly. Lipids are constructed by connecting 1 hydrophilic and 6 hydrophobic particles via Hookean springs to a chain. The harmonic pair potential between two adjacent beads in the chain is given by:

$$U_{harm}(i, i+1) = \frac{1}{2} k_{harm} (|\vec{r}_{i,i+1}| - l_0)^2. \tag{7.17}$$

The indices i, $i+1$ represent here adjacent beads. The spring constant k_{harm} and the unstretched bond length l_0 are chosen such that the average bond length is fixed to the desired value. The stiffness of a lipid chain is modelled by a three-body potential acting between adjacent bead triples:

$$U_{stiff}(i-1, i, i+1) = k_{stiff}(1 - \cos(\phi - \phi_0)) \tag{7.18}$$

The indices $i-1$, i, $i+1$ again represent adjacent beads in the lipid. The angle ϕ is defined as $\phi = \frac{\vec{r}_{i-1,i}\cdot\vec{r}_{i,i+1}}{|\vec{r}_{i-1,i}|\cdot|\vec{r}_{i,i+1}|}$. ϕ_0 specifies the preferred angle between two bonds.

Due to their amphiphilic nature, DPD lipids self-assemble when they are initially distributed randomly in water. The structures which are formed depend on the lipid density in the system and can be micelles, single bilayers or vesicles [192]. The self-assembly ensures that DPD membranes are stable structures. Membrane properties like the lateral stress profile, area stretch modulus or bending rigidity as determined for DPD bilayers are comparable to experimental values measured in typical lipid bilayers [192].

In the DPD literature, various membrane models have been introduced which are based on the Shillcock model, but modify for example the chain length [193], the number of head groups/ tail groups or the number of hydrophobic tails (one/ two) [197, 194]. The choice of the model determines the values of the parameters k_{harm}, l_0, k_{stiff} and a_{ij}.

In the study presented here, the lipid model of Laradji [193, 198] was used, which is a coarse-grained version of the Shillcock model (i.e. a lipid here consists from one hydrophilic headgroup (H) and only three hydrophobic tailgroups (T)), allowing thus the investigation of comparatively large systems. The bead density in the system here is chosen as $\rho = 3/r_0^3$, the lipid density in the membrane has to be $\rho_{lipid} = 2.5$. The interaction constants between the beads are: $a_{WW} = a_{HH} = a_{TT} = a_{WH} = a_{HW} = 25k_BT$, $a_{WT} = a_{TW} = a_{HT} = a_{TH} = 200k_BT$, $k_{harm} = 100k_BT$, $k_{stiff} = 20k_BT, l_0 = 0.45r_0$. The letter W in the index of the repulsion constants denotes the 'water' bead species. In the original version of the Laradji model, the bending potential of the Shillcock model is lacking. It was introduced here using the parameter setting of Shillcock.

Integration

To advance the set of particle positions and velocities, Newtons equation of motion need to be integrated. There exist several integration schemes suitable for DPD [195], but typically the DPD velocity-Verlet (DPD-VV) algorithm is used [199, 195]:

1. Calculate forces: $\vec{F}_i^C = \sum_{i\neq j}\vec{F}_{ij}^C$, $\vec{F}_i^D = \sum_{i\neq j}\vec{F}_{ij}^D$, $\vec{F}_i^R = \sum_{i\neq j}\vec{F}_{ij}^R$

2. Calculate new velocities $\vec{v}_i$:

$$\vec{v}_i \leftarrow \vec{v}_i + \frac{1}{2m}(\vec{F}_i^C dt + \vec{F}_i^D dt + \vec{F}_i^R\sqrt{dt}) \tag{7.19}$$

3. Calculate new positions $\vec{r}_i$:

$$\vec{r}_i \leftarrow \vec{r}_i + \vec{v}_i dt \tag{7.20}$$

4. Calculate $\vec{F}_i^D$

5. Calculate new velocities $\vec{v}_i$:

$$\vec{v}_i \leftarrow \vec{v}_i + \frac{1}{2m}\vec{F}_i^D dt \tag{7.21}$$

6. Calculate new positions $\vec{r}_i$:

$$\vec{r}_i \leftarrow \vec{r}_i + \vec{v}_i dt \tag{7.22}$$

The DPD-VV algorithm is derived from the standard velocity Verlet (VV) scheme which is typically used in molecular dynamics. The VV scheme allows a more stable integration of the equations of motion than the common Euler scheme does. In particular the integration time step dt in the DPD-VV can be choosen by a factor of ≈ 50 larger than in an Euler integrator [196]. In DPD-VV, standard VV was extended by the steps 4.) - 6.) which includes an additional update of $\vec{F}_i^D$ to account for the mutual dependence of $\vec{v}_i$ and $\vec{F}_i^D$ which can be problematical in the integration.

In the choice of the integration time step dt one has to balance between a fast simulation and the requirement to keep the system faithfully reproduce the real dynamics. In Reference [196], it is recommended to choose $dt < 0.05$ to avoid errors of T which are larger than 2 %.

In the integration of the random force $\vec{F}_{ij}^R$, the factor $\sqrt{dt}$ occurs instead of dt, as can be derived from the underlying stochastic differential equations [189].

To save processing time, the random numbers ξ_{ij} can be taken from a uniform distribution instead of a Gaussian distribution. This is allowed since the number of ξ_{ij} used in a simulation is very large and their distribution approximates a Gaussian distribution according to the central limit theorem. Reference [196] demonstrated in this context that there is no statistical difference in DPD simulations when using Gaussian and uniform random numbers.

Barostat

To perform DPD simulations at a constant pressure and a constant surface tension - for example to ensure that a membrane is tensionless - a barostat is used to equilibrate the system. A barostat generally regulates the pressure in a system by relaxing or contracting the simulation box according to the difference of the instantaneous pressure from the selected target pressure.

A Galilean-invariant and momentum-conserving DPD barostat was introduced by Jakobsen [200]. It works analogously to the Langevin piston barostat which was developed for MD simulations [201]. The DPD barostat is impelemented

by introducing three new degrees of freedom to the system, which correspond to the volume of the simulation box and effectively serve as a piston. They are parametrised by a coordinate $\vec{\epsilon}$, the components of which are the logarithms of the box lengths L_x, L_y, L_z in x, y, z - direction. The piston has further a mass W and a velocity $\vec{v}_\epsilon$.
The motion of the piston degree of freedom is described by a Langevin equation. This allows a partial damping and avoids unphysical oscillations of the box volume which are observed in alternative barostat methods without damping [200].
The piston motion is governed by a force F_ϵ which includes contributions from the difference of the instantaneous pressure to the target pressure, from the momenta of the beads in the box, from a dissipation force and from a random force.
The positions of the beads in the box are adjusted to the new volume after every barostat step such that they keep their relative position to the box corners. Also the influence of the piston velocity on the bead velocities is considered.
For integration, the DPD-velocity Verlet integrator is extended to include the piston motion. The resulting equations are complicated because the new particle velocities depend on the new pistion coordinates $\vec{v}_\epsilon$ and vice versa. To account for this, an iterative procedure for the calculation of $\vec{v}_\epsilon$ and the $\vec{v}_i$ has to be used.
The combination of the DPD-VV integrator and the iterative procedure for the barostat lead to the following integration scheme for equilibration with the barostat:

1. $\vec{v''}_\epsilon \leftarrow \vec{v'}_\epsilon,\ \vec{v'}_\epsilon \leftarrow \vec{v}_\epsilon,\ \vec{\epsilon'} \leftarrow \vec{\epsilon}$

2. $\vec{v}_i \leftarrow \vec{v}_i + \frac{1}{2m_i}(\vec{F}_i^C + \vec{F}_i^D - 2v_\epsilon^j \vec{v}_i)dt + \vec{F}_i^R \sqrt{dt})$

3. $\vec{v}_\epsilon \leftarrow \vec{v}_\epsilon + \frac{1}{2W}(dV(P - P_0) + \frac{d}{N_f}\sum_i \frac{p_i^2}{m_i} - \gamma_p \frac{\vec{v}_\epsilon}{W})dt + \frac{\sigma_p \xi_p}{2W}\sqrt{dt}$

4. $\epsilon \leftarrow \vec{\epsilon} + \vec{v}_\epsilon dt$

5. $r_i^j \leftarrow e^{\epsilon_j - \epsilon'_j}(r_i^j + v_i^j dt)$

Update the simulation box size: $L_j = L_j e^{\epsilon_j - \epsilon'_j}$, j: x, y, z - coordinate
Update the simulation box volume: $V = L_x \cdot L_y \cdot L_z$
Calculate the DPD forces $\vec{F}_i^C$, $\vec{F}_i^D$, $\vec{F}_i^R$
Calculate the pressure P

6. $\tilde{\vec{v}}_i \leftarrow \vec{v}_i,\ \tilde{\vec{v}}_\epsilon \leftarrow \vec{v}_\epsilon$

7. $\vec{v}_\epsilon \leftarrow \vec{v''}_\epsilon + \frac{2}{W}(dV(P - P_0) + \frac{d}{N_f}\sum_i \frac{p_i^2}{m_i} - \gamma_p \frac{\vec{v}_\epsilon}{W})dt + \frac{2\sigma_p \xi_p}{W}\sqrt{dt}$

8.a) $v_i^j \leftarrow \{e^{\epsilon^j - \epsilon'^j}\tilde{v}_i^j + \frac{1}{2m_i}(F_i^{Cj}dt + F_i^{Dj}dt + F_i^{Rj}\sqrt{dt})\}/\{1 + v_\epsilon^j dt\}$

8.b) $\vec{v}_\epsilon \leftarrow \tilde{\vec{v}}_\epsilon + \frac{1}{2W}(dV(P - P_0) + \frac{d}{N_f}\sum_i \frac{p_i^2}{m_i} - \gamma_p \frac{\vec{v}_\epsilon}{W}dt) + \frac{\sigma_p \xi_p}{2W}\sqrt{dt}$

Here, indices j denote the x-, y-, z-coordinates. The steps 8.a) and 8.b) are iterated to convergence, which happens within 5 to 10 iterations. The barostat mass is chosen as $W = (N_f + d)k_BT\tau_p^2$. The parameter $N_f = dN - d$ denotes the number of degrees of freedom of the system. d is the dimension, N the number of beads in the box. τ_p is the characteristic time of the barostat and has to be chosen similar to the smallest time scales of particle motion. σ_p is the strength of dissipation of the piston coordinate, ξ_p is the strength of fluctuation; both are related by a fluctuation-dissipation theorem as $\sigma_p^2 = 2\gamma_p W k_B T$.

The pressure P in the box is a tensor and defined as:

$$P^{jk} = \frac{1}{V}(\sum_i \frac{v_i^j v_i^k}{m_i} + \sum_i F_i^{Cj} r_i^k) \tag{7.23}$$

with j, k being the x- ,y- ,z-coordinates. P_0 is the target pressure in the box. For equilibration with the barostat, the parameters were chosen here in agreement with [200] set to: $d = 3$, $P_0 = 23.649 k_BT/r_0^3$, $\tau_p = 2$, $\gamma_p = 10/\tau_p = 5$.

DPD with implicit solvent

Recently, a solvent-free DPD model for membrane simulations was presented [202, 203, 204]. This model leaves out the water solvent of conventional DPD and uses instead attractive forces between lipid tails to mimic the influence of the solvent. Due to the reduction of the total number of beads in the system, this implicit-solvent model saves computational power and represents a very effective way to access much larger systems than conventional DPD.

In most of its parts, the implicit-solvent DPD works equivalently to conventional DPD. All beads within a certain interaction range interact via a repulsive force $\vec{F^C}$, a dissipative force $\vec{F^D}$ and a random force $\vec{F^R}$ (the latter two forming the thermostat); beads which form lipids or other large objects are linked via harmonic forces; chains are stiffened by an angle potential. The forces have the same form as in normal DPD, with the coefficients of repulsion a_{ij}, harmonic force k_{harm}, angle force k_{stiff} and the equilibrium distance l_0 differing slightly from their values in normal DPD because they were adapted to the demands of the implicit model. Lipids in implicit-solvent DPD consist from one hydrophilic headgroup and only two hydrophobic tailgroups.

To mimic the effect of the solvent which is left out, a newly introduced attractive force $\vec{F^A}$ acts between any two hydrophobic beads which are within a certain interaction distance $r_0 < r_{ij} < r_0 + w$:

$$\vec{F}_{ij}^A = \begin{cases} -\vec{e}_{ij}\pi\epsilon\sin(\frac{\pi(r_{ij}-r_0)}{w})/(2w) & \text{for } r_0{<}r_{ij}{<}r_0{+}\mathrm{w} \\ 0 & \text{for } r_{ij} \leq r_0 \text{ and } r_{ij} \geq r_0 + \mathrm{w} \end{cases} \tag{7.24}$$

Here, ϵ is the attraction energy in units of k_BT and w is the typical length scale of the attraction. The interaction constants in implicit solvent DPD are chosen as $a_{HH} = a_{HT} = a_{TH} = 48k_BT$, $a_{TT} = 96k_BT$, $k_{harm} = 120k_BT$, $k_{stiff} = 20k_BT, l_0 = 0.6r_0$, $w = r_0$, $\epsilon = 1.4k_BT$.
Similarly to normal DPD, the equations of motion for implicit-solvent DPD are integrated using the DPD velocity Verlet algorithm which is extended by $\vec{F_A}$. The size of the timestep can be chosen similarly to normal DPD. Also the DPD barostat can be used for equilibrating systems to yield tensionless membranes.

Chapter 8

Results – Size-dependent diffusion of membrane inclusions

In this chapter the results of DPD computer simulations are presented in which the diffusion coefficients of differently sized membrane inclusions were determined; the simulation procedure, the obtained results and their interpretation are described and discussed in detail.

8.1 Problem definition

While several available studies support the validity of the Saffman-Delbrück theory for small inclusion radii, its validity for larger radii has not been probed yet, just as little as the predictions of Hughes et al. [176] for very large radii. The observations of Reference [180] which contradict the Saffman-Delbrück theory underline even more that it is still an open question how two-dimensional diffusion coefficients of membrane inclusions are related to radii, membrane thickness and viscosities.

For a robust experimental test of the size-dependence of diffusion, it would be desirable to measure the diffusion coefficients of various membrane inclusions covering a broad range of radii. However, this is a challanging task, first of all because a suitable experimental system with adjustable inclusions typically is lacking. When, for example, proteins or protein oligomers are used as inclusions, their radii must be determined independently, for example via NMR or scattering experiments. Furthermore, in the measurment of diffusion coefficients all imperfections of the experimental system, for example a hydrophobic mismatch of proteins causing local membrane perturbations [205], can lead to a shift in the effectively detected D. An exact determination of D also may be affected by membrane curvature [206] and membrane fluctuations [207] as well as by limitations of the used measurement technique, in particular FRAP [51].

In the following, an alternative option to experimental investigations on the diffusion of membrane inclusions will be presented. It will be demonstrated that particle-based mesoscopic computer simulation of the DPD class are a suitable approach to clarify the validity of the Saffman-Delbrück relation and its extension.

8.2 Simulation procedure

Implementation of DPD

The DPD algorithm as described in Section 7.3 was implemented in a software program written in Fortran 90. The general functionality of the DPD program was tested by monitoring a number of physical observables:

- The average kinetic temperature

$$\langle k_B T \rangle = \frac{m}{3N-3} \langle \sum_{i=1}^{N} \vec{v}_i^2 \rangle \tag{8.1}$$

must be constant for a canonical ensemble and have the same value as set in the simulation.

- The center of gravity

$$\vec{R}_{center} = \sum_{i=1}^{N} \vec{r}_i m_i / (\sum_{i=1}^{N} m_i) \tag{8.2}$$

of the entire system must be conserved in the center of the box.

- The average velocity

$$< \vec{v} > = \frac{1}{N} \sum_{i=1}^{N} \vec{v}_i \tag{8.3}$$

of all beads must be conserved to 0.

- The distribution $p(v)$ of the absolute velocities $v = \sqrt{v_x^2 + v_y^2 + v_z^2}$ of the beads must correspond to the Maxwell-Boltzmann distribution:

$$p(v) = \sqrt{\frac{2}{\pi}} (\frac{m}{k_B T})^{3/2} v^2 e^{\frac{-mv^2}{2k_B T}} \tag{8.4}$$

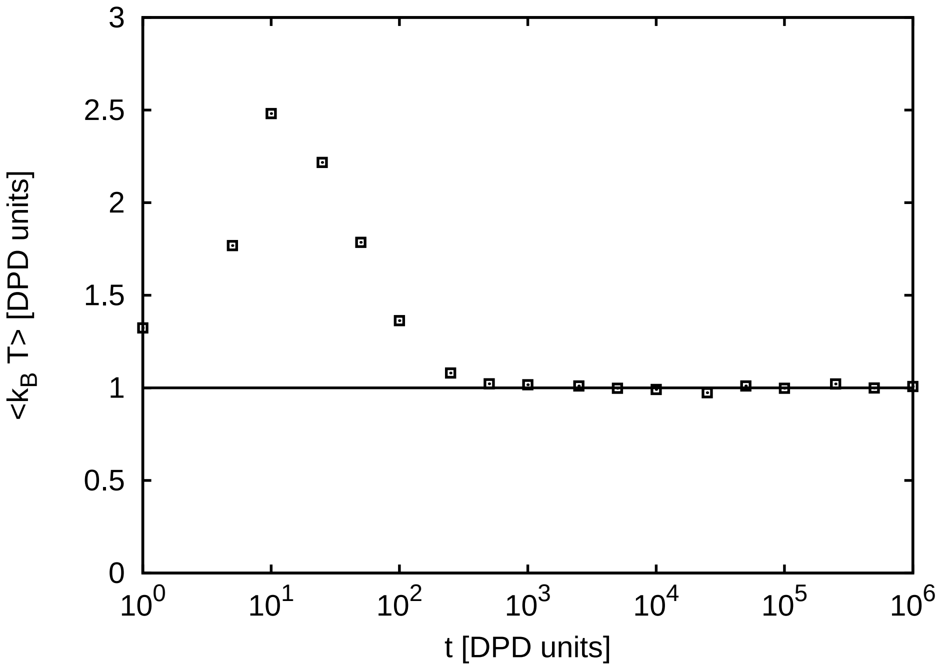

Figure 8.1: Average kinetic temperature $\langle k_B T \rangle$ Eq. 8.1 of a pure water DPD system (symbols). After an equilibration time of about 500 steps, the constant value $\langle k_B T \rangle$ $\approx$ 1 is reached.

For a pure water system of a volume $15 \cdot 15 \cdot 15$ that was simulated for 10^6 time steps, the DPD program used here yielded an average kinetic temperature that became constant after an equilibration time of at a value of $k_B T = 1.012$ (see Figure 8.1 for a plot). The center of gravity was conserved in the box center, i.e. at $\vec{R}_{center} =$ (7.5,7.5,7.5), the average velocity was $< \vec{v} > =$ (0,0,0). The distribution of absolute velocities followed the Maxwell-Boltzmann distribution (see Figure 8.2. All test variables therefore were in an excellent agreement with the expected values, which shows that the DPD algorithm works properly.

The barostat was tested by calculating the dimensionless compressibility κ^{-1} of water from the volume fluctuations dV of the simulation box in case of a pure water system via [200]:

$$\kappa^{-1} = \frac{V}{\langle dV^2 \rangle \rho} \tag{8.5}$$

Here, V is the average box volume and ρ denotes the number density.
With the DPD program used here, simulations of a $15 \cdot 15 \cdot 15$ box with pure water yielded $\kappa^{-1} = 15.92$, which is a good reproduction of values $\kappa^{-1} = 16.1$ given by Reference [200] and $\kappa^{-1} = 15.98$ given by Reference [196].

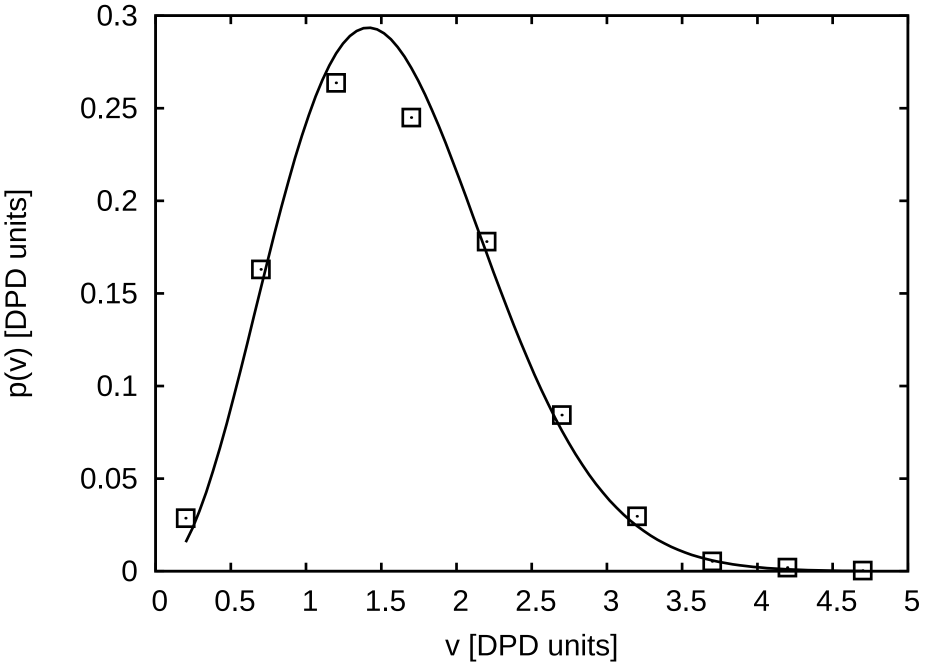

Figure 8.2: The distribution $p(v)$ of absolute velocities v in a DPD water system (symbols) follows the Maxwell-Boltzmann distribution Eq. 8.4 (line).

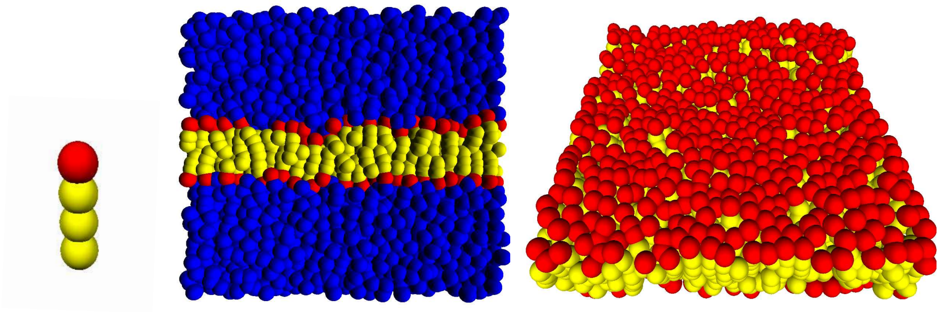

Figure 8.3: *(Left)* A single lipid as used in DPD simulations, consisting from a hydrophilic headgroup (red) and three hydrophobic tailgroups (yellow). *(Center and right)* A self-assembled DPD membrane consisting of single lipids in a cross section (surrounded from water) and a topview (water not shown).

DPD membrane and inclusions

In the DPD simulations presented here, the diffusion of differently sized membrane inclusions was investigated. For this purpose, independent simulations were performed with the Laradji lipid model (lipid length 4) [193]. A single lipid and a self-assembled membrane in the Laradji model are shown in Figure 8.3.

The membrane inclusions in the simulations were modeled as cylinders of hexagonal cross section, consisting of single chains of double lipid length, i.e. the chain length was $N = 8$ beads. The first and the last bead in every chain (top and bottom of the cylinder) were hydrophilic, the $(N - 2)$ beads between were hydrophobic. In total, an inclusion consisted of $2 \cdot N \cdot (3 \cdot K \cdot (K + 1) + 1)$ beads, where $(K + 1)$ is the edge length of the hexagon. The beads in an inclusion were interconnected along the chains and within each layer with Hookean springs of the potential U_{harm}, as in the lipids. Each chain was given a bending rigidity with the potential U_{stiff}. Each inclusion was assigned a radius. The radius was determined from the simulations by measuring the distance of opposite corner beads in a bead layer of the hexagon. The examined inclusions had edge lengths of $(K + 1) = 2$, 3, 4, 6, 8, 10, 15, 20 beads. Example pictures of differently sized inclusions are displayed in Figure 8.4.
All membrane simulations with inclusion of an edge length $(K + 1) = 2$ - 15 were performed in a simulation box with the initial dimensions $L_x = 40r_0$, $L_y = 40r_0$, $L_z = 16r_0$. Membrane simulations with inclusion of a edge length $(K + 1) = 20$ were done in a simulation box with the initial dimensions $L_x = 45r_0$, $L_y = 45r_0$, $L_z = 16r_0$. The systems had always periodic boundary conditions. The membrane was stretched out in the x-y-plane; the box height in z-direction was chosen such that the box was fourfold bigger than the membrane thickness.
Simulations were started with the lipids being already in the configuration of a membrane with initial positions on a lattice. The hexagonal inclusion was initially

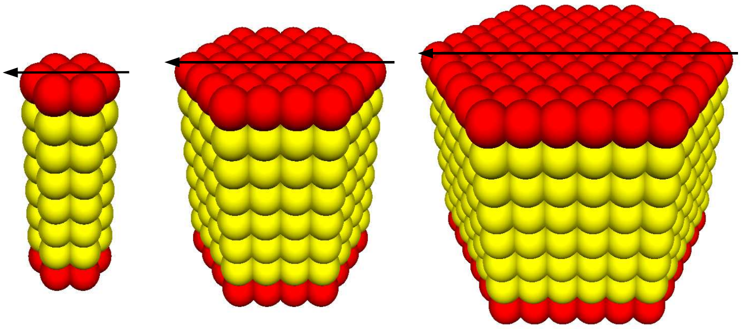

Figure 8.4: Hexagonal membrane inclusions with edge lengths $(K+1) = 2, 4, 6$, consisting of hydrophilic (red) and hydrophobic (yellow) groups. The black arrows display the orientation vectors of the inclusions that were used to determine the rotational diffusion coefficients.

placed in the membrane middle. The lipid density was that of the used membrane model reduced by the number of chains which formed the membrane inclusion.
The box was equilibrated for $3 \cdot 10^4$ timesteps with the barostat to ensure that the membrane with the inclusion was tensionless. Then L_x, L_y, L_z were fixed and simulation was performed for 10^6 timesteps. As timestep, dt =0.01 was chosen for simulations with and without the barostat. Every 100 timesteps the position of the inclusion's center of mass and the 'spin vector' of the inclusion were recorded. The 'spin vector' denotes the vector which points from the the central bead in the top bead layer of the inclusion to the bead which is at the beginning of the simulation at the left corner of the top bead layer (see Figure 8.4).

Determination of inclusion radii

The radius R of an inclusion was determined from the simulations by measuring the distance δ of opposite corner beads in the upper layer of the hexagon; then $R = \delta/2$. For each radius, the average over 80 time steps in the equilibrated system was taken. The resulting radii in simulation units are shown in the Table 8.1.

Determination of diffusion coefficients

The lateral diffusion coefficient D of an inclusion was extracted from its recorded trace $\vec{x}(t)$, while the rotational diffusion coefficient D_{rot} was obtained from the rotating spin vector $\vec{S}(t)$.

Laradji model			
(K+1)	R $[r_0]$	D $[r_0^2/(100dt)]$	D_{rot} $[2 \cdot\pi/(100dt)]$
2	0.52	0.0113	0.00796
3	1.04	0.0105	0.00433
4	1.56	0.0090	0.00159
6	2.62	0.0075	0.00080
8	3.67	0.005	0.00016
10	4.72	0.0043	0.00032
15	7.34	0.0028	0.00012
20	9.96	0.0025	0.00005

Table 8.1: Coefficients of lateral diffusion D and rotational diffusion D_{rot} of a hexagonal cylinder with edge length $(K+1)$ and radius R in a lipid bilayer in the DPD model of Laradji (DPD units).

The values of the mean square displacement $\langle \Delta x^2(\tau)\rangle$ at particular time steps τ_i can be calculated via:

$$\langle \Delta x^2(\tau_i)\rangle = \sum_{j=1}^{m-i} \frac{\Delta\vec{x}_j^2}{m-i} \tag{8.6}$$

Here, the $\tau_i = i \cdot dt$ denote the time increments between i simulation steps. The values $\Delta\vec{x}_j = \vec{x}(t_j + \tau_i) - \vec{x}(t_j)$ denote the $j = (m-i)$ distances which can be extracted from the inclusion's trace for each τ_i.

The lateral diffusion coefficient D was determined by comparing the curve yielded from Equation 8.6 with the theoretically expected mean square displacement for diffusion in two dimensions:

$$\langle \Delta x^2(\tau)\rangle = 4D\tau. \tag{8.7}$$

Figure 8.5 shows the mean square displacement of an inclusion with edge length $(K+1) = 2$ and its fit with Equation 8.7. In the plot, it can be seen that the motion of the inclusion is ballistic for short times and becomes diffusive for larger times, i.e. $\langle \Delta x^2(\tau)\rangle \sim \tau$. At high τ, statistics become bad, which can be seen in a flattening or fluctuations of the curve. The diffusion coefficients (in DPD units) of all inclusions as determined by fitting their mean square displacements with Equation 8.7 are shown in the Table 8.1.

The rotational diffusion coefficient D_{rot} of an inclusion was determined from the angular mean square displacement of the inclusion's 'spin vector'. The spin vector

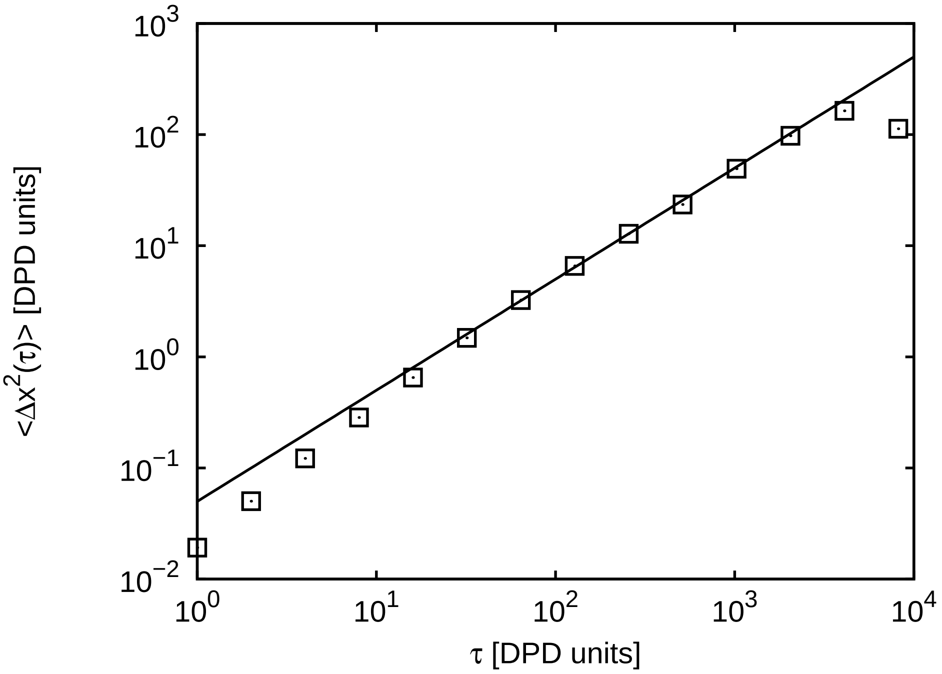

Figure 8.5: Mean square displacement $\langle \Delta x^2(\tau) \rangle$ of a membrane inclusion (data points); fit with equation 8.7 (black curve).

pointed from the bead in the inclusion center to a specific bead at the inclusion's edge and rotated during the simulations about an axis perpendicular to the membrane plane. The angular mean square displacement of the spin vector is:

$$\langle \Delta\phi^2(\tau_i) \rangle = \sum_{1}^{m-i} \frac{\Delta\phi_j^2}{m-i} \tag{8.8}$$

Here, the $\tau_i = i \cdot dt$ denote the time increments between i simulation steps. The values $\Delta\phi_j = \phi(t_j + \tau_i) - \phi(t_j)$ denote the $j = (m-i)$ relative angles between the spin vectors for each τ_i.

The rotational diffusion coefficient D_{rot} was determined by comparing the curve obtained via Equation 8.8 with the theoretically expected angular mean square displacement for rotational diffusion in two dimensions:

$$\langle \Delta\phi^2(\tau) \rangle = 2D_{rot}\tau \tag{8.9}$$

When plotting $\langle \Delta\phi^2(\tau_i) \rangle$ against τ_i for i=1,m, one can fit with equation 8.9. The rotational diffusion coefficients obtained from the fit are shown in Table 8.1.

Conversion of DPD simulation units to SI units

DPD data are converted to SI units by comparing values from the simulation with experimentally measured values [197]. For determining the observed length scale in the simulation, the membrane thickness detected in DPD was compared with synthetic bilayers having a thickness of 3.5 nm [159]. The thickness of the DPD membranes was obtained by averaging the distance of all hydrophilic lipid head beads in the opposing leaflets of the bilayer ('phosphate-to-phosphate distance'). The internal timescale was determined by comparing the numerically obtained diffusion coefficient of a single lipid with the experimentally measured value of a lipid diffusion coefficient $D_{Exp} = 4\ \mu m^2/s$ [162].
In the simulations, the average membrane thickness was $\approx 3.2\ r_0$. This set the internal length scale to $r_0 = 1.1$ nm. The diffusion coefficient of a single lipid $D_{DPD} = 0.03 \frac{r_0^2}{100dt}$ yielded that a single time step $dt = 0.01$ corresponded to 91 ps.

Viscosity of DPD water

For measuring the viscosity of the DPD solvent (water), the traces of a single water bead and of differently sized hexagonal cylinders diffusing freely in a simulation box filled with water beads (bead density $\rho = \frac{3}{r_0^3}$) were monitored. From the traces, the diffusion coefficients of the cylinders were extracted.
The cylinders had the same shape as the membrane inclusions described above, but were composed only from hydrophilic beads. The beads were connected via Hookean springs, using the spring potential of the Laradji model ($k_{harm} = 100k_BT$, $l_0 = 0.45r_0$). The edge lengths of the cylinders were $(K+1)$ beads which yielded a diameter of $(2K+1)$ beads, the cylinder heights were chosen $(2K+1)$ beads. For a single bead, a radius $R_{bead} = (\frac{1}{\rho})^{1/3}/2$ was assumed, which yielded in SI units R_{bead} $= 0.38$ nm. The cylinders were regarded as spheres of different sizes, since their lengths were chosen similarly to their diameters, and since they could rotate freely. Each cylinder was assigned a radius $R = \sqrt{2 \cdot (Kl_0 + R_{bead}/2)}$, which corresponds to the distance from the central bead of the cylinder to a bead in a corner of the hexagon.
The dependence of their diffusion coefficients on size was fitted with the Einstein-Stokes relation $D = \frac{k_BT}{c\pi\eta_c R}$, with $c = 6$ for stick boundary conditions and $c = 4$ for slip boundary conditions. Setting $c = 6$ yielded a good description of the data and determined the viscosity of DPD water to be $\eta_c \approx 0.04$ Pas (see Figure 8.6). Bearing in mind the somewhat vaguely defined radii R (due to the use of soft-core potentials) and the uncertainty if stick or slip boundary conditions are more appropriate in the Einstein-Stokes formula for fitting the DPD data, the value for η_c may be slightly higher or lower.

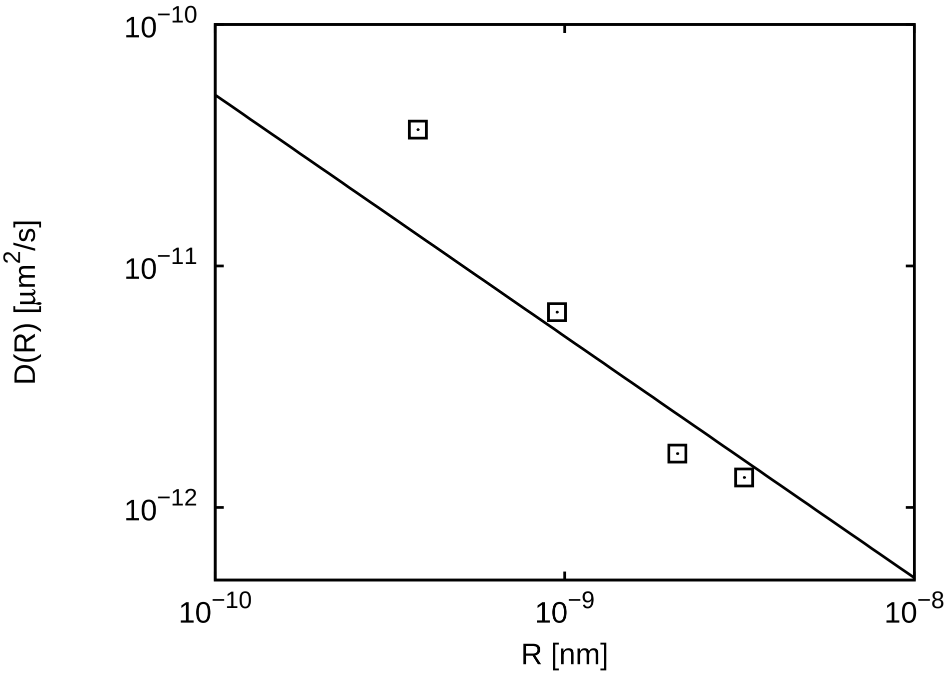

Figure 8.6: Lateral diffusion coefficients D of hexagonal cylinders in a water box in dependence of the cylinder radii (data points); fit with the Einstein-Stokes relation (black curve).

8.3 Results

Size-dependent diffusion of membrane inclusions

To investigate the diffusion of large inclusions in a membrane bilayer, in particular to examine the predictions of the Saffman-Delbrück theory, computer simulations of the DPD scheme were performed. The model system used here consisted of three types of beads: water beads, hydrophilic groups and hydrophobic groups. Lipids were constructed from one hydrophilic bead representing the polar head group and three hydrophobic beads representing the hydrocarbon chains. Membranes were ensured to be self-assembling and stable.
Membrane inclusions were modeled as membrane spanning cylinders with a hexagonal cross-section, consisting from single chains of double lipid length. Edge length of the hexagonal cylinder was $(K+1)$ beads. The top and bottom plane of the cylinders consisted from hydrophilic beads, and the six core planes consisted from hydrophobic beads (see Figure 8.4 for illustration).

To determine the lateral and rotational diffusion coefficients of membrane inclusions with different radii, independent simulations were performed with just one

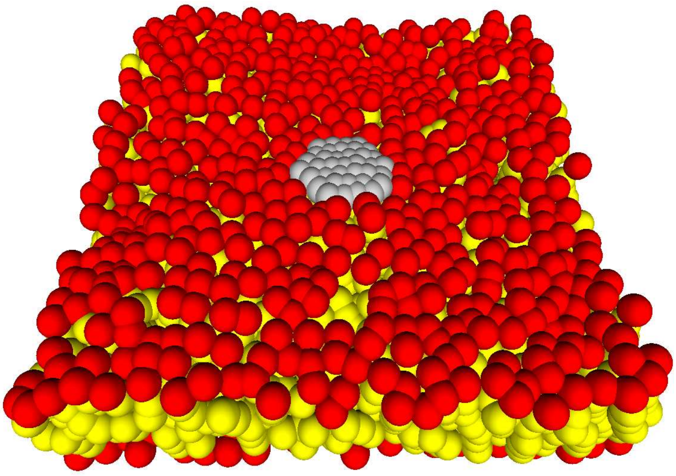

Figure 8.7: Cylindrical inclusion (displayed in grey) with an edge length $(K + 1) = 4$ diffusing in a membrane.

inclusion embedded in a large membrane patch. The membrane with the inclusion was made tensionless by equilibration with a barostat [200]. In the equilibrated system, the lateral motion and the rotation of the inclusion was recorded for a large time period. To be able to relate the results to biological systems, the simulation units were transferred to SI units. Here, simulations lasted $\approx 90\ \mu s$; membrane patches had a size of $\approx 40 \cdot 40\ \mathrm{nm}^2$ and the examined inclusions had radii $R =$ 0.57 - 10.96 nm.

In Figure 8.7, a snapshot of an inclusion embedded in a membrane is shown. From an inclusion's recorded trace and rotation, the coefficients of lateral diffusion D and rotational diffusion D_{rot} were obtained by fitting the translational and angular mean square displacements. The resulting diffusion coefficients are shown together with the inclusion radii in Table 8.2 (in SI units).

To examine the predictions of hydrodynamic theory [2] on the radius dependence of diffusion coefficients, the determined D and D_{rot} were plotted against the inclusion radii R. The resulting curves were compared to the predictions of the Saffman-Delbrück theory [2] for lateral diffusion (Equation 7.4) and rotational diffusion (Equation 7.3). The comparison was done by optimising three parameters in the Saffman-Delbrück equations: the membrane thickness h, the membrane viscosity η_m and the water viscosity η_c.

As a result, both lateral and rotational diffusion coefficients were observed to be described excellently by the Saffman-Delbrück relations. The data for lateral diffusion is displayed in Figure 8.8. The best fit of the lateral diffusion could be done with the parameters $h = 3.5$, $\eta_m = 0.19$ Pas, $\eta_c = 0.039$ Pas. The solvent viscosity η_c matched well with the value determined independently for the pure solvent. The membrane viscosity η_m could not be determined independently, but is

Laradji model			
(K+1)	R [nm]	D [$\mu m^2/s$]	D_{rot} [$2\pi/\mu s$]
2	0.57	1.50	0.87
3	1.14	1.40	0.476
4	1.72	1.20	0.175
6	2.88	1.00	0.088
8	4.04	0.67	0.018
10	5.19	0.57	0.035
15	8.07	0.37	0.013
20	10.96	0.33	0.006

Table 8.2: Coefficients of lateral diffusion D and rotational diffusion D_{rot} of a hexagonal cylinder with edge length $(K+1)$ and radius R in a lipid bilayer in the DPD model of Laradji (SI units).

in good agreement with typical data from the literature for artificial membranes [159].
The best fit of the rotational diffusion (see Figure 8.9) could be done with the prefactor $\frac{k_B T}{4\pi\eta_m h} = 0.5\ \mu m^2/s$, which is in a good agreement with the value 1.1 $\mu m^2/s$ obtained from h and η_m as determined by fitting the lateral diffusion coefficient.

The Saffman-Delbrück theory is valid only for inclusion radii $R < R_c$, with R_c being dependent on the membrane thickness and the viscosities in the system (c.f. Equation 7.5). Beyond R_c, the extended theory of Hughes et al. becomes valid (Equation 7.6). With the values for h, η_m, η_c as determined for the present simulation systems, the critical radius is $R_c \approx 17.05$ nm. The largest inclusion whose diffusion was examined in the simulations had a radius $R \approx 10.96$ nm and was thus below R_c. To investigate the dependence of D on R for large radii beyond R_c, simulations with inclusion radii would be necessary that exceed the present maximum radius by factors of two, three and more. In the framework of the present thesis, the examination of such large inclusions was not possible, since available computers do not allow to perform DPD simulations of appropriatly large systems within a reasonable time period. In particular, in a suitable simulation box the lengths in x- and y- directions must be larger than 2 times the diameter of the inclusion, in order to avoid an interference of the inclusion with itself via the solvent. Since always two box lengths have to be increased, the number of beads inside the box grows quadratically, and the same is true for the simulation time.

In summary, the performed DPD simulations on membrane inclusions demonstrated the Saffman-Delbrück theory to describe the radius dependence of diffusion coefficients excellently. Both the predictions of a scaling $D \sim \log(1/R)$ for lateral

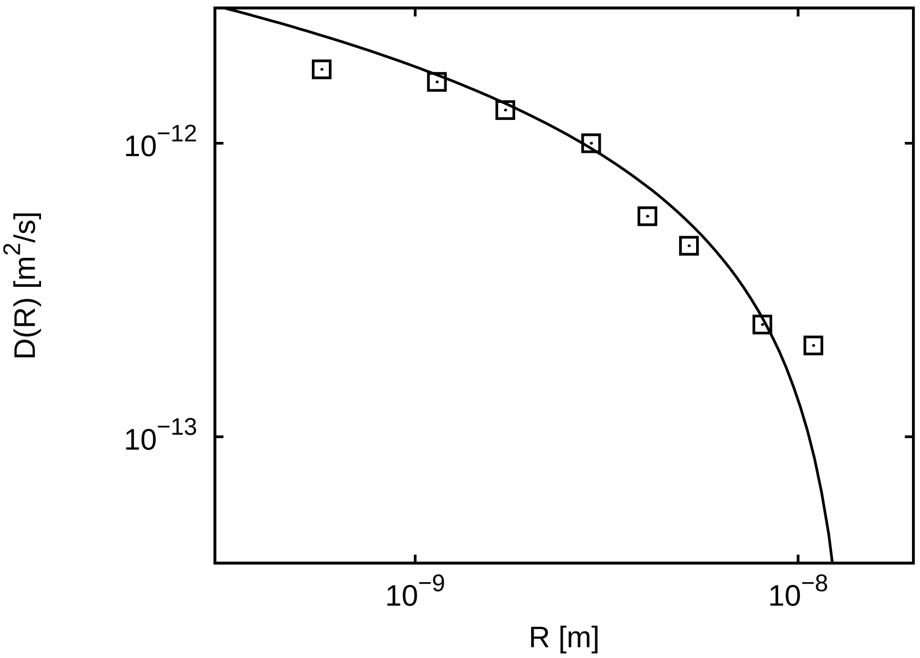

Figure 8.8: Lateral diffusion coefficients D of membrane inclusions in dependence of the inclusion radii R (data points); fit with the Saffman-Delbrück relation for lateral diffusion (black curve).

diffusion and $D_{rot} \sim 1/R^2$ were reproduced clearly in the simulations for all accessible inclusion sizes, which covered small and intermediate radii of $\approx R_c/2$ in maximum. These observations represent a confirmation and an extension of earlier experimental studies which already detected the validity of the Saffman-Delbrück theory for very small radii.

8.4 Beyond the validity regime of the Saffman-Delbrück theory

Parallelly to the DPD study presented in Section 8.3, a similar study was performed with implicit-solvent DPD by Matthias Weiss. Implicit-solvent DPD works without the water solvent of normal DPD, mimicking its influence by an attractive force between hydrophobic groups in the system, e.g. lipid tails. Due to the strong reduction of beads (e.g. for a $30 \cdot 30 \cdot 15$ nm^3 box, 3/4 of the beads are water beads), implicit-solvent DPD permits to access much larger membrane patches than normal DPD.

In the work of M. Weiss the implicit-solvent model of Reference [204] was used. Here, lipids differ from the standard DPD models used in the simulations above in

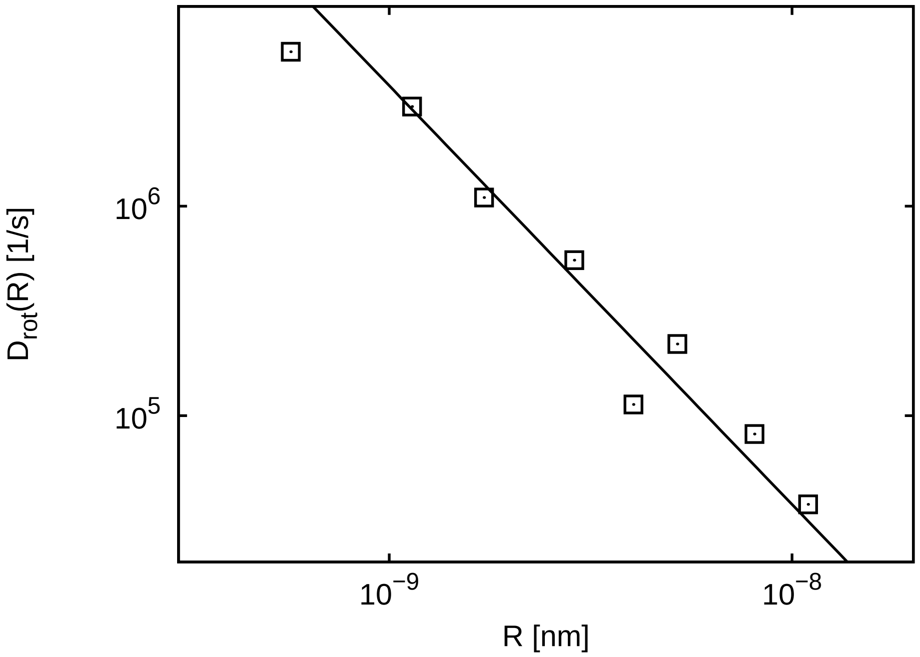

Figure 8.9: Rotational diffusion coefficients D_{rot} of membrane inclusions in dependence of the inclusion radii R (data points); fit with the Saffman-Delbrück relation for rotational diffusion (black curve).

that they consist from one headgroup and only two tailgroups.
In the study of M. Weiss, lateral and rotational diffusion coefficients of differently sized membrane inclusions were determined by recording their trace and rotation, similarly to the study presented above. As inclusions, the hexagonal cylinders described in Section 8.2 were used. Since lipids in the implicit-solvent DPD model have only two hydrophobic tailgroups, the bead chains composing the inclusions consisted accordingly from only six beads in length, with four hydrophilic beads in the middle and one hydrophobic bead at each end of the chain.
The simulation procedure in the work of M. Weiss was the same as described in Section 8.2. Initially, the simulation box was equilibrated with a barostat for $3 \cdot 10^4$ timesteps to get a tensionless bilayer. Then the box size was fixed and the position of the diffusing inclusion and its spin vector were recorded during a simulation of 10^6 timesteps. The lateral and rotational diffusion coefficients were determined analogously to the description in Section 8.2. Convertion from the simulation units to SI units was done as described in Section 8.2 by comparing the bilayer thickness and the diffusion coefficient of a lipid in the simulation with experimentally determined values. This resulted in $dt \approx 80$ ps, $r_0 \approx 1$ nm. A simulation lasted therefore ≈ 80 μs.
The inclusion radii accessible to implicit-solvent DPD were considerably larger than the radii accessible to normal DPD and lied at $R \approx 0.76$ - 50 nm. Thus, the validity

regimes of both the Saffman-Delbrück theory and its extension by Hughes et al. were covered.

The coefficients of lateral diffusion D as extracted from the implicit-solvent DPD simulations are shown in Figure 8.10. The coefficients were plotted in dependence of the cylinder radii R, and the plots were compared to the predictions of Saffman-Delbrück and of Hughes et al.. As in the study with normal DPD, the comparison was done by fitting the membrane thickness h, the membrane viscosity η_m and the solvent viscosity η_c.

For the lateral diffusion coefficients, the Saffman-Delbrück relation yielded a good fit for inclusions with small radii from ≈ 0.76 - 6 nm. The best fit could be done with $h = 3.3$, $\eta_m = 0.25$ Pas, $\eta_c = 0.056$ Pas. These values are very similar to the values determined with normal DPD. Slight deviations may appear because the models of implicit-solvent DPD and normal DPD are not perfectly congruent, due to different lipid models and varying potential parameters. Furthermore, η_c is not a well-defined quantity in the implicit-solvent approach, as will be explained below.

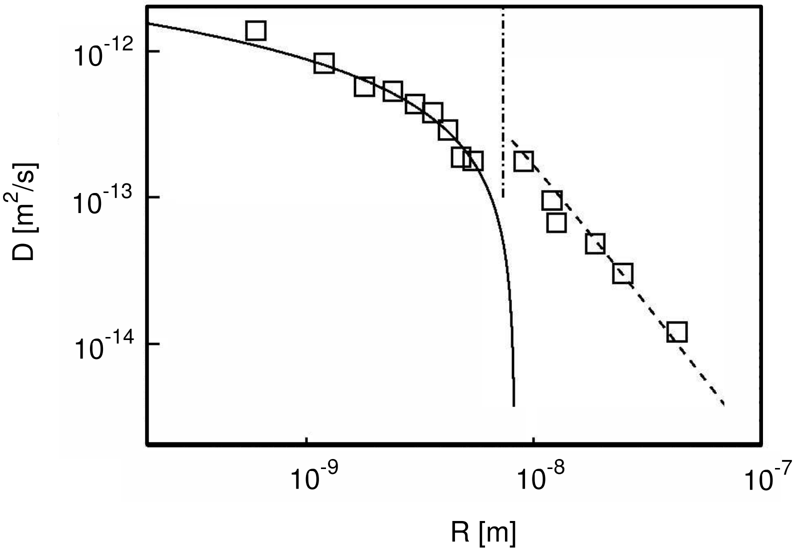

Figure 8.10: Lateral diffusion coefficients D of membrane inclusions in dependence of the inclusion radii R (data points), as determined in the study with implicit solvent DPD of M. Weiss; fits with the Saffman-Delbrück relation for lateral diffusion (full line) and with the expression of Hughes et al. corrected with a term taking in account internal modes of the inclusions (dotted line).

Fitting the entire numerical data with Saffman-Delbrück resulted in a very bad description, with values of η_m and η_c deviating strongly from the results of the simulations with standard DPD.

The rotational diffusion coefficient was for all inclusion sizes well described by the Saffman-Delbrück theory for rotational diffusion (which is by definition valid for all radii). The prefactor of the best fit to the data yielded $\frac{k_BT}{4\pi\eta_m h} = 0.45\mu m^2/s$, which is in excellent agreement with the value 0.41 $\mu m^2/s$ obtained from h and η_m as determined by fitting the lateral diffusion coefficient for small radii.

With the determined values for h, η_m, η_c, the critical radius for the transition from the Saffman-Delbrück validity regime to the formula of Hughes et al. becomes $R_c \approx$ 14.73 nm. In the $D(R)$ - plots indeed strong deviations from Saffman-Delbrück were observed for inclusion radii larger than $R_c/2$. However, while the formula of Hughes et. al. predicts $D_{Hughes} \sim 1/R$ [176], the lateral diffusion coefficient seemed to decrease faster than linearly with the radius of the inclusion.

This observation was rationalized by the consideration that the hydrodynamic calculations of Saffman-Delbrück and Hughes et al. have used incompressible cylinders as a model for the membrane inclusion. In the DPD simulations, however, the inclusions have internal degrees of freedom, due to their construction as being composed from single beads connected with springs. Due to an inclusion's internal degrees of freedom, the erratic impact of surrounding lipids driving the inclusion's Brownian motion is dissipated in part via the imposed thermostat. As a consequence, only a fraction f of the impact can be used to move the center of mass. This fraction can be estimated to be for large radii $f \approx \frac{c}{R}$, as will be described in Section 8.5. Thus, for $R >> R_c$ the effective lateral diffusion coefficient is $D(R) \sim f \cdot D_{Hughes}$, in particular:

$$D(R) \sim \frac{1}{\eta_c R^2}. \tag{8.10}$$

This relation describes very well the numerical data of M. Weiss when using the previously found viscosity $\eta_c = 0.056$ Pas.

The internal modes of the inclusion and the dissipative forces imposed by the thermostat can also be used to explain the ability of the implicit-solvent approach (where $\eta_c = 0$ by definition) to reproduce hydrodynamic relations like the Saffman-Delbrück formula in which a finite value for η_c is needed. The erratic impact of the surrounding lipids excites shear modes within the inclusion with a polarization perpendicular to the bilayer normal, and these modes are dissipated by the action of the thermostat. A 'neutral layer' of the inclusion located roughly in the mid-plane of the bilayer therefore feels a friction with respect to the layers that lie above and below in-plane with the hydrophilic headgroups of the lipids. Hence, these shear modes mimic an apparent solvent viscosity that should change, when the dissipation strength gamma in the thermostat is altered for the beads within the inclusion.

8.5 The influence of internal modes on the diffusion of large objects in DPD

In DPD, large objects such as membrane inclusions are constructed from single beads being interconnected via harmonic springs. A bead being part of a large object is therefore not perfectly fixed in its relative position within the object but can oscillate, i.e. show Brownian motion in the harmonic potential of stiffness k_{harm}. Since the beads are coupled to the DPD thermostat, their oscillations are related to an enhanced dissipation of energy. This has consequences for the diffusive motion of an object, which is driven by the erratic impact of surrounding solvent molecules. Since the impact also excites internal modes, its energy can be used only partially to move the object's center of mass, while a part is dissipated. Dissipation in this context can be expected to have a significant influence especially on the motion of large objects consisting from many beads and many springs, i.e. in cases where many channels of dissipation exist.

In the following, the fraction f of the original solvent impact that can be used to move the center of mass will be estimated for a cylindrical membrane inclusion as used in the simulations presented above, i.e. a cylinder with a hexagonal cross-section and a diameter of $(2K+1)$ beads.

For a bead performing Brownian motion in a harmonic potential of stiffness k_{harm}, the spectral density describing the energy distribution with frequency is given by [208]:

$$p(\omega) = \frac{2\omega_0}{\pi\omega_0^2 + \omega^2} \tag{8.11}$$

Here, $\omega_0 = \frac{k_{harm}}{\beta}$ is the corner frequency of the oscillator. The parameter β denotes the (local) friction coefficient of the moving bead, which depends on the dissipation strength of the thermostat.

The coupling of many individual beads via springs in an inclusion leads to a spectrum of relaxation times. The longest relaxation time τ here appears due to oscillatory modes along the inclusion diameter, where the largest number of springs is included. This maximum relaxation time τ can be estimated by considering an effective Maxwell element, i.e. a series of purely elastic springs and purely viscous dampers. Along the diameter of the inclusion, the effective Maxwell element consists of $(2K+1)$ springs of stiffness k_{harm} and a damping dashpot of viscosity η_m in series. This element represents effectively a spring with stiffness $k_{harm}/(2K+1)$, yielding the relaxation time $\tau = (2K+1)\eta_m/k_{harm}$.

The lowest frequency, that internal oscillatory modes of the inclusion can have, is $\omega_{min} = \frac{2\pi}{\tau}$. When solvent kicks transmit energies to the inclusion which correspond to frequencies $\omega < \omega_{min}$, they do not induce internal oscillations, but move the center of mass. The fraction f of the solvent impact which is not dissipated but induces the motion of the inclusion's mass center can thus be calculated as:

$$f = \int_0^{\omega_{min}} p(\omega)d\omega = 2\arctan(\frac{const.}{2k+1})/\pi \tag{8.12}$$

Using $R \sim (2K+1)$, this equation becomes

$$f = 2\arctan(\frac{const.}{R})/\pi \sim \frac{1}{R} \text{ for large } R \tag{8.13}$$

When the dissipation of energy due to internal modes is considered, the effective lateral diffusion coefficient of an inclusion will be

$$D_{effective} = f \cdot D, \tag{8.14}$$

with D being the lateral diffusion coefficient as expected from hydrodynamic theory for the incompressible equivalent to the considered inclusion.

The expressions Eq. 8.13 and Eq. 8.14 should hold when the diffusive motion on short and intermediate timescales is quantified. The contribution of the internal modes can be expected to subside when the diffusive mobility is monitored over asymptotically large times (similar to a random-coil polymer that behaves asymptotically like a diffusing sphere). In this asymptotic regime, one can expect to obtain the hydrodynamic result.

In the diffusion coefficients determined from DPD simulations in Section 8.3, no deviations from hydrodynamic theory were seen; thus the inclusion radii considered there can be regarded as being too small to be affected significantly by internal modes. In the study of M. Weiss described in Section 8.4, however, significant deviations from theoretical predictions appeared for large radii. These were in agreement with the formulas Eq. 8.13 and Eq. 8.14 when the constant was set to $const. = 6$ nm and could thus be ascribed to internal modes of the inclusion.

8.6 Comparing simulation results with experimental data from literature

In the DPD simulations presented here, the radius dependence of lateral and rotational diffusion coefficients of cylindrical membrane inclusions was examined. The largest inclusion sizes accessible to the simulations were lying at about half R_c. As a result, all diffusion coefficients determined from the simulations were in agreement with the predictions of the hydrodynamic theory of Saffman and Delbrück [2]. This result extends the observations of available experimental studies which detected the Saffman-Delbrück theory already to be valid for very small inculsion radii [178, 177, 179, 175].

The simulations of M. Weiss with implicit-solvent DPD confirmed the described results for small radii and determined as a new result the lateral diffusion of large inclusions with radii beyond R_c to be properly described by the theory of Hughes et al. [176]. The study of M. Weiss further detected lateral diffusion coefficients of huge inclusions to be affected from internal modes when the inclusion is not incompressible.

In the recent study of Cicuta et al. [209], observations were made which agree with the results presented here. In [209], the size-dependend diffusion of micron-sized circular lipid domains in vesicles was probed. The membrane viscosity η_m and thus the critical radius R_c of the experimental system could be shifted by altering the lipid composition of the membrane and by changing the temperature. Dependent on the setting of R_c, the diffusion coefficients were in agreement with the Saffman-Delbrück relation or showed the scaling $\sim 1/R$ predicted by Hughes et. al..

The results presented here are in conflict with the recent experimental study of Gambin et al. [180], where strong deviations from the Saffman-Delbrück relation were measured for small model peptides in membranes. In particular, Gambin et al. detected instead a scaling $D \sim 1/R$. However, a possible explanation for this observation was given by a recent theoretical paper [205], where the authors suggest that a putative hydrophobic mismatch of membrane inclusions will lead to local membrane perturbances and, as a consequence, to an enhanced dissipation of energy in the membrane. Lateral diffusion coefficients therefore have been predicted to obey the formula $D_{effective} \sim \frac{D}{1+R\mu}$ (with D and μ being the diffusion coefficient and the mobility of the inclusion in an unperturbated membrane). Assuming that the assumptions of [205] are true, the radius scaling predicted in their formula would be in agreement with the experimental findings of Reference [180].

Bibliography

[1] T. G. Mason and D. A. Weitz. Optical measurements of frequency-dependent linear viscoelastic moduli of complex fluids. *Phys. Rev. Lett.*, 74:1250 – 1253, 1995.

[2] P. G. Saffman and M. Delbrück. Brownian motion in biological membranes. *Proc. Natl. Acad. Sci. USA*, 72:3111–3113, 1975.

[3] H. C. Berg. *Random Walks in Biology.* Princeton University Press, 1993.

[4] A. Einstein. Über die von der molekularkinetischen Theorie der Waerme geforderte Bewegung von in ruhenden Flüessigkeiten suspendierten Teilchen. *Annal. Physik.*, 17:549–560, 1905.

[5] A. Fick. Über Diffusion. *Ann. Phys. (Leipzig)*, 170:50, 1855.

[6] R. Metzler and J. Klafter. The random walk's guide to anomalous diffusion: A fractional dynamics approach. *Phys. Rep.*, 339:1–77, 2000.

[7] L. F. Richardson. Atmospheric diffusion shown on a distance-neighbour graph. *Proc. R. Soc. London, Ser. A*, 110:709, 1926.

[8] L. Hufnagel, D. Brockmann, and T. Geisel. Forecast and control of epidemics in a globalized world. *Proc. Natl. Acad. Sci. USA.*, 101:15124 – 15129, 2004.

[9] H. Scher and E. W. Montroll. Anomalous transit-time dispersion in amorphous solids. *Phys. Rev. B*, 12:2455, 1975.

[10] E. Fischer, R. Kimmich, U. Beginn, M. Moeller, and N. Fatkullin. Segment diffusion in polymers confined in nanopores: A fringe-field NMR diffusometry study. *Phys. Rev. E*, 59:4079, 1999.

[11] S. Yamada, D. Wirtz, and S. C. Kuo. Mechanics of living cells measured by laser tracking microrheology. *Biophys J*, 78:1736–1747, 2000.

[12] J.-P. Bouchaud and A. Georges. Anomalous diffusion in disordered media: Statistical mechanisms, models and physical applications. *Phys. Rep.*, 195:12, 1990.

[13] M. J. Saxton. Anomalous diffusion due to obstacles: A Monte Carlo study. *Biophys. J.*, 66:394–401, 1994.

[14] B. Schulz and S. Trimper. Random walks in two-dimensional glass-like environments. *Phys. Let. A*, 256:266–271, 1999.

[15] B. I. Halperin, S. Feng, and P. N. Sen. Differences between lattice and continuum percolation transport exponents. *Phys. Rev. Lett.*, 54:2391, 1985.

[16] A. Bunde and S. Havlin (eds). *Fractals in Science.* Springer, Heidelberg, 1996.

[17] M. J. Saxton. Lateral diffusion in an archipelago. The effect of mobile obstacles. *Biophys. J.*, 52:989–997, 1987.

[18] M. J. Saxton. Lateral diffusion in an archipelago. Dependence on tracer size. *Biophys. J.*, 64:1053–1062, 1993.

[19] B. B. Mandelbrot. *The Fractal Geometry of Nature.* Freeman, San Francisco, CA, 1982.

[20] S. Havlin and D. Ben-Avraham. Diffusion in disordered media. *Adv. Phys.*, 36:695–798, 1987.

[21] M. J. Saxton. Anomalous diffusion due to binding: A Monte Carlo study. *Biophys. J.*, 70:1250–1262, 1996.

[22] M. J. Saxton. A biological interpretation of transient anomalous subdiffusion. I. Qualitative model. *Biophys. J.*, 92:1178–1191, 2007.

[23] R. Metzler and J. Klafter. The restaurant at the end of the random walk: Recent developments in the description of anomalous transport by fractional dynamics. *J. Phys. A: Math. Gen.*, 37:R161–R208, 2004.

[24] H. Harder, S. Havlin, and A. Bunde. Diffusion on fractals with singular waiting-time distribution. *Phys. Rev. B.*, 36:3874–3879, 1987.

[25] T. G. Mason, K. Ganesan, J. V. van Zanten, D. Wirtz, and S. C. Kuo. Particle-tracking microrheology of complex fluids. *Phys. Rev. Lett.*, 79:3282–3285, 1997.

[26] B. R. Dasgupta, S.-Y. Tee, J. C. Crocker, B. J. Frisken, and D. A. Weitz. Microrheology of polyethylene oxide using diffusing wave spectroscopy and single scattering. *Phys. Rev. E*, 65:051505, 2002.

[27] D. Weihs, T. G. Mason, and M. A. Teitell. Bio-microrheology: A frontier in microrheology. *Biophys. J.*, 91:4296 – 4305, 2006.

[28] H. Qian. Single-particle tracking: Brownian dynamics of viscoelastic materials. *Biophys. J.*, 79:137–143, 2000.

[29] G. Adam and M. Delbrück. Reduction of dimensionality in biological diffusion processes. In *Structural Chemistry and Molecular Biology* (Rich, A., and Davidson, N., eds), p. 198-215. W. H. Freeman and Co., New York, 1968.

[30] O. Berg and P. von Hippel. Diffusion-controlled macromolecular interactions. *Annu. Rev. Biophys. Biophys. Chem.*, 14:131–160, 1985.

[31] G. M. Viswanathan, S. Buldyrev, S. Havlin, M. G. E. da Luz, E. P. Raposo, and H. E. Stanley. Optimizing the success of random searches. *Nature*, 401:911, 1999.

[32] G. M. Viswanathan, V. Afanasyev, S. V. Buldyrev, S. Havlin, M. G. E. da Luz, E. P. Raposo, and H. E. Stanley. Lévy flights search patterns of biological organisms. *Physica*, 85:295A, 2001.

[33] F. Bartumeus, J. Catalan, U. Fulco, M. Lyra, and G. Viswanathan. Optimizing the encounter rate in biological interactions: Lévy versus Brownian strategies. *Phys. Rev. Lett.*, 88:097901, 2002.

[34] B. Alberts, A. Johnson, J. Lewis, M. Raff, K. Roberts, and P. Walter. *Molecular Biology of the Cell. 4th Edition.* Garland Science, New York, 2002.

[35] B. J. Marsh, D. N. Mastronarde, K. F. Buttle, K. E. Howell, and J. R. McIntosh. Organellar relationships in the Golgi region of the pancreatic beta cell line, hit-t15, visualized by high resolution electron tomography. *Proc. Natl. Acad. Sci. USA.*, 98:2399–2406, 2001.

[36] A. Fulton. How crowded is the cytoplasm? *Cell*, 30:345–347, 1982.

[37] S. B. Zimmerman and A. P. Minton. Macromolecular crowding: Biochemical, biophysical, and physiological consequences. *Annu. Rev. Biophys. Biomol. Struct.*, 22:27–65, 1993.

[38] R. J. Ellis and A. P. Minton. Join the crowd. *Nature*, 425:27–28, 2003.

[39] S. B. Zimmerman and S. O. Trach. Estimation of macromolecule concentrations and excluded volume effects for the cytoplasm of Escherichia coli. *J. Mol. Biol.*, 222:599–620, 1991.

[40] Record T. M. Jr, Courtenay E. S., Cayley S., and Guttman H. J. Biophysical compensation mechanisms buffering E. coli protein-nucleic acid interactions against changing environments. *Trends Biochem. Sci.*, 23:190–194, 1998.

[41] N. Chebotareva, B. Kurganov, and N. Livanova. Biochemical effects of molecular crowding. *Biochemistry (Moscow)*, 69:1239–1251, 2004.

[42] Hall D. and Minton A. P. Macromolecular crowding: Qualitative and semiquantitative successes, quantitative challenges. *Biochim. Biophys. Acta*, 1649:127–139, 2003.

[43] T. Chang, H. Kim, and H. Yu. Diffusion through coarse meshes. *Macromolecules*, 20:2629–2631, 1987.

[44] M. Weiss, M. Elsner, F. Kartberg, and T. Nilsson. Anomalous subdiffusion is a measure for cytoplasmic crowding in living cells. *Biophys. J.*, 87:3518–3524, 2004.

[45] K. Gruenewald, O. Medalia, A. Gross, A. C. Steven, and W. Baumeister. Prospects of electron cryotomography to visualize macromolecular complexes inside cellular compartments: Implications of crowding. *Biophys. Chem.*, 100:577–591, 2003.

[46] W. E. Moerner and M. Orrit. Illuminating single molecules in condensed matter. *Science*, 12:1670–1676, 1999.

[47] U. Kubitscheck, O. Kückmann, T. Kues, and R. Peters. Imaging and tracking of single GFP molecules in solution. *Biophys. J.*, 78:2170 – 2179, 2000.

[48] T. Kues, R. Peters, and U. Kubitscheck. Visualization and tracking of single protein molecules in the cell nucleus. *Biophys. J.*, 80:2954–2967, 2001.

[49] H. Qian, M. P. Sheetz, and E. L. Elson. Single particle tracking. Analysis of diffusion and flow in two-dimensional systems. *Biophys. J.*, 60:910–921, 1991.

[50] D. Axelrod, D. E. Koppel, J. Schlessinger, E. Elson, and W. W. Webb. Mobility measurement by analysis of fluorescence photobleaching recovery kinetics. *Biophys. J.*, 16:1055–1069, 1976.

[51] M. Weiss. Challenges and artifacts in quantitative photobleaching experiments. *Traffic*, 5:662, 2004.

[52] M. J. Saxton. Anomalous subdiffusion in fluorescence photobleaching recovery: A Monte Carlo study. *Biophys. J.*, 81:2226–2240, 2001.

[53] S. Popov and M. M. Poo. Diffusional transport of macromolecules in developing nerve processes. *J. Neurosci.*, 12:77–85, 1992.

[54] J. R. Lepock, K. H. Cheng, S. D. Campbell, and J. Kruuv. Rotational diffusion of TEMPONE in cytoplasm of Chinese hamster cell. *Biophys. J.*, 44:405–412, 1983.

[55] Mastro A. M. and Keith A. D. Diffusion in the aqueous compartment. *J. Cell. Biol.*, 99:180–187, 1984.

[56] A. M. Mastro, M. A. Babich, W. D. Taylor, and A. D. Keith. Diffusion of a small molecule in the cytoplasm of mammalian cells. *Proc. Natl. Acad. Sci. USA.*, 81:3414–3418, 1984.

[57] K. Luby-Phelps, S. Mujumdar, R. B. Mujumdar, L. A. Ernst, W. Galbraith, and A. S. Waggoner. A novel fluorescence ratiometric method confirms the low solvent viscosity of the cytoplasm. *Biophys. J.*, 65:236–242, 1993.

[58] A. S. Verkman. Solute and macromolecule diffusion in cellular aqueous compartments. *Trends Biochem. Sci.*, 27:27–33, 2002.

[59] Arrio-Dupont M., Foucault G., Vacher M., Douhou A., and Cribier S. Mobility of creatine phosphokinase and beta-enolase in cultured muscle cells. *Biophys. J.*, 73:2667–2673, 1997.

[60] R. Swaminathan, C. P. Hoang, and A. S. Verkman. Photochemical properties of green fluorescent protein GFP-S65T in solution and transfected CHO cells: Analysis of cytoplasmic viscosity by gfp translational and rotational diffusion. *Biophys. J.*, 72:1900–1907, 1997.

[61] K. Luby-Phelps. Cytoarchitecture and physical properties of cytoplasm: Volume, viscosity, diffusion, intracellular surface area. *Int. Rev. Cytol.*, 192:189–221, 2000.

[62] K. Luby-Phelps, D. L. Taylor, and F. Lanni. Probing the structure of cytoplasm. *J. Cell. Biol.*, 102:2015–2022, 1986.

[63] K. Luby-Phelps, P. E. Castle, D. L. Taylor, and F. Lanni. Hindered diffusion of inert tracer particles in the cytoplasm of mouse 3T3 cells. *Proc. Natl. Acad. Sci. USA.*, 84:4910–4913, 1987.

[64] M. Arrio-Dupont, S. Cribier, G. Foucault, P. F. Devaux, and A. D'Albis. Diffusion of fluorescently labeled macromolecules in cultured muscle cells. *Biophys. J.*, 70:2327–2332, 1996.

[65] O. Seksek, J. Biwersi, and A. S. Verkman. Translational diffusion of macromolecule-sized solutes in cytoplasm and nucleus. *J. Cell Biol.*, 138:131 – 142, 1997.

[66] K. M. Berland, P. T. So, and E. Gratton. Two-photon fluorescence correlation spectroscopy: Method and application to the intracellular environment. *Biophys. J.*, 68:694–701, 1995.

[67] M. Wachsmuth, W. Waldeck, and J. Langowski. Anomalous diffusion of fluorescent probes inside living cell nuclei investigated by spatially-resolved fluorescence correlation spectroscopy. *J. Mol. Biol.*, 298:677–690, 2000.

[68] D. S. Banks and C. Fradin. Anomalous diffusion of proteins due to molecular crowding. *Biophys. J.*, 89:2960–2971, 2005.

[69] I.Golding and E.Cox. Physical nature of bacterial cytoplasm. *Phys. Rev. Lett.*, 96:098102, 2006.

[70] M. V. Smoluchowski. Versuch einer mathematischen Theorie der Koagulationskinetik kolloider Lösungen. *Z. Phys. Chem.*, 92:129–168, 1917.

[71] R. Kopelman. Rate processes on fractals: Theory, simulations, and experiments. *J. Stat. Phys.*, 42:185–200, 1986.

[72] R. Kopelman. Fractal reaction kinetics. *Science*, 241:1620 – 1626, 1988.

[73] M. C. Bujan-Nunez, A. Miguel-Fernandez, and M. A. Lopez-Quintela. Diffusion-influenced controlled reaction in an inhomogeneous medium: Small concentration of reagents. *J. Chem. Phys.*, 112:8495, 2000.

[74] M. J. Saxton. Chemically limited reactions on a percolation cluster. *J. Chem. Phys.*, 116:203–208, 2002.

[75] L. Michaelis and M. L. Menten. Die Kinetik der Invertinwirkung. *Biochem. Z.*, 49:333–369, 1913.

[76] H. Berry. Monte Carlo simulations of enzyme reactions in two dimensions: Fractal kinetics and spatial segregation. *Biophys J*, 83:1891–1901, 2002.

[77] J. D. Murray. *Mathematical Biology.* Springer-Verlag, 1993.

[78] Sekimura T., Madzvamuse A., Wathen A. J., and Maini P. K. A model for colour pattern formation in the butterfly wing of Papilio dardanus. *Proc. Biol. Sci.*, 267:851–859, 2000.

[79] H. Meinhardt. *The algorithmic beauty of sea shells.* Springer-Verlag, Berlin, 1995.

[80] M. Howard, A. D. Rutenberg, and S. de Vet. Dynamic compartmentalization of bacteria: Accurate division in E. coli. *Phys. Rev. Lett.*, 87:278102, 2001.

[81] H. Meinhardt and P. A. J. de Boer. Pattern formation in Escherichia coli: A model for the pole-to-pole oscillations of Min proteins and the localization of the division site. *Proc. Natl. Acad. Sci. USA.*, 98:14202–14207, 2001.

[82] A. M. Turing. The chemical basis of morphogenesis. *Philos. Trans. R. Soc. London, Ser. B*, 237:37, 1952.

[83] M. Weiss. Stabilizing Turing patterns with subdiffusion in systems with low particle numbers. *Phys. Rev. E*, 68:036213, 2003.

[84] Ellis R. J. Macromolecular crowding: Obvious but underappreciated. *Trends Biochem. Sci.*, 26:597–604, 2001.

[85] G. Rivas, F. Ferrone, and J. Herzfeld. Life in a crowded world. *EMBO Reports*, 5:23–27, 2004.

[86] Minton A. P. Implications of macromolecular crowding for protein assembly. *Curr. Opin. Struct. Biol.*, 10:34–39, 2000.

[87] Minton A. P. Influence of macromolecular crowding upon the stability and state of association of proteins: Predictions and observations. *J. Pharm. Sci.*, 94:1668–1675, 2005.

[88] Minton A. P. Models for excluded volume interaction between an unfolded protein and rigid macromolecular cosolutes: Macromolecular crowding and protein stability revisited. *Biophys. J.*, 88:971–985, 2005.

[89] Minton A. P. Non-ideality and the thermodynamics of sickle-cell hemoglobin gelation. *J. Mol. Biol.*, 110:89–103, 1977.

[90] Han J. and Herzfeld J. Interpretation of the osmotic behavior of sickle cell hemoglobin solutions: Different interactions among monomers and polymers. *Biopolymers*, 45:299–306, 1998.

[91] S. B. Zimmerman and S. O. Trach. Effects of macromolecular crowding on the association of E.coli ribosomal particles. *Nucleic Acids Research*, 16:6309–6326, 1988.

[92] van den Berg B., Ellis R. J., and Dobson C. M. Effects of macromolecular crowding on protein folding and aggregation. *EMBO J.*, 18:6927–6933, 1999.

[93] van den Berg B., Dobson C. M., and Ellis R. J. Macromolecular crowding perturbs protein refolding kinetics: Implications for folding inside the cell. *EMBO J.*, 19:3870–3875, 2000.

[94] Herzfeld J. Entropically driven order in crowded solutions: From liquid crystals to cell biology. *Acc. Chem. Res.*, 29:31–37, 1996.

[95] Zimmerman S. B. and Murphy L. D. Macromolecular crowding and the mandatory condensation of DNA in bacteria. *FEBS Lett.*, 390:245–248, 1996.

[96] Somalinga B. and Roy R. Volume exclusion effect as a driving force for reverse proteolysis. *J. Biol. Chem.*, 277:43253–43261, 2002.

[97] J. M. Mitchison and M. M. Swann. The mechanical properties of the cell surface. I. The cell elastimeter. *J. Exp. Biol.*, 31:443–460, 1954.

[98] R. P. Band and A. C. Burton. Mechanical properties of the red cell membrane. I. Membrane stiffness and intracellular pressure. *Biophys. J.*, 4:115, 1964.

[99] R. M. Hochmuth. Micropipette aspiration of living cells. *J. Biomech.*, 33:15–22, 2000.

[100] M. Radmacher, M. Fritz, C. M. Kacher, J. P. Cleveland, and P. K. Hansma. Measuring the viscoelastic properties of human platelets with the atomic force microscope. *Biophys. J.*, 70:556–567, 1996.

[101] E. A-Hassan, W. F. Heinz, M. D. Antonik, N. P. D'Costa, S. Nageswaran, C. A. Schoenenberger, and J. H. Hoh. Relative microelastic mapping of living cells by atomic force microscopy. *Biophys. J.*, 74:1564–1578, 1998.

[102] J. Alcaraz, L. Buscemi, M. Grabulosa, X. Trepat, B. Fabry, R. Farre, and D. Navajas. Microrheology of human lung epithelial cells measured by atomic force microscopy. *Biophys. J.*, 84:2071–2079, 2003.

[103] O. Thoumine and A. Ott. Comparison of the mechanical properties of normal and transformed fibroblasts. *Biorheology*, 34:309–326, 1997.

[104] S. Felder and E. L. Elson. Mechanics of fibroblast locomotion: Quantitative analysis of forces and motions at the leading lamellas of fibroblasts. *J. Cell Biol.*, 111:2513–2526, 1990.

[105] R. B. Nicklas. Measurements of the force produced by the mitotic spindle in anaphase. *J. Cell Biol.*, 97:542–548, 1983.

[106] A. R. Bausch, Ziemann F., Boulbitch A. A., Jacobson K., and Sackmann E. Local measurements of viscoelastic parameters of adherent cell surfaces by magnetic bead microrheometry. *Biophys. J.*, 75:2038–2049, 1998.

[107] A. R. Bausch, W. Moeller, and E. Sackmann. Measurement of local viscoelasticity and forces in living cells by magnetic tweezers. *Biophys. J.*, 76:573–579, 1999.

[108] B. Fabry, G. N. Maksym, J. P. Butler, M. Glogauer, D. Navajas, N. A. Taback, E. J. Millet, and J. J. Fredberg. Time scale and other invariants of integrative mechanical behavior in living cells. *Phys. Rev. E*, 68:041914, 2003.

[109] E. Lim and S. Zhou. Mechanical models for living cells. A review. *J. Biomech.*, 39:195–216, 2006.

[110] A. Yeung and E. Evans. Cortical shell liquid core model for passive flow of liquid-like spherical cells into micropipets. *Biophys. J.*, 56:139–149, 1989.

[111] D. P. Theret, M. J. Levesque, M. Sato, R. M. Nerem, and L. T. Wheeler. The application of a homogeneous half-space model in the analysis of endothelial cell micropipette measurements. *J. Biomech. Engineering*, 110:190–199, 1988.

[112] B. Fabry, G. N. Maksym, J. P. Butler, M. Glogauer, D. Navajas, and J. J. Fredberg. Scaling the microrheology of living cells. *Phys. Rev. Lett.*, 87:148102, 2001.

[113] Y. Tseng, J. S. H. Lee, T. P. Kole, I. Jiang, and D. Wirtz. Micro-organization and visco-elasticity of the interphase nucleus revealed by particle nanotracking. *J. Cell Sci.*, 117:2159–2167, 2004.

[114] M. L. Gardel, F. Nakamura, J. H. Hartwig, J. C. Crocker, T. P. Stossel, and D. A. Weitz. Prestressed F-actin networks cross-linked by hinged filamins replicate mechanical properties of cells. *Proc. Natl. Acad. Sci. USA.*, 103:1762–1767, 2006.

[115] F. Gittes, B. Schnurr, P. D. Olmsted, F. C. MacKintosh, and C. F. Schmidt. Microscopic viscoelasticity: Shear moduli of soft materials determined from thermal fluctuations. *Phys. Rev. Lett.*, 79:3286–3289, 1997.

[116] F. Amblard, A. C. Maggs, B. Yurke, A. N. Pargellis, and S. Leibler. Subdiffusion and anomalous local viscoelasticity in actin networks. *Phys. Rev. Let.*, 77:4470–4473, 1996.

[117] F. Guilak, J. R. Tedrow, and R. Burgkart. Viscoelastic properties of the cell nucleus. *Biochem. Biophys. Res. Commun.*, 269:781–786, 2000.

[118] Vaziri A. and Mofrad M. R. K. Mechanics and deformation of the nucleus in micropipette aspiration experiment. *J. Biomech.*, 40:2053–2062, 2006.

[119] J. Nickerson. Experimental observations of a nuclear matrix. *J. Cell. Sci.*, 114:463–474, 2001.

[120] J. Guck, S. Schinkinger, B. Lincoln, F. Wottawah, S. Ebert, M. Romeyke, D. Lenz, H. M. Erickson, R. Ananthakrishnan, D. Mitchell, J. Kaes, S. Ulvick, and C. Bilby. Optical deformability as an inherent cell marker for testing malignant transformation and metastatic competence. *Biophys. J.*, 88:3689–3698, 2005.

[121] K. A. Ward, W. I. Li, S. Zimmer, and T. Davis. Viscoelastic properties of transformed cells: Role in tumor cell progression and metastasis formation. *Biorheology*, 28:301–313, 1991.

[122] M. Lekka, P. Laidler, D. Gil, J. Lekki, Z. Stachura, and A. Z. Hrynkiewicz. Elasticity of normal and cancerous human bladder cells studied by scanning force microscopy. *Eur. Biophys. J.*, 28:312–316, 1999.

[123] E. M. Darling, S. Zauscher, J. A. Block, and F. Guilak. A thin-layer model for viscoelastic, stress-relaxation testing of cells using atomic force microscopy: Do cell properties reflect metastatic potential? *Biophys. J.*, 92:1784–1791, 2007.

[124] J. B. Wyckoff, J. G. Jones, J. S. Condeelis, and J. E. Segall. A critical step in metastasis: In vivo analysis of intravasation at the primary tumor. *Cancer Res.*, 60:2504–2511, 2000.

[125] D. Magde, E. Elson, and W. W. Webb. Thermodynamic fluctations in a reacting system. Measurement by fluorescence correlation spectroscopy. *Phys. Rev. Let.*, 29:705–708, 1972.

[126] E. L. Elson and D. Magde. Fluorescence correlation spectroscopy. I. Conceptual basis and theory. *Biopolymers*, 14:1–27, 1974.

[127] D. Magde, E. L. Elson, and W. W. Webb. Fluorescence correlation spectroscopy. II. An experimental realization. *Biopolymers*, 13:29–61, 1974.

[128] D. Magde, W. W. Webb, and E. L. Elson. Fluorescence correlation spectroscopy. III. Uniform translation and laminar flow. *Biopolymers*, 17:361–376, 1978.

[129] M. Ehrenberg and R. Rigler. Rotational Brownian-motion and fluorescence intensity fluctuations. *Chem. Phys.*, 4:390–401, 1974.

[130] J. Schlessinger, D. Axelrod, D. E. Koppel, W. W. Webb, and E. L. Elson. Lateral transport of a lipid probe and labeled proteins on a cell membrane. *Science*, 195:307–309, 1977.

[131] P. Schwille and E. Haustein. Fluorescence correlation spectroscopyy: A tutorial for the Biophysics Textbook Online BTOL. *Biophysics Textbook Online BTOL*, 2002.

[132] M. Borsch, P. Turina, C. Eggeling, J. R. Fries, C. A. Seidel, A. Labahn, and P. Graber. Conformational changes of the H^+-ATPase from Escherichia coli upon nucleotide binding detected by single molecule fluorescence. *FEBS Lett.*, 437:251, 1998.

[133] M. Kinjo and R. Rigler. Ultrasensitive hybridization analysis using fluorescence correlation spectroscopy. *Nucleic Acids Research*, 23:1795–1799, 1995.

[134] R. Rigler, A. Pramanik, P. Jonasson, G. Kratz, O. T. Jansson, P.-A. Nygren, S. Stahl, K. Ekberg, B.-L. Johansson, and S. Uhlen. Specific binding of proinsulin C-peptide to human cell membranes. *Proc. Natl. Acad. Sci. USA*, 96:13318 – 13323, 1999.

[135] H. Quian and E. L. Elson. Analysis of confocal laser-microscope optics for 3-D fluorescence correlation spectroscopy. *Appl. Opt.*, 30:1185–1195, 1991.

[136] R. Rigler, U. Mets, J. Widengren, and P. Kask. Fluorescence correlation spectroscopy with high count rate and low-background - Analysis of translational diffusion. *Eur. Biophys. J.*, 22:169, 1993.

[137] J. Widengren, R. Rigler, and Ü. Mets. Triplet-state monitoring by fluorescence correlation spectroscopy. *J. Fluorescence*, 4:255–258, 1994.

[138] I. Y. Wong, M. L. Gardel, D. R. Reichman, E. R. Weeks, M. T. Valentine, A. R. Bausch, and D. A. Weitz. Anomalous diffusion probes microstructure dynamics of entangled F-actin networks. *Phys. Rev. Lett.*, 92:178101, 2004.

[139] P. M. Chaikin and T. C. Lubensky. *Principles of Condensed Matter Physics.* Cambridge University Press, Cambridge, 1994.

[140] W. Hess and R. Klein. Generalized hydrodynamics of systems of Brownian particles. *Adv. Phys.*, 32:173–283, 1983.

[141] A. V. Oppenheim and A. S. Wilsky. *Signals and Systems.* Prentice-Hall, London, 1983.

[142] M. M. Bradford. A rapid and sensitive method for the quantitation of microgram quantities of protein utilizing the principle of protein-dye binding. *Anal. Biochem.*, 72:248–254, 1976.

[143] P. Labhart. Ku-dependent nonhomologous DNA end joining in Xenopus egg extracts. *Mol. Cell. Biol.*, 19:2585–2593, 1999.

[144] P. Schwille, J. Korlach, and W. W. Webb. Anomalous subdiffusion of proteins and lipids in membranes observed by fluorescence correlation spectroscopy. *Biophys. J.*, 76:A391, 1999.

[145] M. H. Jacobs. The measurement of cell permeability with particular reference to the erythrocyte. In *Modern Trends in Physiology and Biochemistry* (ed. E. S. G. Barrón), p. 149. New York: Academic Press., 1952.

[146] F. Lang, G. L. Busch, and H. Voelkl. The diversity of volume regulatory mechanisms. *Cell. Physiol. Biochem.*, 8:1–45, 1998.

[147] D. R. Tivey, N. L. Simmons, and J. F. Aiton. Role of passive potassium fluxes in cell volume regulation in cultured HeLa cells. *J. Membr. Biol.*, 87:93–105, 1985.

[148] M. Weiss, H. Hashimoto, and T. Nilsson. Anomalous protein diffusion in living cells as seen by fluorescence correlation spectroscopy. *Biophys. J.*, 84:4043, 2003.

[149] S. Hess and W. Webb. Focal volume optics and experimental artifacts in confocal fluorescence correlation spectroscopy. *Biophys. J.*, 83:2300–2317, 2002.

[150] F. Hoefling, T. Franosch, and E. Frey. Localization transition of the 3D Lorentz model and continuum percolation. *Phys. Rev. Lett.*, 96:165901, 2006.

[151] M. L. Gardel, M. T. Valentine, J. C. Crocker, A. R. Bausch, and D. A. Weitz. Microrheology of entangled F-actin solutions. *Phys. Rev. Lett.*, 91:158302, 2003.

[152] J. D. Ferry. *Viscoelastic Properties of Polymers.* Wiley, New York, 1980.

[153] M. Doi and S. F. Edwards. *The Theory of Polymer Dynamics.* Oxford University Press, Oxford, UK, 1986.

[154] M. V. Berry and Z. V. Lewis. On the Weierstrass-Mandelbrot fractal function. *Proc. R. Soc. (Lond.) A*, 370:459–484, 1980.

[155] M. Elsner, H. Hashimoto, J. Simpson, D. Cassel, T. Nilsson, and M. Weiss. Spatiotemporal dynamics of the COPI vesicle machinery. *EMBO R.*, 4:1000–1004, 2003.

[156] C. Wilson, H. Zhan, L. Swint-Kruse, and K. Matthews. The lactose repressor system: Paradigms for regulation, allosteric behavior and protein folding. *Cell. Mol. Life Sci*, 64:3–16, 2007.

[157] R. Duden. ER-to-Golgi transport: COPI and COPII function. *Mol. Membr. Biol.*, 20:197–207, 2003.

[158] U. Alon, L. Camarena, M. Surette, B. Aguera y Arcas, Y. Liu, S. Leibler, and J. Stock. Response regulator output in bacterial chemotaxis. *EMBO J.*, 17:4238–4248, 1998.

[159] O. G. Mouritsen. *Life-As a Matter of Fat. The Emerging Science of Lipidomics.* Springer Verlag, Berlin., 2005.

[160] D. Chandler. Insight review: Interfaces and the driving force of hydrophobic assembly. *Nature*, 437:640–647, 2005.

[161] M. O. Jensen and O. G. Mouritsen. Lipids do influence protein function - The hydrophobic matching hypothesis revisited. *Biochim. Biophys. Acta*, 1666:205–226, 2004.

[162] J. Korlach, P. Schwille, W. W. Webb, and G. W. Feigenson. Characterization of lipid bilayer phases by confocal microscopy and fluorescence correlation spectroscopy. *Proc. Natl. Acad. Sci. USA.*, 96:8461–8466, 1999.

[163] R. H. Austin, S. S. Chan, and T. M. Jovin. Rotational diffusion of cell surface components by time-resolved phosphorescence anisotropy. *Proc. Natl. Acad. Sci. USA.*, 76:5650–5654, 1979.

[164] S. J. Singer and G. L. Nicholson. The fluid mosaic model of the structure of cell membranes. *Science*, 175:720–731, 1972.

[165] K. Simons and E. Ikonen. Functional rafts in cell membranes. *Nature*, 119:569–572, 1997.

[166] D. M. Engelman. Membranes are more mosaic than fluid. *Nature*, 438:578–580, 2005.

[167] M. J. Saxton and K. Jacobson. Single-particle tracking: Applications to membrane dynamics. *Annu. Rev. Biophys. Biomol. Struct.*, 26:373–399, 1997.

[168] A. Kusumi, C. Nakada, K. Ritchie, K. Murase, K. Suzuki, H. Murakoshi, R. S. Kasai, J. Kondo, and T. Fujiwara. Paradigm shift of the plasma membrane concept from the two-dimensional continuum fluid to the partitioned fluid: High-speed single-molecule tracking of membrane molecules. *Annu. Rev. Biophys. Biomol. Struct.*, 34:351–378, 2005.

[169] M. Edidin. The state of lipid rafts: From model membranes to cells. *Annu. Rev. Biophys. Biomol. Struct.*, 32:257–283, 2003.

[170] S. Heinzer, S. Woerz, C. Kalla, K. Rohr, and M. Weiss. A model for the self-organization of exit sites in the endoplasmic reticulum. *J. Cell Sci.*, 121:55, 2008.

[171] S. Nir and W. D. Stein. Two modes of diffusion in liquids. *J. Chem. Phys.*, 55:1598, 1971.

[172] W. L. C. Vaz, F. Goodsaid-Zalduondo, and K. Jacobson. Lateral diffusion of lipids and proteins in bilayer membranes. *FEBS Lett.*, 174:199–207, 1984.

[173] H. J. Galla, W. Hartmann, U. Theilen, and E. Sackmann. On two-dimensional passive random walk in lipid bilayers and fluid pathways in biomembranes. *J. Membr. Biol.*, 48:215–236, 1979.

[174] W. L. C. Vaz, R. M. Clegg, and D. Hallmann. Translational diffusion of lipids in liquid crystalline phase phosphatidylcholine multibilayers: A comparison of experiment with theory. *Biochemistry*, 24:781–786, 1985.

[175] C. C. Lee and N. O. Petersen. The lateral diffusion of selectively aggregated peptides in giant unilamellar vesicles. *Biophys. J.*, 84:1756–1764, 2003.

[176] B. D. Hughes, B. A. Pailthorpe, and L. R. White. The translational and rotational drag on a cylinder moving in a membrane. *J. Fluid Mech.*, 110:349–372, 1981.

[177] C.-H. Chang, H. Takeuchi, T. Ito, K. Machida, and S. Ohnishi. Lateral mobility of erythrocyte membrane proteins studied by the fluorescence photobleaching recovery technique. *J. Biochem. (Tokyo)*, 90:997 – 1004, 1981.

[178] R. Peters and R. J. Cherry. Lateral and rotational diffusion of bacteriorhodopsin in lipid bilayers: Experimental test of the Saffman-Delbrück equations. *Proc. Natl. Acad. Sci. USA*, 79:4317–4321, 1982.

[179] W. L. C. Vaz, M. Criado, V. M. C. Madeira, G. Schoellmann, and T. M. Jovin. Size dependence of the translational diffusion of large integral membrane proteins in liquid-crystalline phase lipid bilayers. A study using fluorescence recovery after photobleaching. *Biochemistry*, 21:5608–5612, 1982.

[180] Y. Gambin, R. Lopez-Esparza, M. Reffay, E. Sierecki, N. Gov, M. Genest, R. Hodges, and W. Urbach. Lateral mobility of proteins in liquid membranes revisited. *Proc. Natl. Acad. Sci. USA.*, 103:2098–2102, 2006.

[181] K. V. Damodaran and K. M. A Merz. Comparison of DMPC-based and DLPE-based lipid bilayers. *Biophys. J.*, 66:1076–1087, 1994.

[182] U. Essman and M. L. Berkowitz. Dynamical properties of phospholipid bilayers from computer simulation. *Biophys. J.*, 76:2081–2089, 1999.

[183] M. Pasenkiewicz-Gierula, Y. Takaoka M., H. Miyagawa, K. Kitamura, and A. Kusumi. Charge pairing of headgroups in phosphatidylcholine membranes: A molecular dynamics simulation study. *Biophys. J.*, 76:1228–1240, 1999.

[184] D. P. Tieleman, L. R. Forrest, M. S. P. Sansom, and H. J. C. Berendsen. Lipid properties and orientation of aromatic residues in OmpF, influenza M2, and alamethicin systems: Molecular dynamics simulations. *Biochemistry*, 37:17554–17561, 1998.

[185] S. Bandyopadhyay, M. Tarek, and M. L. Klein. Molecular dynamics study of a lipid-DNA complex. *J. Phys. Chem. B*, 103:10075–10080, 1999.

[186] R. Goetz, G. Gompper, and R. Lipowsky. Mobility and elasticity of self-assembled membranes. *Phys. Rev. Lett.*, 82:221–224, 1999.

[187] J. C. Shelley, M. Y. Shelley, R. C. Reeder, S. Bandyopadhyay, and M. L. Klein. A coarse grain model for phospholipid simulations. *J. Phys. Chem. B*, 105:4464–4470, 2001.

[188] P. J. Hoogerbrugge and J. M. V. A. Koelman. Simulating microscopic hydrodynamic phenomena with dissipative particle dynamics. *Europhys. Lett.*, 19:155–160, 1992.

[189] P. Espanol and P. Warren. Statistical mechanics of dissipative particle dynamics. *Europhys. Lett.*, 30:191–196, 1995.

[190] E. G. Flekkoy and P. V. Coveney. From molecular dynamics to dissipative particle dynamics. *Phys. Rev. Let.*, 83:1775–1778, 1999.

[191] S. Yamamoto, Y. Maruyama, and S. Hyodo. Dissipative particle dynamics study of spontaneous vesicle formation. *J. Chem. Phys.*, 116:5842, 2002.

[192] J. C. Shillcock and R. Lipowsky. Equilibrium structure and lateral stress distribution of amphiphilic bilayers from dissipative particle dynamics simulations. *J. Chem. Phys.*, 117:5048–5061, 2002.

[193] M. Laradji and P. B. Kumar. Dynamics of domain growth in self-assembled fluid vesicles. *Phys. Rev. Lett.*, 93:198105, 2004.

[194] M. Venturoli, B. Smit, and M. M. Sperotto. Simulation studies of protein-induced bilayer deformations, and lipid-induced protein tilting, on a mesoscopic model for lipid bilayers with embedded proteins. *Biophys. J.*, 88:1778–1798, 2005.

[195] P. Nikunen, M. Karttunen, and I. Vattulainen. How would you integrate the equations of motion in dissipative particle dynamics simulations? *Comp. Phys. Comm.*, 153:407–421, 2003.

[196] R. D. Groot and P. B. Warren. Dissipative particle dynamics: Bridging the gap between atomistic and mesoscopic simulation. *J. Chem. Phys.*, 107:4423–4435, 1997.

[197] A. F. Jakobsen, O. G. Mouritsen, and M. Weiss. Close-up view on the modifications of fluid membranes due to phospholipase A2. *J. Phys. Condens. Matter.*, 17:4015–4024, 2005.

[198] M. Laradji and P. B. Kumar. Domain growth, budding, and fission in phase-separating self-assembled fluid bilayer. *J. Chem. Phys.*, 123:224902, 2005.

[199] G. Besold, I. Vattulainen, M. Karttunen, and J. M. Polson. Towards better integrators for dissipative particle dynamics simulations. *Phys. Rev. E*, 62:R7611, 2000.

[200] A. F. Jakobsen, O. G. Mouritsen, and G. Besold. Artifacts in dynamical simulations of coarse-grained model lipid bilayers. *J. Chem. Phys.*, 122:204901, 2005.

[201] S. E. Feller, Y. Zhang, R. W. Pastor, and B. R. Brooks. Constant pressure molecular dynamics simulation: The langevin piston method. *J. Chem. Phys.*, 103:4613–4621, 1995.

[202] O. Farago. 'water-free' computer model for fluid bilayer membranes. *J. Chem. Phys.*, 119:596, 2003.

[203] G. Brannigan and F. L. H. Brown. Solvent-free simulations of fluid membrane bilayers. *J. Chem. Phys.*, 120:1059–1071, 2004.

[204] I. R. Cooke, K. Kremer, and M. Deserno. Tunable generic model for fluid bilayer membranes. *Phys. Rev. E.*, 72:011506, 2005.

[205] A. Naji, A. J. Levine, and P. A. Pincus. Corrections to the Saffman-Delbrück mobility for membrane bound proteins. *Biophys. J.*, 93:L49–L51, 2007.

[206] E. Reister-Gottfried, S. M. Leitenberger, and U. Seifert. Hybrid simulations of lateral diffusion in fluctuating membranes. *Phys. Rev. E*, 75:011908, 2007.

[207] S. M. Leitenberger, E. Reister-Gottfried, and U. Seifert. Hybrid simulations of lateral diffusion in fluctuating membranes. *Langmuir*, 24:1254–1261, 2007.

[208] K. Svoboda and S.M. Block. Biological applications of optical forces. *Ann. Rev. Biophys. Biomol. Struct.*, 23:247–285, 1994.

[209] P. Cicuta, S. L. Keller, and S. L. Veatch. Diffusion of liquid domains in lipid bilayer membranes. *J. Phys. Chem. B*, 111:3328–3331, 2007.

Publications

1. G. Guigas and M. Weiss
   Size-dependent diffusion of membrane inclusions.
   Biophysical Journal 91:2393-2398 (2006)

2. G. Guigas, C. Kalla and M. Weiss
   Probing the nanoscale viscoelasticity of intracellular fluids in living cells.
   Biophysical Journal 93:316-323 (2007)

3. G. Guigas, C. Kalla and M. Weiss
   The degree of macromolecular crowding in the cytoplasm and nucleoplasm of mammalian cells is conserved.
   FEBS Letters 581:5094-5098 (2007)

4. G. Guigas and M. Weiss
   Sampling the cell with anomalous diffusion - The discovery of slowness.
   Biophysical Journal 94:90-94 (2008)

5. G. Guigas and M. Weiss
   Influence of hydrophobic mismatching on membrane protein diffusion.
   In press, Biophysical Journal (2008)

6. U. Schmidt*, G. Guigas* and M. Weiss
   Cluster formation of transmembrane proteins due to hydrophobic mismatching.
   Submitted
   * equal contribution

Danksagung

Diese Arbeit wurde in der Zeit von April 2005 bis Mai 2008 in der Abteilung Zelluläre Biophysik am Deutschen Krebsforschungszentrum in Heidelberg angefertigt.

Prof. Dr. Michael Hausmann vom Kirchhoff-Institut für Physik danke ich für sein freundliches Interesse an meiner Arbeit und die Übernahme der Betreuung und Begutachtung von seiten der Fakultät für Physik und Astronomie der Universität Heidelberg.

Mein besonderer Dank gilt Dr. Matthias Weiss, dem Leiter unserer Arbeitsgruppe, der mich in jeder nur denkbaren Weise unterstützt und durch unsere Zusammenarbeit nachhaltig geprägt hat – als Wissenschaftler ebenso wie als Mensch.

Stephan Heinzer danke ich für die vielen Diskussionen, in denen er mir biologische Zusammenhänge aufzeigte, des Weiteren für wertvolle Anmerkungen zu meiner Arbeit und zahlreiche gemeinsame Unternehmungen jenseits der Wissenschaft.

Claudia Kalla danke ich für ihre tatkräftige Unterstützung in allen mit dem Nasslabor, der Zellkultur und der Zellmikroskopie in Zusammenhang stehenden Tätigkeiten.

Ulrich Schmidt dank ich für die gute Zusammenarbeit bei unseren gemeinsamen Projekten, für viele klärende Erörterungen wissenschaftlicher Fragen, insbesondere aber für seine hilfreichen technischen Ratschläge während der Erstellung der vorliegenden Arbeit.

Diana Morozova, Jedrzey Szymanski und Jens Kühnle danke ich für das Korrekturlesen meiner Arbeit und zahlreiche nützliche Anmerkungen.

Nina Malchus, Marcel Hellmann und allen bereits Genannten sei an dieser Stelle noch einmal herzlich gedankt für den freundschaftlichen Umgang innerhalb der Arbeitsgruppe und die angenehme Zusammenarbeit während der letzten Jahre.